

**Experimental Investigation of the Flow Dynamics in
Models of Patient-Specific Aneurysms**
Hugo Blons

A Thesis in The Department of Mechanical, Industrial & Aerospace
Engineering

Presented in Partial Fulfillment
of
the Requirements
For the Degree
of
Master of Applied Science (Mechanical Engineering)
at
Concordia University Montréal, Québec, Canada

August 2023

© Hugo Blons, 2023

CONCORDIA UNIVERSITY SCHOOL OF GRADUATE STUDIES

This is to certify that the thesis prepared

By: Hugo Blons

Entitled: Experimental Investigation of the Flow Dynamics in Models of Patient-Specific Aneurysms

and submitted in partial fulfillment of the requirements for the degree of

Master of Applied Science (Mechanical Engineering)

complies with the regulations of the University and meets the accepted standards with respect to originality and quality.

Signed by the final examining committee:

_____ Chair
Dr. Hoi Dick Ng

_____ Examiner
Dr. Hang Xu

_____ Thesis supervisor
Dr. Lyes Kadem

Approved by _____
Dr. Sivakumar Narayanswamy, MSc Program Director

September 2023 _____
Dr. Mourad Debbabi, Dean Gina Cody School of Engineering & Computer
Science

Abstract

Experimental Investigation of the Flow Dynamics in Models of Patient-Specific Aneurysms
Hugo Blons

This work investigates the complex flow dynamics in patient-specific compliant models of Abdominal Aortic Aneurysms (AAA) using time-resolved Particle Image Velocimetry (PIV). Scans of multiple planes were performed on three different models: a healthy aorta, a 4-cm saccular AAA, and a 7-cm fusiform AAA. We discuss the differences in flow patterns in patient-specific models compared to idealized models from previous work. We note that the curvature of the aorta upstream from the aneurysm, specific placement of the iliac arteries, and the overall symmetry of the aneurysm have important effects on flow structures, such as increasing transient effects, vortex formation, and wall impingement. Viscous energy dissipation rate (VEDr) was also evaluated as it has been previously identified as a potentially good metric to assess the severity of some vascular diseases.

Finally, a modal analysis was performed on the velocity fields using Proper Orthogonal Decomposition (POD). The main modes obtained were inspected to identify the dominant structures, and the distribution of energy between the modes (Shannon entropy), and to create a reduced-order model of the flow. The results show that Shannon entropy was significantly different between the three models, suggesting that it can be a promising clinical parameter to evaluate the severity of AAAs.

Acknowledgments

I would like to start by presenting my thanks to all who helped me during my master's thesis. First to Dr. Lyes Kadem who welcomed me two years ago to the Laboratory of Cardiovascular Fluid Dynamic and trusted me with this project. Who was always understanding and ready to give time to help and guide me.

To Dr. Wael Saleh and Dr. Ahmed Darwish who taught me how to work in the lab, without whom I would have certainly learned much less in the field of experimental physics. Thank you for always being ready to take your time to help me.

To Osman Aycan who was a great collaborator in the many hours we worked together. Thanks for all the hard work and immeasurable help.

To all the members of the Laboratory of cardiovascular fluid dynamics thanks for the lightness and happiness you brought with you it helped me a lot when the workday was long.

To my friends and family thanks for everything

Contents

<u>List of figures</u>	vii
<u>Tables</u>	ix
<u>Acronyms</u>	x
1 Introduction	p1
1.1 <u>Cardiovascular System</u>	p1
1.1.1 Function	p1
1.1.2 Blood	p1
1.1.3 Heart	p1
1.1.4 Arteries	p3
1.1.5 Abdominal aorta	p5
1.2 <u>Abdominal Aortic Aneurysm</u>	p6
1.2.1 Description	p6
1.2.2 Risk factors	p7
1.2.3 Complication	p8
1.2.4 Diagnostic	p8
1.2.5 Treatment	p9
1.3 <u>Thesis outline</u>	p11
2 Literature review	p13
2.1 <u>Hemodynamics of the aorta</u>	p13
2.1.1 Flow in a healthy aorta	p13
2.1.2 Flow in abdominal aortic aneurysm	p14
2.2 <u>AAA flow characterization</u>	p15
2.2.1 <i>In vivo</i> studies	p15
2.2.2 <i>In vitro</i> studies	p17
2.2.3 <i>In silico</i> studies	p21
2.3 <u>Viscous energy loss</u>	p23
2.4 <u>Modal analysis</u>	p24
2.5 <u>Thesis objectives</u>	p25
3 Methodology	p27
3.1 <u>Experimental setup</u>	p27
3.1.1 Flow circulatory system	p27
3.1.2 Pressure and flow validation	p31
3.1.3 AAA phantom	p34
3.1.4 Blood-mimicking fluid	p37
3.2 <u>Particle Image Velocimetry</u>	p40
3.2.1 Basic principles	p40
3.2.2 Experimental setup	p42
3.3 <u>Processing</u>	p46
3.3.1 Image pre-processing	p46
3.3.2 Computation of the velocities	p47
3.3.3 Velocity gradients calculation	p48
3.3.4 Viscous energy dissipation	p49
3.3.5 Proper orthogonal decomposition	p50
4 Results	p54
4.1 <u>Instantaneous velocity field</u>	p54
4.1.1 Healthy aorta	p54
4.1.1.1 Velocity fields at rest, Healthy aorta.	p55
4.1.1.2 Impact of increased heart rate, case of the healthy aorta	p57

4.1.2 Saccular aneurysm model	p58
4.1.2.1 Velocity fields at rest, Saccular aneurysm model	p59
4.1.2.2 Impact of increased heart rate on the flow in the saccular aneurysm	p62
4.1.3 Fusiform aneurysm model	p64
4.1.3.1 Velocity fields at rest	p65
4.1.3.2 Impact of increased heart rate in the fusiform aneurysm	p67
4.2 <u>Viscous energy loss</u>	p68
4.3 <u>Proper Orthogonal Decomposition</u>	p73
4.3.1 Mode description	p77
4.3.2 Healthy model	p76
4.3.3 Saccular aneurysm model	p79
4.3.4 Fusiform Model	p82
4.3.5 Data reduction with POD	p85
4.3.6 Viscous energy of the reconstructed mode	p87
4.3.7 Shannon entropy	p88
5 Discussion and conclusion	p90
5.1 <u>Patient-specific models</u>	p90
5.2 <u>Hemodynamic study of AAA in patient-specific models</u>	p90

List of figures

[Figure 1](#): Blood circulation in the heart. ([Iaizzo et al. 2010](#)), with modified labels.

[Figure 2](#): Diagram of the three layers of the arterial wall: intima, media, and adventitia ([Holzapfet et al. 2000](#)).

[Figure 3](#): Compliance of a healthy aorta during a cycle systole/diastole ([Briet et al. 2012](#)).

[Figure 4](#): Schematic of the aortic anatomy ([Sakalihasan et al. 2018](#)).

[Figure 5](#): A) a saccular AAA, B) a fusiform AAA, from patient-specific data used in this thesis.

[Figure 6](#): Schematic of OSR, A) open aorta with clamp blocking blood flow, B) the aortic walls sutured around the craft, C) schematic of EVAR, on an aneurysm containing an intraluminal thrombus ([Sakalihasan et al. 2018](#)).

[Figure 7](#): Schematic of EVAS technic A) Nellix system in place in the AAA B) deployment of the endobags sealing the aneurysm ([Brownrigg et al. 2015](#)).

[Figure 8](#): Schematic of distinct types of endoleaks and their classification ([Kassem et al. 2017](#)).

[Figure 9](#): Experimental setup, A) schematic, B) in laboratory setup.

[Figure 10](#): Motor control electrical waveforms, A) heart rate 60 bpm $T_l = 1$ s, B) heart rate 80 bpm $T = 0.75$ s, A) heart rate 100 bpm $T_l = 0.6$ s.

[Figure 11](#): Experimental pressure waveforms.

[Figure 12](#): Volumetric Flow rate and instantaneous Reynolds number, A) $r_1 = 60$ bpm, 1 Hz, B) $r_2 = 80$ bpm, 1.3 Hz, C) $r_3 = 100$ bpm, 1.7 Hz.

[Figure 13](#): The 3D-CAD models of the abdominal aorta. Posterior view (left) and left lateral view (right), A) Healthy aorta, B) Fusiform aneurysm, C) Saccular aneurysm.

[Figure 14](#): Fusiform AAA model, A) 3D printed Lumen, B) Silicone phantom.

[Figure 15](#): Main concept of velocity vector computation in 2 components planar PIV.

[Figure 16](#): Normalized light scattering intensity by the selected tracker particle ([Di Labbio 2019](#)).

[Figure 17](#): Proper orthogonal decomposition snapshot method from ([Darwish et al. 2021](#)).

[Figure 18](#): Planes investigated for the healthy aorta.

[Figure 19](#): Velocity field snapshots, healthy aorta plane A, the dimensionless times ($t^* = t/T_I$) instants are indicated in red on the flow waveform graph.

[Figure 20](#): Velocity field snapshots, healthy aorta plane B.

[Figure 21](#): Velocity field at $t^* = 0.275$ comparison between the three different heart rates.

[Figure 22](#): Planes investigated for the saccular aneurysm model.

[Figure 23](#): Velocity snapshot, saccular aneurysm plane A, the dimension-less times ($t^* = t/T_I$) are indicated in red on the flow waveform graph.

[Figure 24](#): Velocity snapshot, saccular aneurysm plane G.

[Figure 25](#): Velocity fields at $t^* = 0.175$ and $t^* = 0.45$, on plane A comparison for different heart rates.

[Figure 26](#): Planes of investigation for the fusiform AAA model.

[Figure 27](#): Velocity field snapshots, fusiform aneurism plane A, the dimensionless times ($t^* = t/T_I$) are indicated in red on the flow waveform graph underneath.

[Figure 28](#): Velocity field snapshots, fusiform aneurism plane G.

[Figure 29](#): Velocity fields at $t^* = 0.45$, on plane G comparison for the different heart rates.

[Figure 30](#): Energy dissipation rate by unit depth in the healthy aorta.

[Figure 31](#): Energy dissipation rate by unit of depth in the saccular AAA model.

[Figure 32](#): Energy dissipation rate by unit depth total fusiform AAA model.

[Figure 33](#): Total energy loss during a heartbeat, the y-axis represents the total energy loss, and the x-axis represents all cases studied by plane clustered in groups of increasing heart rates.

[Figure 34](#): Energy contained in the 65 first modes, for $r = r_I$, A) healthy model, B) saccular model, C) fusiform model.

[Figure 35](#): First two POD modes for planes A and B in the healthy aortic model, A) POD modes, B) time coefficients of the modes in plane A, C) time coefficients of the modes in plane B.

[Figure 36](#): First four POD modes for plane A in the saccular AAA model, A) POD modes, B) time coefficients of the modes.

[Figure 37](#): First four POD modes for plane G in the saccular AAA model, A) POD modes, B) time coefficients of the modes.

[Figure 38](#): First four POD modes for plane A in the fusiform AAA model, A) POD modes, B) time coefficients of the modes.

[Figure 39](#): First four POD modes for plane G in the fusiform AAA model, A) POD modes, B) time coefficients of the modes.

[Figure 40](#): Velocity field snapshots, reduced order model capturing 98% of the overall kinetic energy, fusiform model on plane A $T = T_I$.

[Figure 41](#): Difference in kinetic energy loss between the PIV data and the reduced order model.

[Figure 42](#): Shannon entropy y-axis, x-axis represents all cases studied clustered by plane in groups of heart rate levels.

Tables

[Table 1](#): Experimental setup parameters.

[Table 2](#): Number of modes needed to capture a given kinetic energy fraction.

Acronyms

Abdominal Aortic Aneurysm (AAA)

Aliphatic Polyester Material (PLA)

Direct Numerical Simulations (DNS)

Doppler Color Ultrasound (DCU)

Doppler ultrasound velocimetry (DUV)

Echocardiographic PIV (echo-PIV)

Endovascular Aneurysm Repair (EVAR)

Endovascular Aneurysm Sealing (EVAS)

Kinetic Energy (KE)

Large Eddy Simulation (LES)

Laser Doppler Velocimetry (LDV)

Open Surgical Repair (OSR)

Oscillatory Shear Index (OSI)

Particle Image Velocimetry (PIV)

Phase Contrast Magnetic Resonance Imaging (PC-MRI)

Refractive Index (RI)

Reynolds Averaged Navier Stokes (RANS)

Thermoplastic Polyurethane (TPU)

Viscous Energy Dissipation rate (VEDr)

Wall Shear Stress (WSS)

1 Introduction

1.1 Cardiovascular System

1.1.1 Function

The cardiovascular system is a means of transport for nutrients, metabolic end products, and cells in the body. The British physiologist William Harvey published one of the first descriptions of the cardiovascular system, as a closed-loop system, and established the importance of blood circulation ([Harvey et al. 1928](#)). The latter is the flow of a carrier fluid in vessels, called arteries and veins, due to a pressure constraint created by the contraction of the heart's muscles.

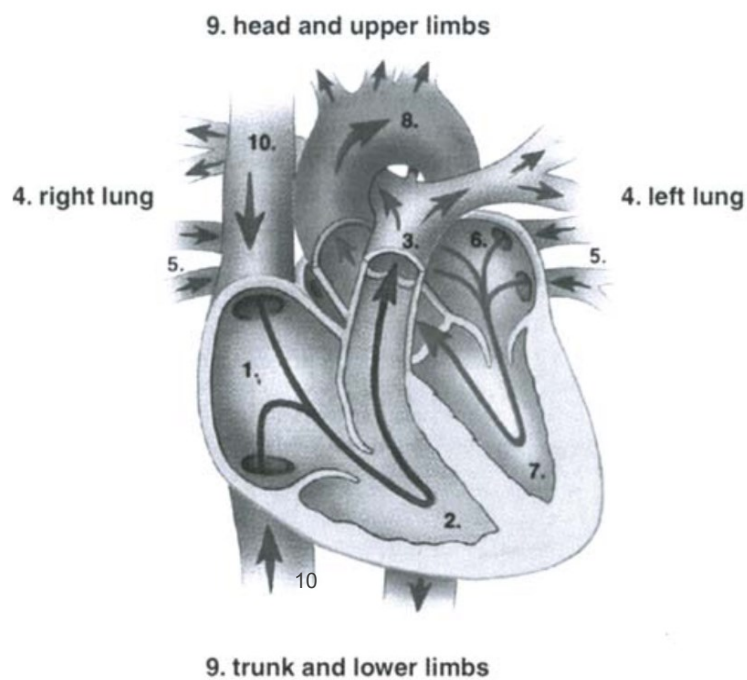
1.1.2 Blood

We can note that the word *blood* refers to the mentioned carrier fluid and all its content. The fluid itself is called plasma, if isolated it has similar components to interstitial fluid with which it forms the major parts of extracellular fluid in the body ([Betts et al. 2013](#)). The blood also contains platelets that allow coagulation by clumping, red blood cells (also called erythrocytes) that carry oxygen in the blood, and diverse types of white blood cells, which take part in the immune response, in case of infection.

1.1.3 Heart

The flow of blood is created thanks to the action of the heart. It is divided into two sides, left and right, each of which contains two cavities called atrium and ventricle. Blood enters the heart through an atrium then it passes in a ventricle and is expelled from the heart ([Iaizzo et al. 2010](#)). [Figure 1](#) presents the anatomy of the heart and the blood circulation through it. Valves separate atriums from ventricles and are also found at the entry and exit points of the

heart. The left side of the heart receives oxygenated blood from the lungs and redistributes it in the body; the right side does the inverse with blood poor in dioxygen. Blood vessels are classified into two main categories regarding the direction of their blood flow to the heart. Therefore, we call veins blood vessels where the blood goes back to the heart, and arteries if the blood flows from the heart towards any other part of the body. The blood flow is created by the contraction of the myocardium, the heart's muscle. It periodically tenses and unknots expelling blood in the arteries. The two phases of this cycle are called systole, when the myocardium contracts itself, and diastole when it unknots.



- | | | |
|-------------------|-------------------|--------------------------|
| 1 right atrium | 5 pulmonary veins | 9 other organs |
| 2 right ventricle | 6 left atrium | 10 superior and inferior |
| 3 pulmonary trunk | 7 left ventricle | |

Figure 1: Blood circulation in the heart. ([Iaizzo et al. 2010](#)), with modified labels.

1.1.4 Arteries

As written above, arteries are vessels where the blood flow is directed from the heart to other organs. Arteries must accommodate the periodic pressure of the heart. To accomplish this, arterial walls are composed of different layers. For a given patient, the exact composition will depend on the place in the vessel network of the artery's section ([Gopalakrishnan et al. 2014](#)). Those layers are, from the outer to the inner, the external layer (also called adventitia), the media layer (also called muscular), and the intima ([Gopalakrishnan et al. 2014](#)), as presented in [Figure 2](#). The presence of smooth muscle cells in the media and of connective tissues in both media and adventitia gives arteries elasticity. This allows a reduction of blood pressure in the artery during the systole when the artery is dilated, and an increase of blood pressure in the artery during the diastole, when the artery contracts, this mechanism is presented in [Figure 3](#). This flattens the pressure waveform in the arteries. As a result, the pressure waveform in arteries varies with the specificity of a patient's heart but also with the specificity of the patient's arteries. Connective tissues are one of the main components of the mechanical properties of the arterial walls. The elastin and collagen are the main connective tissue that we can find in the arterial wall. They are regrouped in the adventitia and media layer of the walls. Elastin is found in the media. It is one of the prevailing tissues of the arterial wall. Elastin fibers form a network in extracellular matrices, they form up to 30% of the dry weight of the aorta. Those networks give elasticity to the arterial walls and attenuate shocks due to the pulsatile blood flow. They are also responsible for the recoil of the arteries during diastole. Collagen is present in media and adventitia; it is the primary component of the adventitia and is far less extensible than elastin and brings support to the arteries. The arterial walls also contain smooth muscle cells, which are actively helping to give it its mechanical properties.

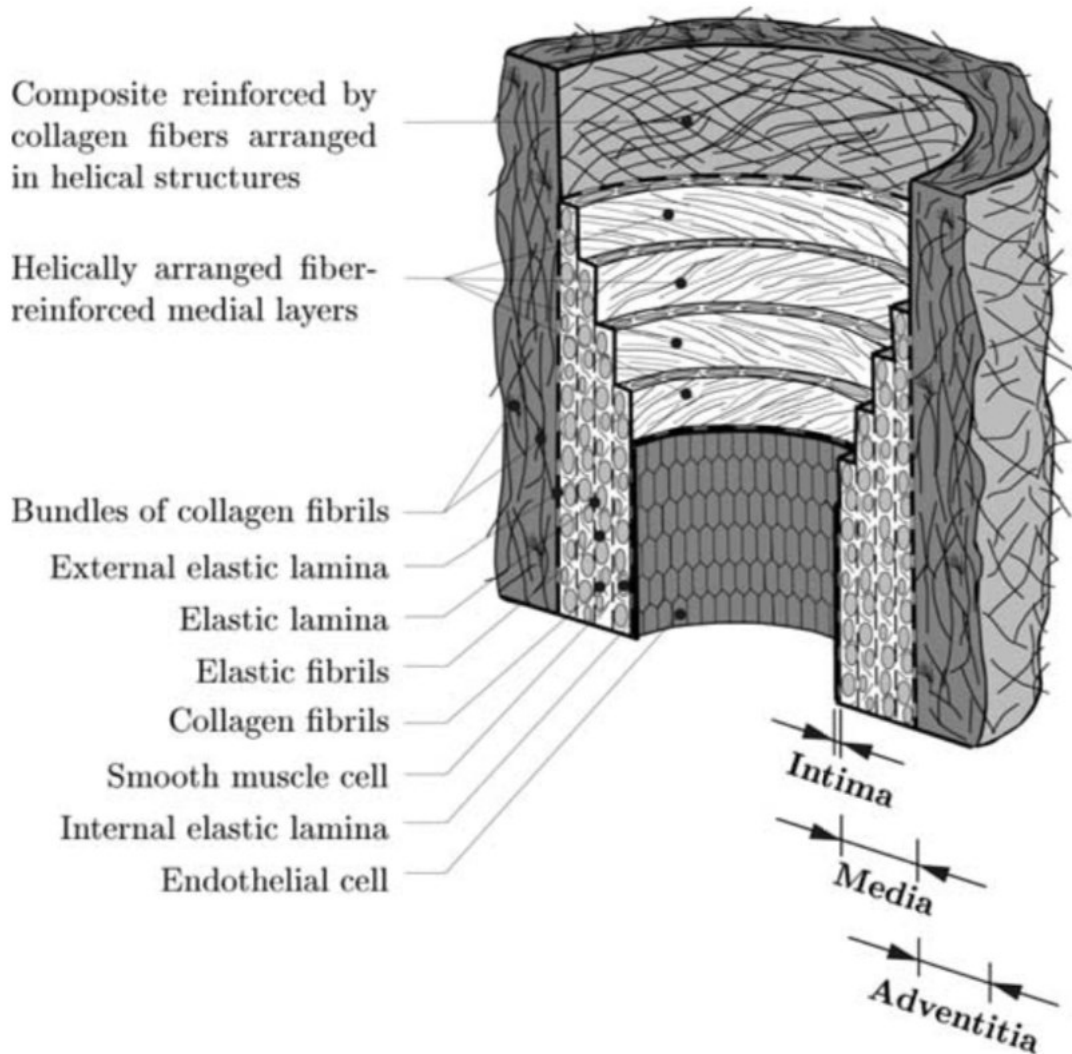


Figure 2: Diagram of the three layers of the arterial wall: intima, media, and adventitia ([Holzapfet et al. 2000](#)).

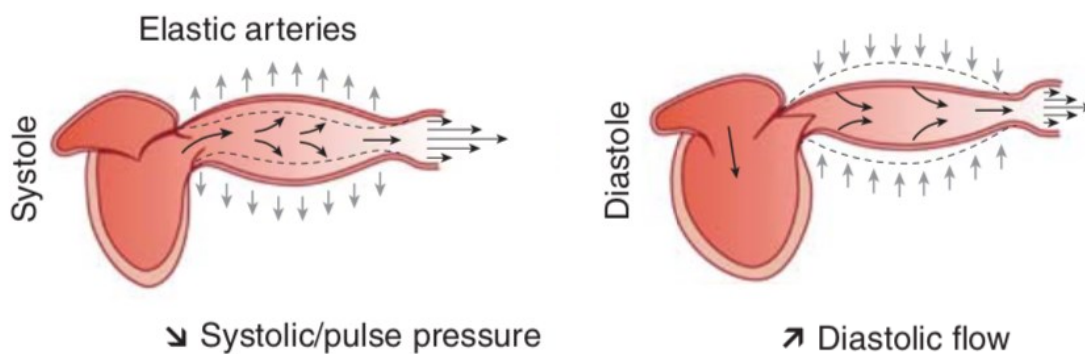
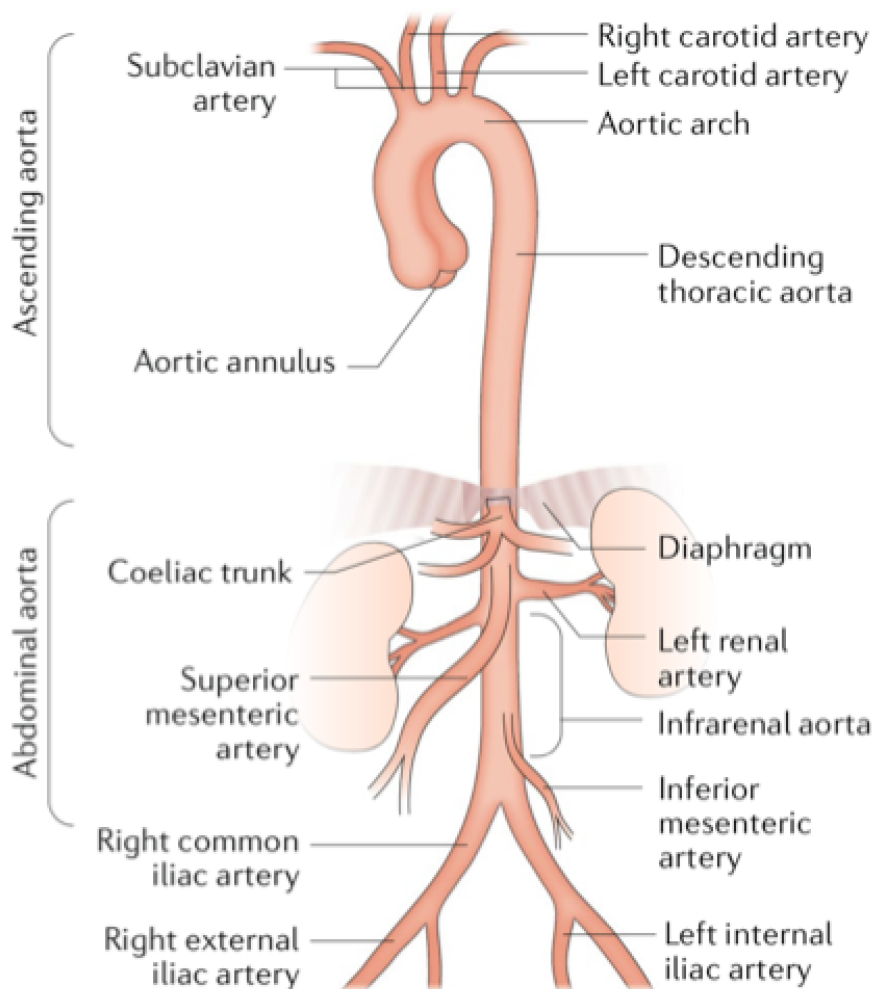


Figure 3: Compliance of a healthy aorta during a cycle systole/diastole ([Briet et al. 2012](#)).

1.1.5 Abdominal Aorta

The abdominal aorta is a section of the aorta, the largest artery in the abdominal region. It ends by dividing itself into the two iliac arteries at the level of the 4th lumbar vertebrae. It is connected to diverse smaller arteries that irrigate the abdominal region. The two renal arteries, commonly located at the level of the intervertebral disc between the 1st and 2nd lumbar vertebrae, can be used to identify two parts of the abdominal aorta, the suprarenal abdominal and infrarenal respectively above and under the branch between the abdominal aorta and the renal arteries. [Figure 4](#) presents the abdominal aorta in relation to the rest of the aorta.



[Figure 4](#): Schematic of the aortic anatomy ([Sakalihasan et al. 2018](#)).

1. 2 Abdominal Aortic Aneurysm or AAA

1.2.1 Description

An aneurysm is a disease characterized by a deformation of a blood vessel. In arteries, it can weaken the arterial wall and change the blood flow. Some observations reveal a disturbance in the architecture of arterial walls and a loss of connective tissue ([Alexander et al. 2004](#)). This can lead to a loss of resistance to deformation allowing therefore the aneurysm to grow with time. Clinically, a growth of 150% or more in the diameter of an artery is considered an aneurysm. Abdominal Aortic Aneurysms (AAA) are more often found in the infrarenal region which could be understood as the result of an inhomogeneity of deformation of the abdominal aorta, resembling the results obtained with simplified models by ([Duclaux et al. 2010](#)). However, this is not always the case, and some AAAs are found above the branch between the abdominal aorta and the renal arteries.

Aneurysms are classified into two groups, originally called true aneurysms when the deformation is a dilatation of the artery and false when the deformation is a sac attached to the artery ([Laennec et al. 1837](#)), ([Withers et al. 2013](#)). These are now called fusiform (true) and saccular (false). [Figure 5](#) presents the two forms of AAA.

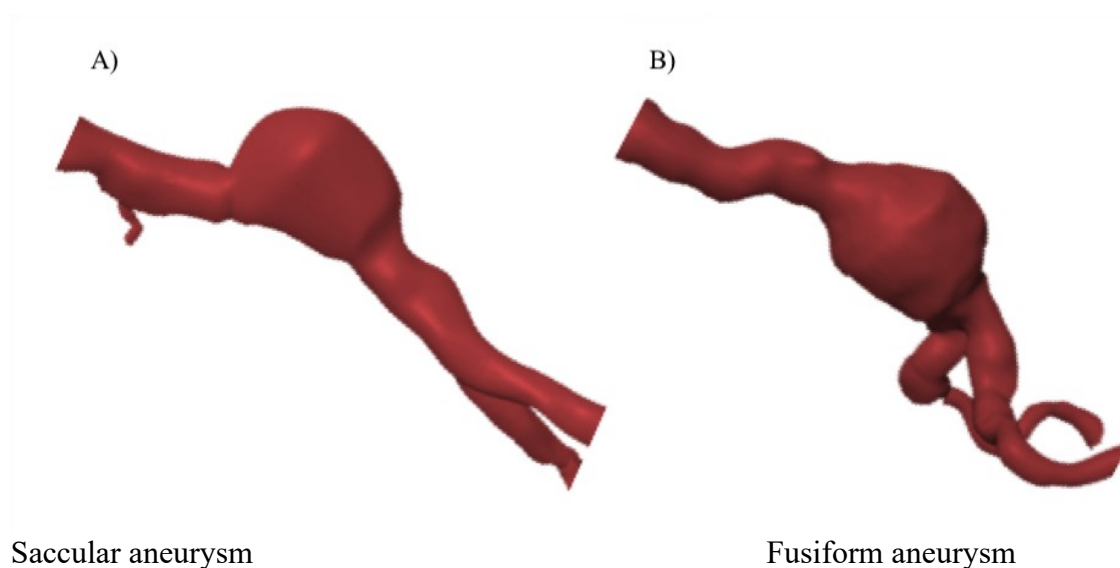


Figure 5: A) a saccular AAA, B) a fusiform AAA, from patient-specific data used in this thesis.

1.2.2 Risk factors

The causes of the formation of an AAA are still not fully understood, but several risk factors have been identified. Some identified risk factors are age, male sex, family history, smoking, hypertension, overweight, and other vascular diseases ([Kent et al. 2010](#)). It is reasonable to believe that the motor of the formation and growth of aneurysms is an abnormal interaction between the blood flow and the arterial wall.

Age as a risk factor can be linked to a progressive loss of elasticity of the aorta (also true for other arteries) linked to the aging of tissues. Stiffer arterial walls change the pressure waveform; the mechanism of storing blood during systole and releasing it during diastole is not possible anymore. This creates a higher blood pressure in the artery, which is suspected to be a key factor in aneurysm development. More complex consequences, like a difference in wave reflection with stiffer arteries, could have an impact on the blood flow. Risks linked to smoking are quantifiable by the following parameters: the number of smoking years, the number of cigarettes smoked per day and for people who quit smoking, the duration since quitting, etc., all impact the odds of developing an AAA.

Vascular diseases like arteriosclerosis, which is the accumulation of lipids and other material partially cloaking an artery, are also noticeable suspects. The partial cloaking will change the blood flow and therefore change the forces exerted on the arterial wall. Furthermore, the presence of lipids against the wall can influence it and change its structure. However, no direct link between the two pathologies has been found ([Alexander et al. 2004](#)).

1.2.3 Complication

In the worst-case scenario, weakened walls of an aneurysm can break, leading to internal bleeding. According to the Multicentre Aneurysm Screening Study group ([Scott et al. 2002](#)), half of the victims of an aneurysm's rupture die before reaching a hospital, and the mortality rate when taking into account the risk of mortality of the emergency operation is between 65% and 85%.

1.2.4 Diagnostic

It is therefore extremely important to diagnose AAA as early as possible. So, patients can undergo preventive surgery if the risk of rupture is high.

The simplest detection method is physical examination, or the detection of irregularities indicating the presence of an aneurysm through palpation of the abdominal region. However, this method has limitations; For instance, the precision of this method is dependent on the patient's anatomy and the diameter of the aneurysm, and overall is not precise enough to be an efficient diagnostic tool, as concluded by ([Lynch et al. 2004](#)).

A more efficient method is ultrasound imaging. This imaging method uses high-frequency sound waves; the amplitude of the signal and the time needed to go through the body is used as an indicator of the properties of traversed matter, bone tissue, or blood. It gives an image of the internal organs. The transmitter can be placed on the skin or in the body, in the case of abdominal observation no intrusion is needed; the transmitter is on the skin. The ultrasound waves bring energy to the tissues; therefore, a high level of ultrasound can bring some unwanted effects. Those effects can be the heating of tissues or the formation of gas bubbles in the body. Ultrasound imaging must be used carefully but it remains a useful tool for in vivo imaging with minimal drawbacks ([Health Canada webpage](#)). To detect AAA, the Multicentre Aneurysm Screening Study attests that the use of ultrasound imaging is efficient in 99% of

cases and expresses that their results tend to advocate for the benefit of screening with ultrasound imaging population at risk of developing AAA ([Scott et al. 2002](#)).

Other imaging methods can be used to detect and study AAAs; among them, we can find magnetic resonance imaging (MRI), where powerful magnetic fields are used. This leads the tissue to emit a specific electromagnetic signal that can be detected and traced back to the tissue that emitted it. Computed Tomography scans (CT) that use X-rays to visualize organs can also be used. CT scans and MRI are both more precise than ultrasound imaging, they allow for a better visualization of the aneurysm's shape. However, they are more challenging to implement. CT scans also have the disadvantage of exposing the patient to radiation, which in the case of repetitive use to monitor an aneurysm growth over time should be avoided. Radiations can damage tissues and cell metabolism. Different types of radiation have different biological impacts. The sievert unit (Sv) gives the equivalent doses of radiation from a biological impact point of view. An adult abdominal CT corresponds to a dose of *10 mSv*. The Canadian dose limit set for nuclear plant workers is *50 mSv* in a year and *100 mSv* in 5 consecutive years, with a reduction to *4 mSv* for pregnant workers ([Canadian Nuclear Safety Commission](#)).

1.2.5 Treatment

When detected, an AAA needs to be closely followed, as a rupture is a life-threatening event. However, operations can also come with risks. An AAA elective repair has a 1% to 5% mortality risk ([Schermerhorn et al. 2009](#)). Even if, it is low in comparison with the risk of death associated with a rupture of the aneurysm, and indeed not every aneurysm should be operated on if the risk of rupture is low. Therefore, as long as the risk of rupture is lower than the risk of the operation it is preferable to monitor the aneurysm. To monitor the aneurysm its maximal diameter and growth over time are studied. It is recommended to operate for any

aneurysm with a diameter > 5.5 cm. However, it is important to note that because the studies included more men than women there is a bias with this maximum diameter criterion, with a lower value expected in women ([Isselbacher et al. 2005](#)).

In the case of an elective surgery, several methods can be used; Open Surgical Repair (OSR), Endovascular Aneurysm Repair (EVAR), both represented in [Figure 6](#), and Endovascular Aneurysm Sealing (EVAS) represented in [Figure 7](#).

For an OSR the surgeon incises the aorta in its length to insert a craft made of a biocompatible synthetic textile. This method requires heavy operations. Therefore, for some patients, the risks of morbidity and mortality are too important. Other methods should then be attempted.

EVAR minimizes intrusion by using an expandable stent-craft, inserted from the femoral artery that is guided, with a catheter, to the aneurysm where it opens stopping the blood from interacting with the aneurysm wall. However, with this technique, the aneurysm still exists, and it is important to continue monitoring it. In some cases, the graft does not completely isolate the aneurysm from the blood circulation and the risk of growth and rupture persists. Patients may need a follow-up operation. This phenomenon called endoleak is divided into classes in function of how the aneurysm is connected to blood circulation ([Kassem et al. 2017](#)), those classes are presented in [Figure 8](#). Another drawback of this method is that EVAR is not suited for all aneurysms. The AAA needs to be at least 15mm long and less than 25mm wide and must be separated from the branch with the renal arteries for this approach to be applicable ([May et al. 2000](#)).

To circumvent the problem of leaking stent-crafts, EVAS is a new method that adds to EVAR the sealing of the remaining aneurysm using the Nellix system (Endologix Irvine, CA USA). This system consists of a stent-craft like those used for EVAR on which are attached balloon-like structures, called endobags, filled with a polymer to seal the aneurysm ([Brownrigg et al. 2015](#)). We can note that similar methods do exist by injection of different materials (e.g., coil,

foam, biological glue) to stop blood flow. This is called embolization, and it can be used in the treatment of some cases of aneurysms or in a second operation after EVAR to stop a leak ([Withers et al. 2013](#)).

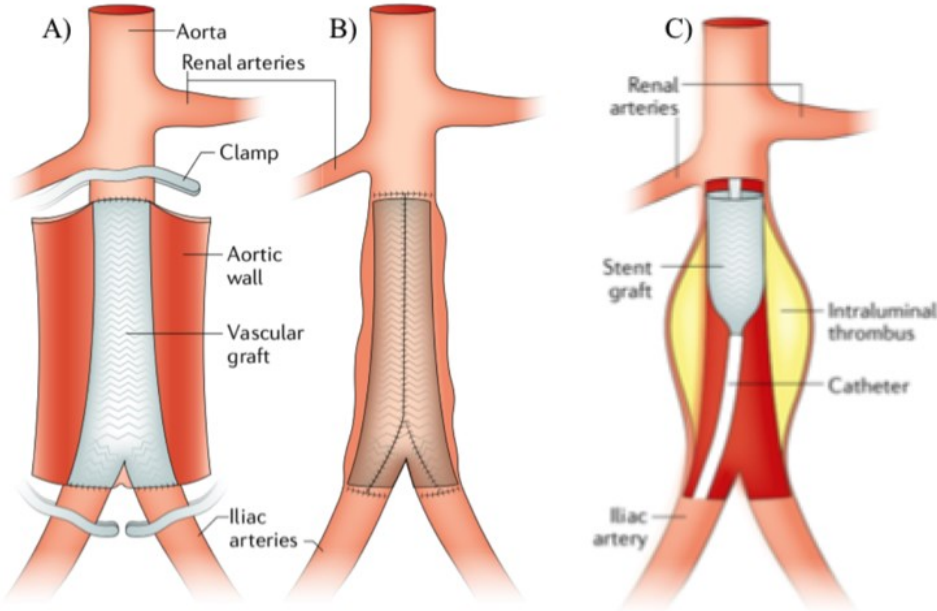


Figure 6: Schematic of OSR, A) open aorta with clamp blocking blood flow, B) the aortic walls sutured around the graft, C) schematic of EVAR, on an aneurysm containing an intraluminal thrombus ([Sakalihasan et al. 2018](#)).

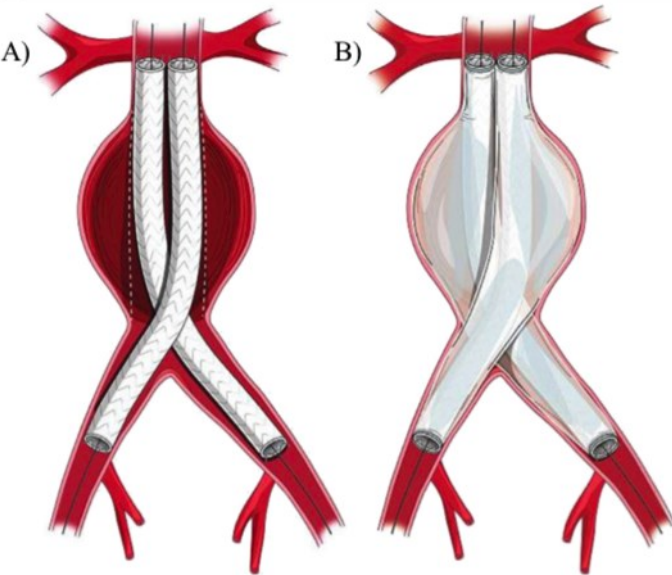


Figure 7: Schematic of EVAS technic A) Nellix system in place in the AAA B) deployment

of the endobags sealing the aneurysm ([Browmrigg et al. 2015](#)).

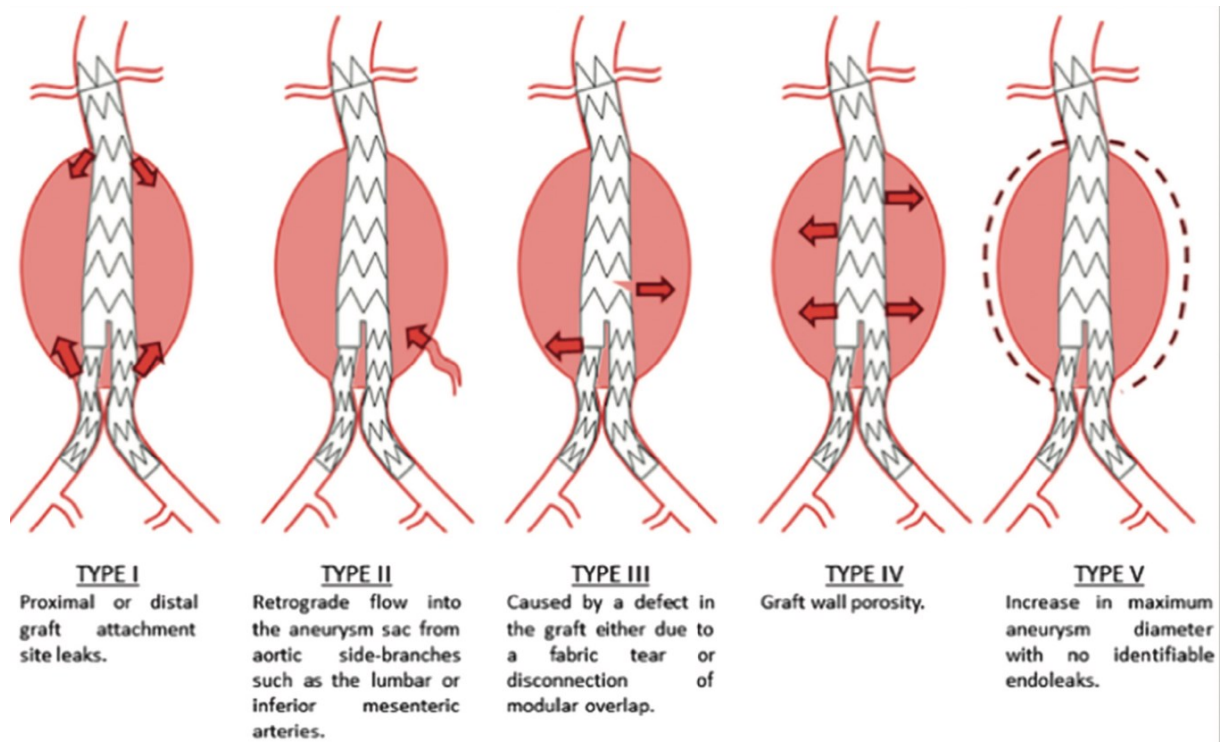


Figure 8: Schematic of distinct types of endoleaks and their classification ([Kassem et al. 2017](#)).

1.3 Thesis outline

This thesis goal is to study the effect of the geometry created by an aneurysm on the blood flow dynamic using an *in vitro* setup and patient-specific models of AAAs. The velocity fields will be resolved using time-resolved Particle Image Velocimetry (PIV),

In the following chapters, we will review previous works related to blood flow dynamics in AAA establishing a proper background to this work ([Ch. 2](#)). Then we will describe our experimental approach including our experimental setup and PIV ([Ch. 3](#)), followed by the results of our study ([Ch. 4](#)). The last chapter will conclude by highlighting important findings from this study and remaining challenges, while also presenting suggestions for follow-up works ([Ch. 5](#))

2 Literature review

2.1 Hemodynamics of the aorta

The nature of the flow in the arteries is known to have a mechanical impact on its walls. Therefore, hemodynamic factors are key components of the evolution of those walls, and a better understanding of flow-induced stresses can provide crucial clues on the dilatation and subsequent rupture of the arterial walls. To understand the pathological flow of AAA it is necessary to have a prior knowledge of the flow through the healthy aorta.

2.1.1 Flow in a healthy aorta

It was expected that the flow in the aorta (with a mean Reynolds close to 600) would be laminar, periodic, and unidirectional, resembling a pulsed flow in a straight tube ([Ku 1997](#)). However, different flows are observed at various locations of the aorta. In the suprarenal aorta, the above-mentioned stable type of flow is observed. However, the flow observed in the infrarenal aorta deviates from a straight tube case. It is only unidirectional during systole. ([Moore et al. 1992](#)) observed four main characteristics of the infrarenal flow: time-varying vortices are created after the renal arteries and propagate through the aorta, the lumbar curvature creates a localized transient separation toward the posterior wall, during late systole a phase of reversed flow is observed along the posterior and lateral walls, finally a horseshoe vortex is created at the terminal aorta due to the aortic bifurcation. The flow through the infrarenal aorta can be considered as a superposition of the unsteady flow through the different geometries that create the aorta, a straight pipe, a curved pipe, a pipe including side branches, and a symmetric bifurcation.

2.1.2 Flow in abdominal aortic aneurysm

An important number of studies on AAA flows have been conducted; the hemodynamics biomarkers studied are the velocity field, vorticity field, wall shear stress, and turbulence intensity. AAA flow is highly patient-specific, it depends on specific geometry and upstream flow for each patient ([Arzani et al. 2012](#)). However, some common features can be identified. First, the AAA flow can be characterized by a transitional flow regime. In the case of a straight tube, transitional and turbulent effects manifest over a Reynolds number of ≈ 2000 (for the peak Re of the pulsatile flow), however transitional flow has been observed at lower Re *in vivo* and *in vitro* studies ([Bluth et al. 1990](#)), ([Khanafer et al. 2009](#)), ([Parashar et al. 2013](#)), ([Poelma et al. 2015](#)) with transitional effects observed even at $Re = 600$. Due to the unstable nature of the flow, small perturbations can cause substantial changes. ([Poelma et al. 2015](#)) compared the integral timescales of transitional flow in different aneurysms, using *in silico* models. They found that for the AAA (large aneurysms compared to the intracranial aneurysm) the instabilities are still present when the systolic phase produces new instabilities, this creates random conditions before each stroke making the flow nonperiodic. ([Vergara et al. 2017](#)) also highlighted the impact of the size of the aneurysm on transitional effects, stating that their simulation showed a high correlation between the dimensions of the AAA and the intensity of the turbulence kinetic energy. The second common flow feature of AAAs is the formation of a large recirculation area in the bulge of the aneurysm. The streamlines tend to go further from the wall when entering the aneurysm, creating a fast-moving jet and a slow-moving recirculation area. It has been observed that a recirculation zone is a preferential area for thrombus formation ([O'Rourke et al. 2012](#)). However, this recirculation zone can mix with the jet flow as found by ([Arzani et al. 2012](#)). The third feature observed in AAAs is

the formation of vortices usually at the distal or proximal end of the aneurysm during systole and propagate downstream. The number, size, and exact path of such vortices are highly patient-dependent ([Arzani et al. 2012](#)). Moreover, it is suspected that a link does exist between such vortices and the intraluminal thrombus ([Chen et al. 2014](#)). However, no causality link has been established. For further precision, the reader can refer to an overview of AAA mechanics ([Kemmerling & Peattie 2018](#)).

2.2 AAA flow characterization

2.2.1 *In vivo* studies

In vivo studies, use clinical data obtained from patients. One of the most common methods for velocity investigation in the abdominal aorta is Doppler ultrasound velocimetry (DUV). DUV works by detecting the Doppler shift in a sound wave scattered from the moving blood component (red and white blood cells). In the case of spectral Doppler ultrasound, automated Fourier analysis is used to convert returning sound waves into a series of individual frequencies. It yields to graphical representation of velocities over time. It results in 1D flow velocities, either a single peak or an average waveform on a single cross-section. The study by ([Fraser et al. 2008](#)) presents one of the first studies of flow data in AAAs. In 31 patients, measurements of the centerline velocity, near an infrarenal aorta aneurysm were obtained. It yielded the identification of 21 characteristic points and the creation of an archetypical centerline velocity waveform. An example of a flow wave, for AAA patients was computed from the velocity waveform, assuming a Womersley profile. The mean flow throughout the cardiac cycle was found to be 0.798 L/min. Even if the archetypical centerline velocity waveform can be used as an inlet condition in either *in vitro* or *in silico* models, it is an

imperfect representation since the actual infrarenal flow is neither axisymmetric nor periodic, two properties needed to assume a Womersley-type profile.

It is also important to note that DUV does not provide information on flow structures and patterns. In addition, it has low resolution and high uncertainty and can be challenging to use since imaging depth and bowel gas can lead to loss of signal.

To our knowledge magnetic resonance imaging is a better choice to study the flow in the aorta, *in vivo*. Two-dimensional, Phase-Contrast, Magnetic Resonance Imaging (PC-MRI) is a method that resolves a single direction in two dimensions. The velocity on a section of the aorta can be measured using PC-MRI, resulting after integration over the entire lumen surface to a more precise estimation of the flow waveform than using the centerline velocity. ([Les et al. 2010 b](#)) used PC-MRI to measure the flow rate in 43 patients, counting only one woman. They used the results to create an average waveform that is scalable according to the body size and can be used as an inlet condition for *in vitro* or *in silico* models.

Closer to our visualization design of the velocity structures in AAAs, 4D flow MRI ([Markl et al. 2012](#)) is a PC-MRI technique allowing the visualization in 3D of the three-velocity components over time, enabling a comprehensive analysis of regional hemodynamics and the identification of new biomarkers such as wall shear forces, pulse wave velocity, pressure gradients, and others. A 4D MRI resolution varies with the studied cardiovascular region. In the aorta, the spatial and temporal resolutions are 2.0 to 2.5 mm and 40 to 50 ms. [Indrakusuma et al. \(2019\)](#) studied the robustness of 4D MRI for applications to hemodynamic studies in AAAs. Thirteen patients, all men, with asymptomatic AAA were scanned twice with an interval of one week. The agreements of the two scans were analyzed through a Bland-Altman plot and an orthogonal regression analysis. Through the acquisition and determination of velocity and wall shear stress, the Bland-Altman plot showed slight

differences, and the orthogonal regression showed moderate agreement. MRI requires no line of site and gives more accurate results than DUV. However, it cannot be used for patients having any metallic implant and thus requires DUV.

Echocardiographic PIV (echo-PIV) is a newly developed method of visualization allowing to obtain 2D velocity fields, with a similar approach as particle image velocimetry (PIV). It is based on ultrasound imaging, and the goal is to follow micro-bubbles in the blood stream. So far, echo-PIV needs a contrast agent to be functional. ([Engelhard et al. 2018](#)) presented the first results of echo-PIV performed in the abdominal aorta of patients and compared the results to 4D MRI. The study was performed on 15 patients including 6 men. The flow patterns of echo-PIV and MRI were found to be qualitatively similar, and a Bland-Altman analysis of peak velocities in 8 patients showed a mean difference of 8.5% between the two methods.

2.2.2 *In vitro* studies

Creating an *in vitro* model can be an interesting approach to studying the hemodynamics in AAA. An engineered model needs to faithfully replicate *in vivo* conditions. The choice of geometry material used for the aneurysm model wall, working fluids, and inlet conditions need to be chosen accordingly. Some other parameters will also be chosen depending on the method of flow visualization; specifically *in vitro* models can be created with transparent materials allowing the use of optical methods.

The first studies of blood flow using *in vitro* models were performed by qualitatively studying flow patterns. ([Moore Jr et al. 1992](#)) used dyes to visualize the flow in a rigid glass model of the aorta, with varying pulsatile inlet conditions (resting, postprandial, and exercise

conditions). The model was based on 55 biplanar angiograms and included the two renal arteries, the inferior and superior mesenteric arteries, the celiac artery, and the iliac arteries. With this observation of the flow in the aorta, it was identified that the flow patterns in the infrarenal aorta were more complex, in the resting condition than those of the suprarenal region. This complexity comes from the formation at the renal arteries' entry points of time-varying vortices that propagate through the infrarenal aorta. A horse-shoe-shaped vortex is created at the aortic bifurcation during the systolic acceleration, and a backward flow is observed during late systole, fluid flows back upstream and swirls in the aorta. Similar patterns were observed with postprandial conditions. However, exercise conditions created a quite different laminar flow.

Doppler Color Ultrasound (DCU) can be used to visualize the flow field giving a first overall perception of the flow. It can be used in tandem with Laser Doppler Velocimetry (LDV) which quantifies the flow velocities. LDV works by measuring the Doppler shift in the scattered light of two lasers at one given point, the light is scattered by micron-sized tracer particles in the fluid. It gives the three directional components of the velocity at this single point with a very high temporal resolution, over 10,000 Hz. Experiments by [\(Asbury et al. 1995\)](#) used DCU and LDV, to study the critical Reynolds number for the onset of turbulence and complete transition to turbulent flow, in seven models of fusiform AAA. Those models were made as symmetric elliptic expansions in a rigid pipe with a straight entrance and exit. The experiment was conducted under steady flow. It was found that, in those models, high shear occurred when the flow was turbulent.

[\(Peattie et al. 2004\)](#) used LDV with a similar setup, however, they studied the effect of the pulsatile flow on 7 rigid simplified AAA models. They identified that vortices appeared in the AAA bulge initially during the deceleration from systole and expanded during the retrograde

flow. Systolic flow was found to be going forward in all models. They identified that the complexity of the flow increased with the increase in bulge diameter. The main issue with LDV is its low spatial resolution as this method only gives results at one point at a time. In the paper of ([Peattie et al. 2004](#)), only 50 points were measured for each model. ([Yip and Yu 2002](#)) conducted a similar study with only 2 rigid AAA models but performed the measurements at 276 individual locations. They performed a stability analysis, showing that instability grows during the acceleration phase and that the transition to turbulence happens shortly after the beginning of the deceleration phase.

To improve the spatial resolution of the measurements, Particle Image Velocimetry (PIV) can be used. This method allows the visualization of 2D velocity components on a full plan, the velocities are computed from the visualization of moving particles scattering the light in a laser sheet. ([Bluestein et al. 1996](#)) presented the hemodynamic impact in the deposition of platelets on the wall of a rigid model of AAA, with cylindrical inlet and outlet, under steady and pulsatile flow. ([Yu et al. 2000](#)) conducted a PIV study on similar AAA models, rigid Pyrex glass tubes at the inlet and outlet with an elliptical bulge and various dimensions. However, the studied flow conditions were both steady and unsteady, with a sinusoidal waveform. The formation and evolution of the vortices in the bulge of the AAA were studied in this setting.

The use of rigid models is widespread in the study of AAAs although it does not reflect the reality of the flexible tissue forming arterial walls. ([Deplano et al. 2007](#)) studied the hemodynamic difference between rigid and flexible AAA models. PIV was used to compute the velocity fields, inside asymmetrical AAA models, one is a rigid glass model and the second is a flexible polyurethane model, both having the same geometry. It was found that the secondary flow patterns, and especially the vortices in the AAA highly depended on the flow

waveform and the wall behavior. In the compliant model, the energy stored during the expansion of the model is restored during the deceleration phase and contributes to the propagation of vortices in the AAA, which eventually leads to vortices impacting the wall of the aneurysm, leading to a repetitive increase in local pressure and thus wall stresses. It is also important to note that this study was conducted using a physiological waveform, leading to a more realistic pulsatile flow than using sinusoidal inlet conditions.

All the above-mentioned models are created as straight tubes, lacking any branches of the aorta, and lacking an aortic bifurcation into iliac arteries. Importantly, the aortic bifurcation can reflect the pulse wave, increasing the pressure. ([Patel et al. 2017](#)) presented a study of the impact of adding the aortic bifurcation to a model, and the effect of stenosis in one of the iliac arteries breaking the symmetry of the outlet. This study was conducted using a physiological waveform in rigid models. It showed that in the presence of an arterial bifurcation, the strength and speed of propagation of the vortices were reduced compared to models using a straight tube outlet. The non-symmetric outlet creates non-symmetric flow patterns in the AAA.

As discussed, time-varying vortices can be created at the renal arteries and propagate in the abdominal aorta. However, several models are created without arterial side branches. ([Kung et al. 2011](#)) created a patient-specific rigid model of AAA including the renal arteries. Including renal arteries makes the model more accurate as discussed, and thus the renal arteries have an important impact on the flow in the infrarenal aorta. However other branches on the aorta do not impact as significantly the flow in the infrarenal region and can therefore be removed to simplify the model. This model was studied using PC MRI.

A lot of AAA models are based on simplified averaged models. Patient-specific models have become easier to create thanks to new manufacturing techniques. ([Zhan et al. 2022](#)) created a

patient-specific rigid model of an AAA, with the iliac arteries as outlets and a straight tube as an inlet and used a physiological waveform. They studied the formation of vortex structures. Their model was paired with a numerical model. The focus of this study was the effect of the intraluminal thrombus, and no comparison of their model with averaged models was made. However, the small vortices group observed in their results have not been observed on simplified averaged models.

Most PIV experiments on AAAs have been conducted using classical 2D PIV. More advanced methods like tomographic PIV and holographic PIV have been developed to visualize flow in 3D with the three-velocity component and have been used in other hemodynamic models. ([Saaïd et al. 2019](#)) used tomographic PIV to visualize the 3D flow in the left ventricle with biological and mechanical valves. However, to the best of our knowledge, experiments on AAAs have not been conducted. Experiments using stereoscopic (stereo-PIV), another PIV technique, have been however conducted on AAAs. ([DePlano et al. 2016](#)) used stereo-PIV in a flexible simplified model of an AAA including an iliac outlet and a straight tube inlet. Tests were done under pulsatile physiological conditions. Using stereo-PIV in different planes and some interpolation techniques it was possible to study the 3D vortex ring evolution formed in the AAA.

2.2.3 *In silico* studies

Numerical models are also interesting alternative methods to investigate the flow behavior in AAAs. As for any other model, the issue is the similarity between the model and physiological AAA and how well the model fits reality. Choices related to the geometry, the fluid properties, and the boundary conditions need to be relevant to the hemodynamic study of

AAA. Additionally, the numerical model needs to resolve the complexity of the flow phenomenon realistically.

The first study of pulsatile flow in an aneurysm was conducted by [\(Wille et Øivind 1981\)](#). This study computed a laminar flow in an axisymmetric model of an aneurysm, using no-slip wall conditions, a velocity profile inlet computed from a straight tube simulation using pressure inlet and outlet. However transitive and turbulent flows are expected in AAA. Turbulence can be modeled in diverse ways. A statistical approach uses averaged equations, Reynolds averaged Navier Stokes (RANS) equations, to model turbulence. It can also be partially resolved by computing eddies up to a given size and approximating the effects of smaller eddies (Large Eddy Simulation LES). Finally, it can be completely resolved at the continuum level using Direct Numerical Simulations (DNS). [\(Bopp et al. 2019\)](#) compared the results of three different RANS models to MRI results on an *in vitro* model. Both models are simplified symmetrical aneurysms with rigid wall straight inlet and outlet tubes. They showed a significant agreement, but some slight differences can also be noted. [\(Vergara et al. 2017\)](#) conducted the first LES simulation of hemodynamics in AAAs. They modeled the flow through three patient-specific AAAs with a straight inlet, the aortic bifurcation in the outlet, rigid walls, and Newtonian rheology. Their study of the transition to turbulence in AAAs showed that transitional effects are significant. [\(Marrero et al. 2014\)](#) conducted a DNS study on patient-specific AAAs with both renal and iliac arteries, with rigid walls. A comparative study of Newtonian and non-Newtonian effects was made and concluded that taking into account the non-Newtonian effects reduced the transitional effects and therefore the computational resources needed. It results in a similar computational cost between the Newtonian and non-Newtonian models even if the non-Newtonian model needs to compute the varying viscosity. The choice of model will be motivated by the phenomenon that is studied, specifically by the accuracy needed and the computational cost of the

model. ([Shadden et al. 2018](#)) studied coherent structures in an averaged geometry model of AAAs and a patient-specific model, showing that the patient-specific hemodynamic is more complex than what the simplified model approximates.

It is interesting to note that patient-specific models are more common for *in silico* experiments, which can be explained by some difficulties in the design of *experiments*

([Scotti et al. 2005](#)) studied the differences between a static wall model and a fluid-structure interaction model to mimic the flexible walls of the aneurysm. They did not find a significant disagreement when comparing wall stresses.

In silico and *in vitro* models have been used in tandem in a lot of studies, specifically, it is a usual practice to validate the value of *in silico* models by comparing them with an *in vitro* counterpart.

2.3 Viscous energy loss

Viscous energy loss is the process of conversion of mechanical kinetic energy into thermal energy through viscous frictions. Viscous friction is the resistive force between relative tangential motions in the fluid. Energy loss is normal in a healthy vascular system. Vascular pathologies have an impact on energy loss. It was seen that a dilatation of the aorta either ascending thoracic or abdominal was accompanied by an increase in energy loss ([Norouzi 2020](#)), ([Barker et al. 2014](#)). It has also been found that aortic stenosis increases energy loss ([Dyverfeldt et al. 2013](#)). The quantification of energy loss could be interesting to evaluate the burden caused on the vascular system by altered hemodynamics. It could also be an accurate marker of disease severity with the possibility of non-invasive measurement.

Multiple studies of energy loss in the heart have been conducted, notably studies on the left ventricle, where the structure of the healthy flow is anticipated to minimize energy dissipation. In this case, the increase in energy loss will be detrimental to the heart which will need to work harder to maintain blood flow ([Di Labbio and Kadem 2018](#)).

In the case of aneurysms, energy dissipation is studied as a potential indicator of the risk of rupture. ([Khe et al. 2015](#)) found in their computational study on intracranial aneurysms that a lower averaged energy dissipation per unit of volume was seen in ruptured aneurysms. In the case of AAAs, ([Norouzi 2020](#)) *in vitro* experiments showed that the geometry has an impact on energy loss and that large diameter aneurysms exhibit higher energy dissipation.

2.4 Modal analysis

Proper Orthogonal Decomposition (POD) is a modal decomposition technique (also named Principal Component Analysis or Karhunen-Loève Transform). In the context of fluid dynamics, it decomposes a physical field such as the velocity field into an optimal set of orthogonal basis functions of special variables (modes). The set is optimal in the sense that the obtained modes maximize their energy content. Each mode obtained is associated with an energy level as well as a temporal coefficient. POD has a wide use in fluid dynamics, it can be used for turbulent analysis to unambiguously define coherent structures ([Cazemier et al. 1997](#)). It can also be used for model order reduction, data filtering, or gappy data reconstruction. ([Mc Gregor et al. 2008](#)) created a data set of different types of flows through the abdominal aorta and the aortic arch, which were mapped onto a standard geometry. Their model was used to improve the accuracy of low spatial resolution phase contrast MRI. The measured flow is mapped onto the model standard geometry and interpolated on a fine mesh, by minimizing a cost function in the modal space. ([Darwish et al. 2021](#)) used POD to identify malfunction of bileaflet mechanical valves, using POD to create a reduced order model from

in vitro flow data in the ascending aorta, for velocity as well as high order flow characteristics such as wall shear stresses. [\(Norouzi 2020\)](#) used averaged *in vitro* models of AAAs to gauge aneurysm severity based on flow data, creating a reduced-order flow model that captured the most important flow features. Their study showed that the increased size of AAA is accompanied by an increased complexity of the flow and a dispersion of the energy in the modes. The complexity of the flow is quantified using Shannon entropy a representation of the dispersion of energy between modes.

2.5 Thesis objectives

As discussed earlier, the interplay between the hemodynamic forces and the aortic wall is important for both the initiation of the aneurysm and its development. Several studies on AAAs have been conducted, *In vivo*, studies can be cumbersome for patients and must deal with challenges in terms of the acquisition, with the more accurate being 4D MRI which still has relatively low spatial and temporal resolutions. *In silico* experiments will most likely have the finest resolution and bring relative ease in the construction of the model geometries compared to *in vitro*. However, the computation of a complex fluid-structure interaction with a pulsed transitional flow can be challenging in terms of the numerical model. There is a need for a validation of the results against *in vivo* or *in vitro* studies. Although extensive *in vitro* experiments have been conducted on AAA models, most *in vitro* experiments use simplified geometries. There is therefore a need to investigate the flow in patient-specific models. Moreover, to the best of our knowledge, no patient-specific studies have been presented with a compliant model taking into account the complexity of the upstream flow and aortic bifurcation. The use of modal analysis POD, to identify coherent structures and create reduced order models, has also been scarce in the study of AAA hemodynamics.

Therefore, this thesis aims at contributing answers to the following questions:

- Can a customized *in vitro* setup reproduce the complex flow of *in vivo* patient-specific AAAs?
- How does the flow in a patient-specific geometry differ from what has been observed in simplified models?
- How does the size of the aneurysm impact the energy loss and flow structures?
- Can modal decomposition using POD be used to identify dominant flow structures and provide robust reduced-order models?

3 Methodology

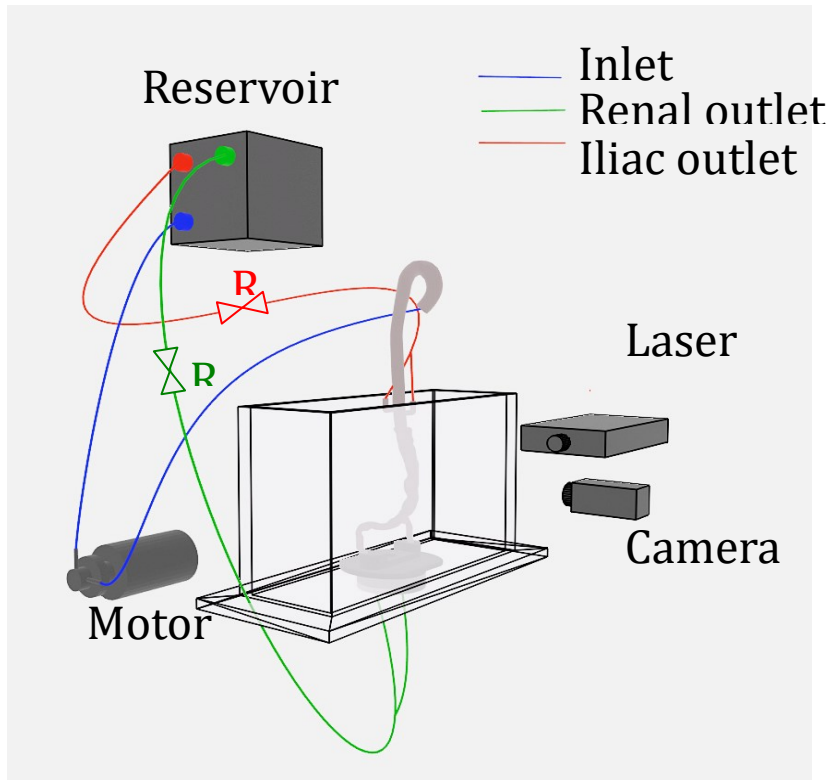
3.1 Experimental setup

3.1.1 Flow circulatory system

The circulatory system has been created to accurately reproduce in vivo flow conditions.

[Figure 9](#) shows the custom-made experimental facility developed in the context of this thesis.

A)



B)

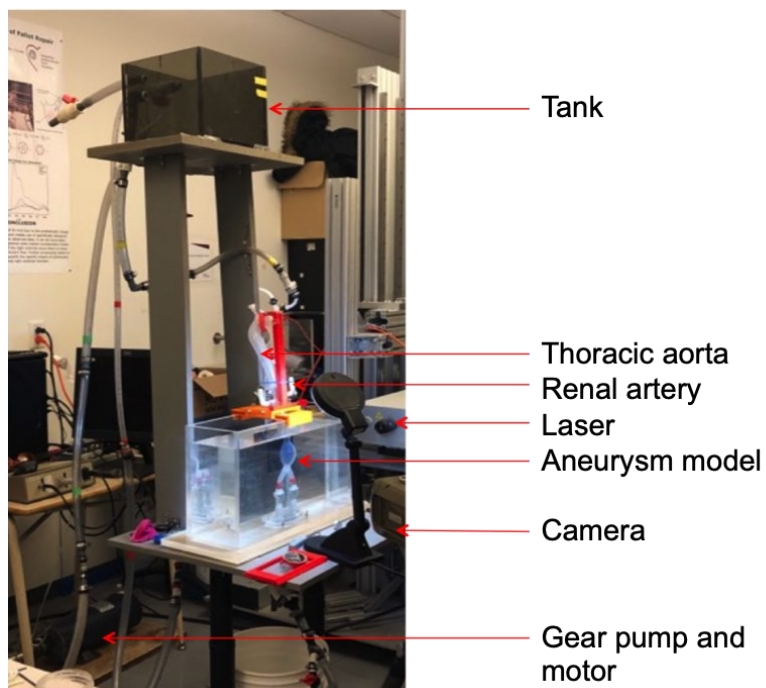


Figure 9: Experimental setup A) schematic B) in lab setup.

This experimental setup is a closed-flow loop. Three main parts can be identified: first, rigid wall tubes are used to connect the anatomical part of the model with a tank in both inlet and outlet. Second, the anatomical part of the model is itself divided in two. The first is an averaged model of the aortic arch, the thoracic aorta, and the renal arteries, created with flexible walls. The inlet of the ascending aorta includes a trileaflet bioprosthetic aortic valve (25 mm Perimount Theon RSR valve, Edwards Lifescience; Irvine, CA, US), this ensures the cardiac pulsatile behavior of the flow in our anatomical model. The outlets at the renal arteries end in a gate valve used to modify its resistance. The second part of the anatomical system is composed of a patient's specific abdominal aorta with or without aneurysm and a patient's specific iliac arteries. After the iliac arteries, a rigid outlet tube closes the loop by bringing the fluid back to the tank. Similarly, to the renal outlet, a gate valve allows for the adjustment in the resistance.

The pulsatile flow was imposed using a positive displacement gear pump coupled with a motor. This system was chosen for its ability to run continuously during an extended period of time. The control system used to run the motor uses multifunction input/output devices with a LabView (National Instruments, Austin, TX, US) program created to define varying control signals. The control signals were created are periodic with a waveform comprised of three distinct components: a positive half sine start of amplitude $A = 2.5 \text{ V}$ and duration $T/2 = 0.3 \text{ s}$ simulates the systole. A constant negative step of -0.5 V is then applied to close the leaflets of the aortic valve, followed by a constant null signal simulating the diastole. The diastolic time will be varied to reduce the period of the total signal, simulating the increase in heart rate under exercise conditions. Three conditions have been studied, with the respective heart rate of $r_1 = 60 \text{ bpm}$, $r_2 = 80 \text{ bpm}$, and $r_3 = 100 \text{ bpm}$, the signal waveform is depicted in [Figure 10](#)

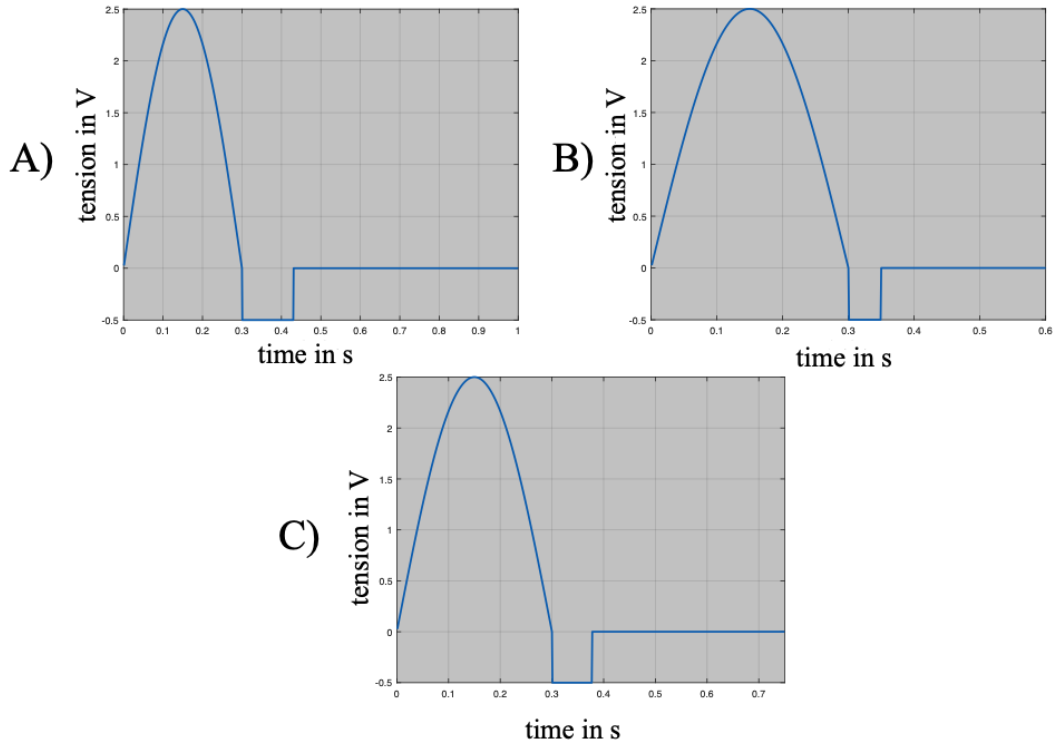


Figure 10: Motor control electrical waveforms: A) heart rate 60 bpm $T_1 = 1$ s, B) heart rate 80 bpm $T_2 = 0.75$ s, C) heart rate 100 bpm $T_3 = 0.6$ s

The flow imposed by the pump will fully develop in the rigid tubes before reaching the valve at the inlet of the ascending aorta. We characterize the flow using the Reynolds ($Re = \frac{\rho U D}{\mu}$) and Womersely ($Wo = \frac{D}{2} \sqrt{\frac{2\pi}{T\nu}}$) numbers. With U being the characteristic normal velocity of the cross-section post renal arteries, $D = 20$ mm the diameter of the cross-section, μ the dynamic viscosity of the fluid, ν its kinematic viscosity, and ρ its density. The Womersely numbers associated with the different heart rates are: $Wo_1 = 13.30$, $Wo_2 = 15.4$, and $Wo_3 = 17.2$. The averaged Reynolds numbers are: $Re_1 = 484$, $Re_2 = 592$, $Re_3 = 707$.

3.1.2 Pressure and flow validation

To reproduce a realistic waveform in an in vitro model, both an adequate input signal and lifelike impedance along the vascular model are needed. The compliant aortic model serves as a capacitor storing energy during systole, thus mimicking the behavior of real arteries. The peripheral resistance of the vascular system was reproduced by adjusting the above-mentioned outlet valves (section 3.1.1). Validation of the waveform was then done through pressure measurement, flow measurement, and preliminary velocity visualization.

The pressure was acquired at the end of the aortic arch and after the branch, using a fiber optic pressure sensor (FOP-M200) with an FPI-HR2 module (FISO Technologies Inc.; Quebec, QC, CA). The pressure probe was inserted into the model via a homeostasis valve fixed at the top of the aortic arch. Note that this port was also necessary to remove all air that would be trapped in the model after its initial filling. The EVOLUTION software (FISO Technologies Inc.; Quebec, QC, CA) is used with the pressure probe. Instantaneous pressure was acquired in resting conditions for a total of 10 heartbeats for two positions. In position 1, the systolic pressure was 130 mmHg, going down to 76 mmHg during the diastole. In the second condition, the peak systolic pressure is 163 mmHg and goes down to 104 mmHg during diastole. Those values and the pressure waveforms obtained are realistic. Indeed, ([Ku et al. 1997](#)), ([Les et al. 2010 a](#)) work on blood flow in arteries showed that hypertension is commonly found in patients with AAA and motivated the choice of a slightly high pressure. The instantaneous pressure measurement is reported in [Figure 11](#)

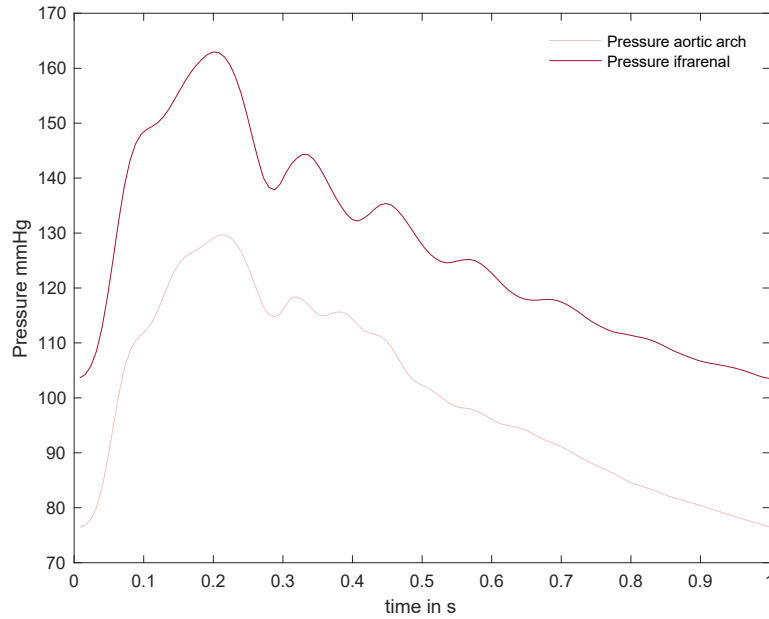


Figure 11: Experimental pressure waveforms.

The flow rate was measured on a cross-section under the renal arteries with a COidence flowprobe HQx 20AU (transonic, Quebec, QC, CQ), for vessel size 20 mm with a maximum flow rate of 50 L/min. The instantaneous volumetric flow is reported in [Figure 12](#). A total of 10 heartbeats are recorded, and the flow rate from beat to beat closely matches. We chose to present the flow as an ensemble average of 10 beats. The waveform shape is comparable to real flow waveforms from patients with AAA ([Fraser et al. 2008](#)). After some adjustments with the visualization of velocities using preliminary PIV tests (keeping velocities in ranges of 0 m/s to 0.6 m/s), the resting condition (60 bpm) showed a mean volumetric flow rate of $Q_1 = 1.6$ L/min and a maximum systolic peak of 6.7 L/min. The first increase in heart rate (80 bpm) brings the flow rate to an average of $Q_2 = 2.0$ L/min with a systolic peak of 6.3 L/min. Finally, with a heart rate of (100 bpm) the measured averaged flow rate is $Q_3 = 2.4$ L/min with a systolic peak of 6.5 L/min. average of 10 beats. The waveform shape is comparable to real flow waveforms from patients with AAA ([Fraser et al. 2008](#)). After some adjustments

with the visualisation of velocities using preliminary PIV tests (keeping velocities in ranges of 0 m/s to 0.6 m/s), the resting condition (60 bpm) showed a mean volumetric flow rate of $Q_1 = 1.6$ L/min and a maximum systolic peak of 6.7 L/min. The first increase in heart rate (80 bpm) brings the flow rate to an average to $Q_2 = 2.0$ L/min with a systolic peak of 6.3 L/min. Finally, with a heart rate of (100 bpm) the measured averaged flow rate is $Q_3 = 2.4$ L/min with a systolic peak of 6.5 L/min.

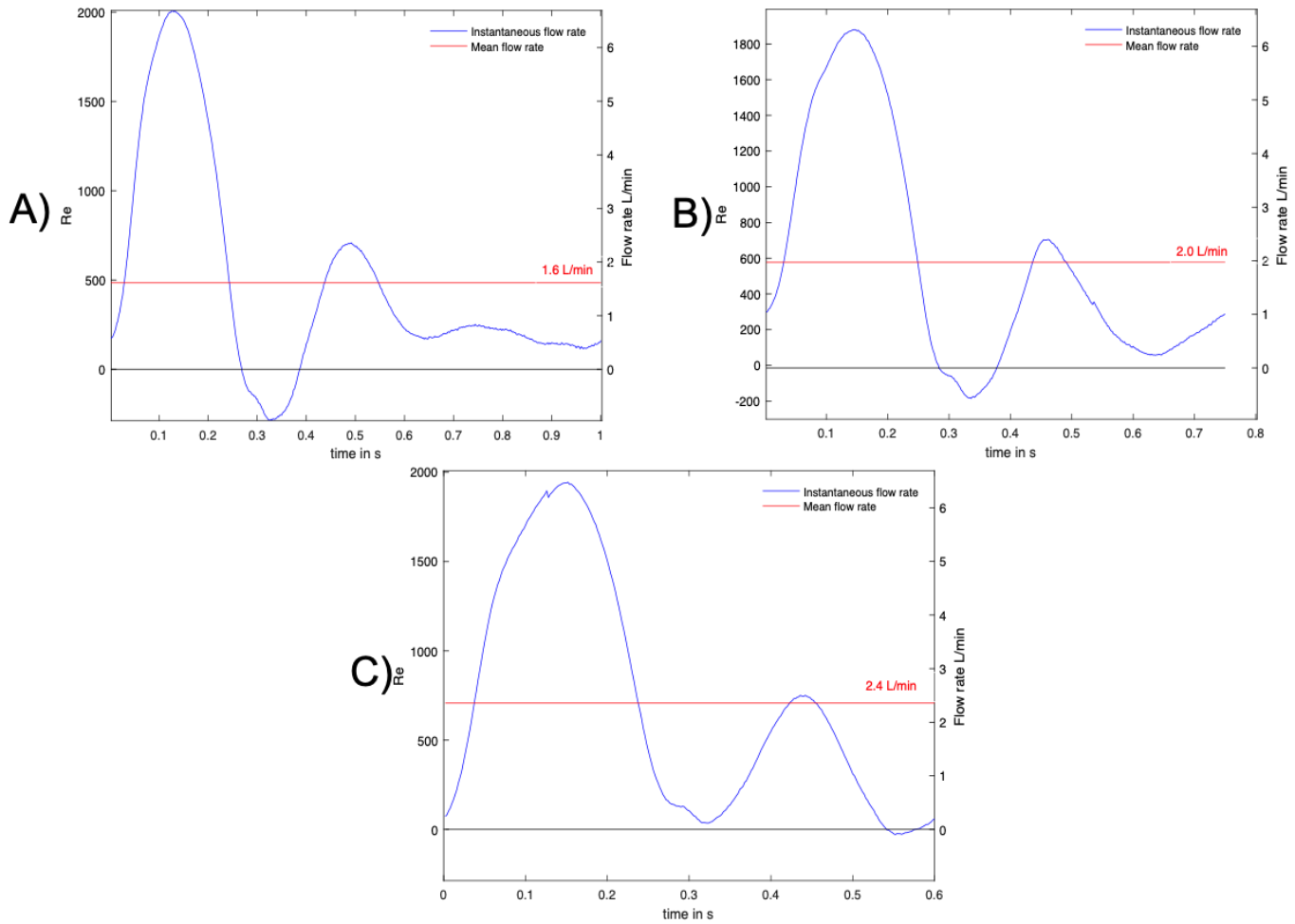


Figure 12: Volumetric Flow rate and instantaneous Reynolds number, A) $r_1 = 60$ bpm, 1 Hz
 B) $r_2 = 80$ bpm, 1.3 Hz, C) $r_3 = 100$ bpm, 1.7 Hz

3.1.3 AAA phantom

As stated in section 3.1.1 the aorta phantom is created from the aortic root to the iliac arteries with a patient-specific part including the abdominal aorta in the infrarenal region and the iliac arteries. The averaged model was designed to replicate the essential anatomical features of the human aorta, including its length, 3D curvature, the sinuses of Valsalva, and dimensions that match the average dimension of the human aorta ([Hager et al. 2002](#)). The aortic model starts with a diameter of 30 mm. It is kept constant up to the isthmus where it starts to diminish gradually up to the hiatus of the diaphragm where the diameter is fixed at 20 mm up to the

junction with the patient-specific model located 20 mm under the second renal artery. This aortic model has as its only branches the two renal arteries. Which are modeled by L-shaped branches, with a 11 mm diameter. They are positioned asymmetrically on the aorta.

Three patient-specific 3D models were used. Those models were obtained from CT scan images in DICOM format, which have been obtained from the Cardiovascular Surgery Department at the University Hospital of Zonguldak, Turkey. The first model does not present any aneurysm, while the second model presents a saccular aneurysm, and the third presents a fusiform aneurysm. The characteristic size of the saccular aneurysm is close to 40 mm which has been linked to an estimated annual risk of rupture of 0.5% to 5%. Concerning the fusiform model, it has a characteristic size of 70 mm linked to an annual rupture risk between 30% and 50%, as published by [\(Brewster et al. 2003\)](#). As previously stated, most *in vitro* AAA models are made with average models. In this study, we use patient-specific aneurysms, a more realistic approach.

[Figure 13](#) depicts the 3D models used.

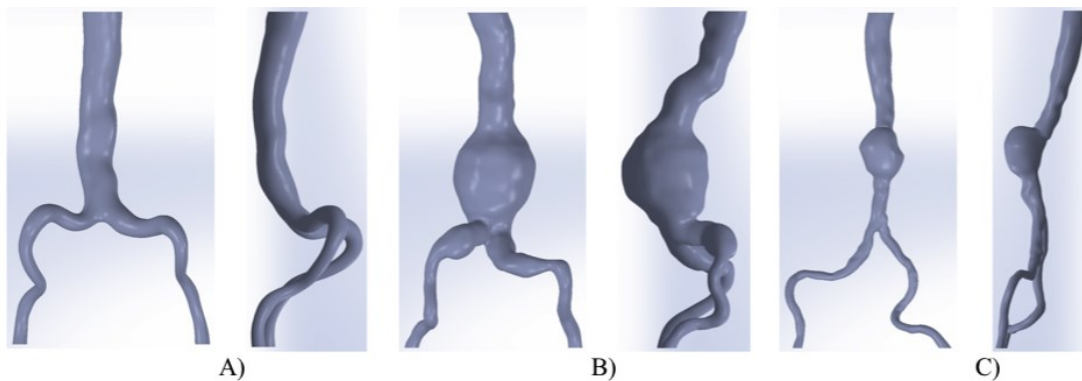


[Figure 13](#): The 3D-CAD models of the abdominal aorta. Posterior view (left) and left lateral view (right), A) Healthy aorta, B) Fusiform aneurysm, C) Saccular aneurysm.

The models created need to be compliant and transparent. To limit the risk of leakage or defect in the area of interest, they needed to be made in one piece. Molding techniques have

been used to produce vascular phantoms, however, the molds used are non-reusable. To create our AAA phantom, we opted for a brushing technique. From our initial 3D models, models of lumen were made as multiple pieces. Those pieces were printed using a LulzBolt TAZ6 (Fargo Additive Manufacturing Equipment 3D). The aneurysm bulge was printed using a flexible NinjaFlex 3D printer filament, which is composed of thermoplastic polyurethane (TPU) material. The flexible bulge is printed with a layer height of 0.1 mm and a 0-density infill. This flexibility will make the bulge removable from the phantom without damaging it. The rest of the lumen parts are printed with rigid thermoplastic aliphatic polyester material (PLA). The rigid parts are printed with a layer height of 0.2 mm and lightly sanded. All the lumen parts are then assembled using neodymium magnets. The obtained lumen is then placed on a frame, with two rotation axes, in a low-temperature-curing oven (40 to 50 degrees Celsius). A two-component silicone material (polycraft T-4 NBFiberglass Newtownabbey, ANT, NIR) is applied layer by layer on the model, between each layer the oven is turned on, and the frame is slowly rotated for a total curing time of 45 mins, the rotation smooths the layer. A layer of silicone is composed of 10 parts silicone base and 1 part curing agent the total mass used varies from model to model due to their varying size. The number of layers of silicone applied for every model is adjusted to reach a consistent wall thickness of 2 mm consistent with [\(Kemmerling et al.\)](#). The quality of the model is principally related to the transparency and regularity of the walls. The main source of defects comes from air bubbles trapped in the silicone when the base and curing agent are mixed. To remove those bubbles the mixture is placed under a vacuum pump for 10 min, then it is left for an additional 5 min to open air. If any bubble remains, they should be popped with a needle or pressed between the brush and the solid lumen. Lastly, we flip the model inside out and apply the two last layers on the inside face to smooth out any defect from the 3D-printed surface. The product has a shore hardness of 40 A, it provides sufficient flexibility to be removed from its mold

without tears, it has a 400% elongation at break and a 26 kN/m tear strength. The optically transparent refractive index of our model is 1.41 ± 0.01 . [Figure 14](#) shows a 3D-printed model and its corresponding silicone phantom.

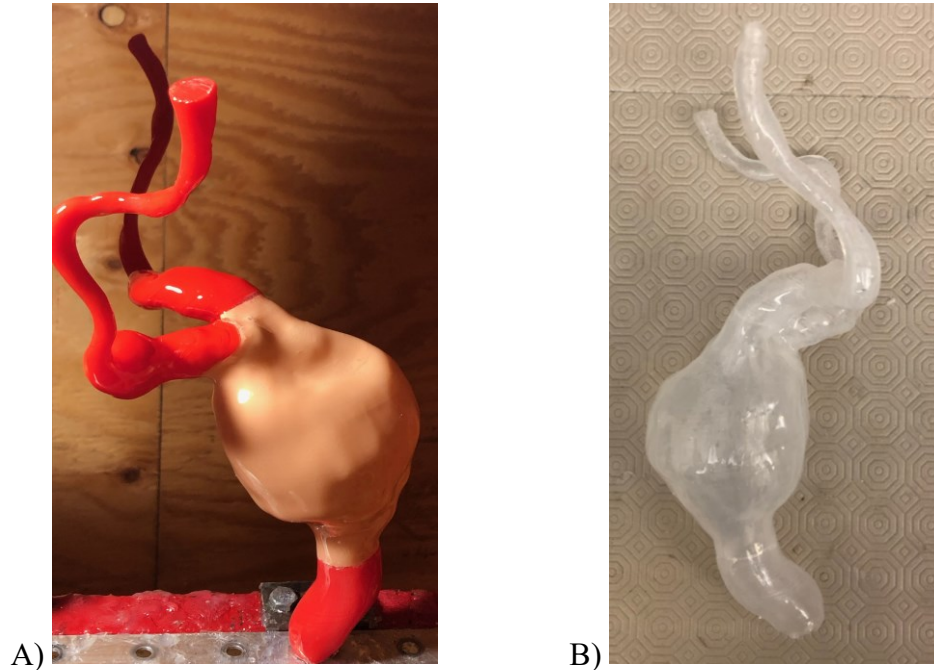


Figure 14: Fusiform AAA model, A) 3D printed Lumen, B) Silicone phantom

3.1.4 Blood-mimicking fluid

The working fluid chosen as a blood analog is a mix of 40% glycerol and 60% distilled water in volumetric fraction. The choice of this blood analog is motivated by two things; firstly, as we try to recreate realistic flow conditions, the blood analog needs to have a density and dynamic viscosity in realistic ranges compared to human blood. Secondly, as we are using PIV, we need to have a transparent working fluid with a Refractive Index (RI) matching the RI of the silicone phantom. As the density and viscosity of fluids are temperature-dependent, we will maintain our working fluid at room temperature (23.5 ± 0.5 ($^{\circ}\text{C}$)). The density of the blood analog was obtained by measuring the weight of a series of volumes of fluid, using a digital scale with a precision of 0.01 g. The water-glycerol mix has a density of $1106 \pm$

20 kg/m(23.5 ± 0.5 °C), which is close to the reported value of 1043-1060 kg/m³ for the density of blood ([Vitello et al. 2015](#)).

The viscosity was measured using a Cannon-Fenske routine viscometer (size 75, Cannon Instrument Company, State College, PA) which can accurately measure kinematic viscosity in the range (1.6 cSt to 8 cSt). The viscometer is calibrated by the manufacturer. The kinematic viscosity is obtained by measuring the time taken by the fluid to move down a capillary from the gravitational attraction. The viscometer is placed in a bath to stay at room temperature; the water glycerol is raised in the capillary above a starting mark by applying negative pressure, once the pressure is set back to its atmospheric level, the fluid will start falling. A stopwatch is started when a first mark is reached on the viscometer and stopped at a second. To limit human error, we repeated the process multiple times. An average kinematic viscosity is computed as the product of the time and the specific constant of the viscometer. The kinematic viscosity of the water-glycerol blood analogue is 3.7 ± 0.04 cSt which is in the viscometer measurement range. The dynamic viscosity is then computed as a product of the kinematic viscosity and the density and was 4.1 cP. ([Yousif et al. 2011](#)) reported blood's dynamic viscosity at body temperature (37 °C) to be 4.4 ± 0.5 cP. In terms of refractive index RI, we did not obtain an exact match with the silicone used in the AAA phantoms but the blood analog RI of 1.39 was sufficiently close to the silicone RI to give a clear view of the moving fluid. Moreover, the calibration of PIV will take the difference into account. Changes to the working fluid could increase the RI similarity. One possibility would be to add sodium iodide (NaI) to a water-glycerol to increase the solution RI without changing the fluid viscosity. However, the first issue of this addition is that the resulting fluid density would be much higher than that of blood. Moreover, NaI solutions are harmful at high concentrations, considering the important fluid quantities that needed to be handled for this experiment, it was decided that NaI was to be excluded. It is also notably expensive. Another solution would be

to add urea to a water-glycerol solution to yield a refractive index closer to 1.41 with a matching blood density and viscosity ([Brindise et al. 2018](#)). Indeed, a water-glycerol-urea solution seemed interesting, additional tests should be done. Lastly, the possibility of mimicking the non-Newtonian behavior of blood is to be investigated. The shear-thinning of the blood should not be major in large vessels like the abdominal aorta. The blood mainly behaves as a Newtonian fluid ([Valchopoulos et al. 2011](#)). It is expected that it will be so as long as the vessel diameter is greater than 0.5mm. However, some studies have used xanthan gum in their blood-mimicking solution to model the macroscopic non-Newtonian behavior of blood ([Deplano et al. 2014](#)). Also, it is interesting to be able to analyze non-Newtonian behavior, adding Xanthan gum could reduce the accuracy of our results. The use of the gear pump to actuate the system generates large deformations, those deformations are localized and do not impact the flow in the AAA, but they can deteriorate the xanthan molecular network and reduce the overall dynamic viscosity ([Benard et al. 2007](#)). It is expected that it will be so as long as the vessel diameter is greater than 0.5mm. However, some studies have used xanthan gum in their blood-mimicking solution to model the macroscopic non-Newtonian behaviour of blood ([Deplano et al. 2014](#)). Also, it is interesting to be able to analyze non-Newtonian behaviour, adding Xanthan gum could reduce the accuracy of our results. The use of the gear pump to actuate the system generates large deformations, those deformations are localized and do not impact the flow in the AAA, but they can deteriorate the xanthan molecular network and reduce the overall dynamic viscosity ([Benard et al. 2007](#)).

3.2 Particle Image Velocimetry

The velocity fields in the abdominal aorta and AAA are investigated in a succession of planes using two-dimensional time-resolved particle image velocimetry. The details of this measuring method and its core concepts are presented in this section.

3.2.1 Basic principles

To visualize the inner movement of a fluid body is particularly complicated. Any probe contact will inevitably deform the flow, and visual observation of the flow is only possible as a bulk body. The only way to see those inner motions is through the movement of outside bodies (particles or bubbles) carried by the flow. Dyes have been used to visualize simple flows and are used for the visualization of the transition between laminar to turbulent regimes. Visualization through dyes only gives us the path lines from one given point and a qualitative idea of the movement of the flow. Using PIV, digital image processing allows us to obtain an instantaneous Eulerian velocity field from the visualization of moving particles in the studied velocity field. As stated, we will use two-components, two-dimensions PIV (2D-2C PIV) but we will refer to it simply as PIV.

To perform PIV the working fluid is seeded with properly selected tracer particles, then a laser sheet is used to illuminate the flow twice in rapid succession. The time between two exposures will be used to determine the velocity of the flow at a given instant. The light scattered by the particles will allow the visualization of the flow in the plan. A camera is positioned perpendicular to the investigated plan. Depending on the setup, the camera will film either as a section of snapshot where two successive snapshots will be used as the two pictures used for velocity calculation or as a film of a pair of pictures where one instant of the film is divided into two frames. The small time difference between those two frames is used to compute instantaneous velocities. Those methods are usually called double-frame or single-

frame PIV. A calibration of the imaging system is done so that the pixel value of the image relates to the real dimensions of the velocity field. The image is then divided into smaller sub-areas, the areas of interrogation, around a point of the Eulerian field, assuming uniform displacement of the surrounding particle. Corresponding interrogation areas between pairs of pictures are compared via a cross-correlation technique yielding the most probable displacement of the particles. This process will create a velocity map at every snapshot of the film. The process of velocity vector calculations is briefly sketched in [Figure 15](#).

This method assumes that the particles closely follow the fluid motion and that the local flow velocities can be deduced from particle velocities. The obtained vector field is then analyzed and processed under different validation criteria, outlier vectors are replaced creating a 2D Eulerian velocity field which can be used to compute different parameters like; velocity gradients, shear stresses, or energy loss.

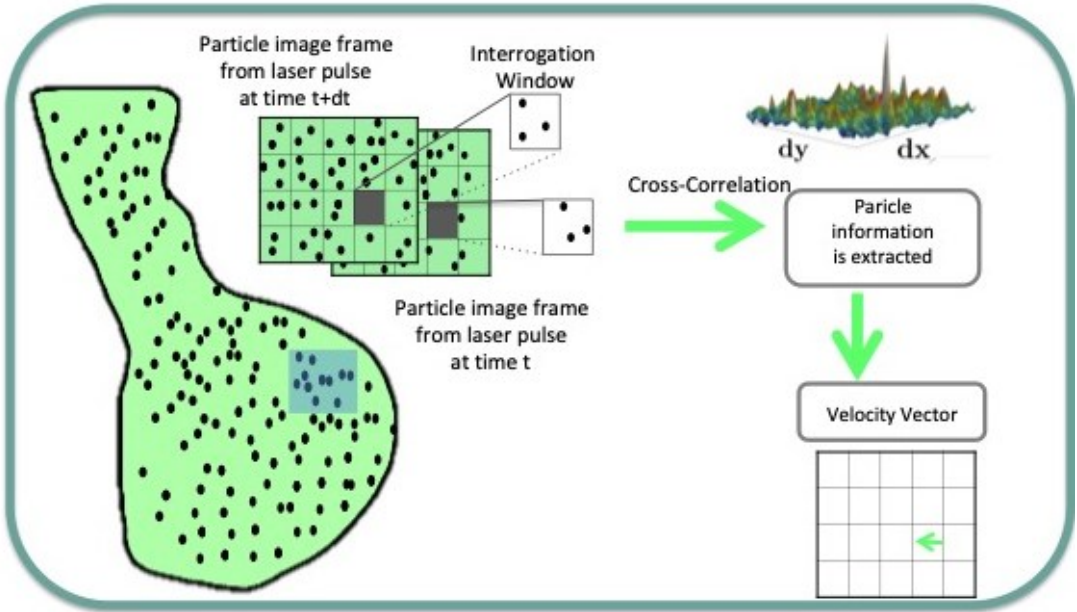
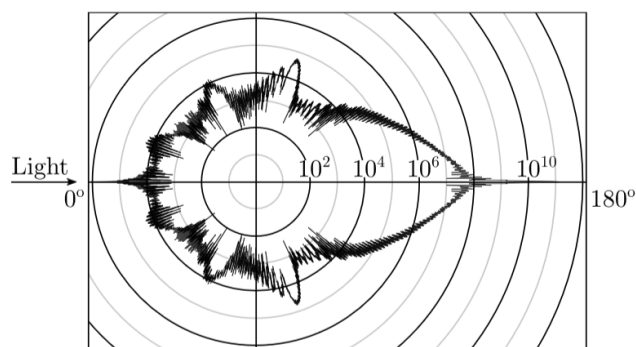


Figure 15 Main concept of velocity vector computation in 2 components planar PIV

3.2.2 Experimental setup

As stated, the success of a PIV setup starts with the choice of the particles. Particles are selected as a function of their shape, size, and material, which are the characteristics impacting their optical behavior as well as their interaction with the fluid flow. The material's density should be close to the working fluid's density, so the particles are neutrally buoyant. The optimal size of the particle is a compromise between its visibility and its impact on the flow. Bigger particles scatter more light and are therefore easier to see, whereas smaller particles follow faithfully the fluid motion. Polyamide particles with a nearly spherical shape are used in this setup; their mean diameter is $d_p = 50 \mu\text{m}$ with a deviation of $20 \mu\text{m}$ (PSP-50 Dantec Dynamics; Skovlunde, CPH, DK) and a density of 1030 kg/m^3 . Those particles are sufficiently neutrally buoyant in the water-glycerol blood analog used. The refractive index of the particles is $n_p = 1.5$ as the wavelength of the light source is 527 nm , the particles are subjected to Mie scattering ($d_p \gg \lambda_{PIV}$). Therefore, the forward scattering of light of the particles is more intense than the scattering of light perpendicular to the laser sheet. However, it is sufficient to visualize the particle.

[Figure 16](#) represents the intensity distribution of scattered light by the chosen particles at the wavelength λ_{PIV} .



[Figure 16](#): Normalized light scattering intensity by the selected tracker particle ([Di Labbio 2019](#)).

The time response of the particles is $\tau_0 = d_p^2 \rho_p / 18\mu$ which corresponds to a settling velocity of approximately 20 $\mu\text{m/s}$, taking the acceleration phase of the systole as the characteristic time of the flow ($t_0 \approx 0.1\text{ s}$). The identification of the uncertainty in the velocity field associated with the choice of the article is not an easy task, however when the particles are properly selected, which is the case according to the guidelines in ([Adrian et al. 2011](#)), the error should not be over 1%. Particles heavier than the fluid tend to under-respond, while particles lighter will over-respond. In our case, the uncertainty presents a bias toward higher velocities magnitude. However, this uncertainty is acceptable for this work. Also, Brownian motions will not impact the results as they are important when particle size is in the range of 50 nm to 500 nm and velocities in the range of 1 mm/s, as discussed in ([Raffel et al. 2018](#)).

To limit optical deformation from the curved surface of the phantom, the test section is immersed in a tank containing the same working fluid as the one used as a blood analog. The tank is made of transparent acrylic material with a similar RI as the silicone phantom and working fluid.

The field of view starts with the proximal neck of the aneurysm under the renal arteries, which only serves to simulate a realistic flow, and stops at the aortic bifurcation. A thin light sheet illuminates the test section with a presumed uniform intensity parallel to the field of view. It is generated with a diode-pumped Nd:YLF laser (LDY301, Litron; Rugby, Warks, GB) which emits light pulses of wavelength lasting $100 \lambda_{PIV} = 527\text{ nm}$ kHz to 20 kHz. The maximum energy per pulse is 10 mJ. The light sheet is emitted toward the test section using a cylindrical lens while a second lens is used to tune its width ($\approx 1\text{ mm}$).

The acquisition of images is done using a phantom V310, Vision Reseach Inc.; Wayne, NJ, US) with AF Micro NIKKOR 60 mm f/2.8D lens (Nikon; Tokyo, JP). It has a maximum frequency of 3250 Hz with a resolution of 1280 x 800 pixel frame. The camera was placed

with its sidewalls parallel to the sidewalls of the acrylic tank. Having the laser, acrylic tank, and camera well placed limits the problems associated with small RI mismatch. One last parameter to consider is that the size of the particles on the screen is not too small to limit a systematic error called peak-locking, which occurs when the continuous intensity distribution of a very small particle image is insufficiently sampled by the discretized camera sensor. If the low intensities of the pixel next to the one containing the maximum intensity of a particle image are of the order of magnitude of the image noise level, the sub-pixel position of the particle is lost.

As multiple planes are investigated in every model, the calibration of the real dimension of the image is done for every plan. To be perfectly set on the investigated plan, the calibrations are done using the known dimension of the phantom. Every plane has its own calibration coefficient, but they are all of the order of magnitude of 8 px/mm.

We use a double-frame single exposure PIV approach in this work. To minimize in-plane particle loss, it is required that the fast particles do not move more than 1/4 of the interrogation area, or if a multi-pass approach is used 1/4 of the initial window size ([Adrian et al. 2011](#)). In our case, 48 x 48 pixels. Therefore, a limit of displacement of 12 pixels is to be respected. In this work, the fastest identified particles follow those guidelines, it is expected that any slower particle will. Using iterative evaluation with a window-shifting technique in the PIV computation algorithm allows in-plane losses to be treated with conformity to this 1/4 rule while maximizing the spatial resolution. As the large interrogation windows limit in-plane losses of particle and the small interrogation window increase the resolution ([Scarano et al. 2000](#)). Regarding the out-of-plane loss of pairs, it is recommended to keep the number of particle pairs within the interrogation window generally around five ([Scharnowski et al. 2017](#)).

The acquisition parameters of our PIV setup are the following: A constant acquisition frequency of 240 Hz was used, it denotes the time between the acquisition of each pair of pictures in the double-frame PIV scheme; The time difference between frames was $dt = 2400 \mu\text{s}$. Those values are constant for every case studied, and the number of pictures varied to reflect a time closely matching 10 heart beats (2400 pictures, 1800 pictures, and 1440 pictures); The flow actuation was run ahead of the acquisition to remove perturbations from transient effects. However, due to the relatively slow motion of the flow, the run time of the experiment was kept as short as possible as the particles tend to stick to the anterior wall due to flow stagnation, partially covering the flow from the camera. The phantoms were therefore regularly cleaned to ensure optimal visibility.

Multiple studies assumed that the flow in AAA could be considered 2D as the velocity normal to the plane is relatively small ([Norouzi 2020](#)), ([Deplano et al. 2007](#)). To capture some of the third velocity component ([Deplano et al. 2016](#)), used stereo PIV, but only at a specific time instant. In this study, multiple perpendicular planes have been visualized in every case in order to have a better evaluation of the 3D motion of the flow.

Working fluid properties	Water-glycerol ratio	60 - 40 (volume %)
	Density	$1106 \pm 20 \text{ kg/m}^3$
	Dynamic viscosity	0.0041 Pa*s
	Refractive Index	1.39
	Temperature	$23.5 \pm 0.5 \text{ }^\circ\text{C}$
Simulator operating conditions	Infrarenal average flow rate	$Q_1 = 1.4 \text{ L/min}$
		$Q_2 = 2.0 \text{ L/min}$
		$Q_3 = 2.4 \text{ L/min}$
	Cardiac periods	$T_1 = 1 \text{ s}$
		$T_2 = 0.75 \text{ s}$
		$T_3 = 0.6 \text{ s}$
	Heart rates	60 bpm
		80 bpm
		100 bpm
	Systolic pressure	163 mmHg
Diastolic pressure	104 mmHg	
Image acquisition settings	Number of images (n_i)	$n_1 = 2400$
		$n_2 = 1800$
		$n_3 = 1440$
	Frequency (f)	$f = 240 \text{ Hz}$
	Laser time delay (dt)	$dt = 2000 \text{ } \mu\text{s}$

Table 1: Experimental setup parameters

3.3 Processing

3.3.1 Image pre-processing

Before calculating the velocity field from the acquired images, some numerical filters are applied to remove possible image defects. Mainly the background image and diffuse reflections caused by the complex topology of the aneurysm walls are sources of errors in the velocity calculations. We consider that the background images or anything fixed in time can only be a source of error. To remove it, an average image is created from a total of 10 heart beats. This average image is subtracted from every snapshot. It was identified that large intensity fluctuation still existed in the obtained pictures, therefore a subtract fluctuating

averaged scheme was used. This scheme works as a high pass filter, removing large intensity fluctuations without impacting short fluctuations from the particle signal.

A coarse fixed mask is created including the movement of the aneurysm wall, to reduce computation time; a finer dynamic mask will be applied to the vector fields after computation. The pre-processing was made using the commercial software LaVision Davis version 8.4.0.

3.3.2 Computation of the velocities

For every pair of pictures obtained and pre-processed, vector fields are calculated using the commercial software LaVision Davis version 8.4.0. A statistical evaluation of both frames of every pair is done to match particles identifying the displacement between each frame distribution of particles. Both images are divided into small interrogation windows. The evaluation uses a cross-correlation standard fast Fourier transform. A multi-pass scheme is implemented, comparing results from varying interrogation window sizes with a round Gaussian function. The starting interrogation area is 48 x 48 pixels, it is halved to 24 x 24 and then halved to 12 x 12 pixels. Using a large starting interrogation area ensures that the 1/4 rule mentioned in section 3.2.2 was respected, while the smaller final interrogation area increases the spatial resolution. Furthermore, the resolution was increased by a 50% overlap in the interrogation region. The final spatial resolution of the measurements is around 0.75 mm, depending on the specific calibration of every plane investigated.

A PIV sliding sum-of-correlation is used to improve the precision of the correlation map. Correlation maps are compared in a small variation of time (time filter length N) in order to increase the correlation peaks. The correlation maps are added with a Gaussian bell-weighting factor dampening the effect on the studied time instant of the correlation map further away in time. This method uses the comparison of time neighboring displacement maps to reduce errors, it works best in flow with small displacement. A number of PIV recordings were used

to compute velocities with and without a sliding sum-of-correlation scheme. For every test, the resulting flow field closely matches. However, more outliers (false vectors) are detected when the sliding sum-of-correlation scheme is not used. The time filter used in this study is $N = 2$.

In order to detect velocity outliers, a local median filter is applied twice. This method, proposed by [\(Westerweel et Scarano 2005\)](#), recognizes a vector as valid if its variation from a local average divided by the standard deviation of the neighboring vectors is lower than a specific threshold. This method is independent of the frame of reference; spurious vectors in moving flow structures and fixed flow structures are detected equally. It is also independent of the vector norms. The threshold is proportional to the standard deviation which increases with the velocity gradient. In this work, the neighboring vectors in a 5 x 5 area are compared. If a spurious vector is detected, it is not considered for average and deviation computations, the other three highest correlation peaks (stored in the vector buffer) are used to replace the false vector. The peak ratio factor Q is also used to identify false vectors, $Q = \frac{P_1 - \min}{P_2 - \min}$ where P_1 and P_2 are the first and second highest correlation peaks and min is the lowest value of the correlation plane. A peak ratio factor Q close to 1 implies that the highest peak is likely a false random peak, in this work vectors with $Q < 1.1$ are removed. Empty spaces are filled by interpolation, averaging 4 valid neighbor vectors. A simple 5 x 5 smoothing is finally applied to reduce noise. Following [\(Raffel et al. 2018\)](#). guidelines, it is estimated that the uncertainty of the PIV data is less than 5%.

3.3.3 Velocity gradients calculation

A result of the 2D PIV is that only two components of velocity in two directions are available (u,v in directions x,y). As a result, only some secondary dynamic values can be computed. Namely, we can compute the out-of-plane vorticity component w_z and the in-plane shearing

and elongation strain. Since the velocities are projected on a 2D plan, finite differencing has to be used to estimate the velocity gradients. To reduce the truncation error, a noise-optimized fourth-order scheme is used. The compact-Richardson scheme is applied to the grid point inside the flow domain.

$$\frac{\partial u}{\partial x}\bigg|_k = \sum_{j=1,2,4,8} \frac{w_j}{w} \frac{\partial u}{\partial x}\bigg|_{kj}$$

with: $w = 1239, w_1 = 279, w_2 = 1036, w_4 = 0, w_8 = -69$

$$\frac{\partial u}{\partial x}\bigg|_{k-1,j} + \frac{\partial u}{\partial x}\bigg|_{k,j} + \frac{\partial u}{\partial x}\bigg|_{k+1,j} = a \frac{u_{k+1,j} - u_{k-1,j}}{2j\Delta x}$$

$$\text{with } a = \frac{3}{2}$$

For the nodes at the boundary, a forward compact scheme with the highest possible order corresponding to the available points is used, ([Etebari et al. 2005](#)).

The uncertainty in the velocity gradients is proportional to the uncertainty estimation in the velocity deviated by local spatial differences Δx on the neighboring data. The uncertainty in the velocity gradient will be around 10% for interior grid points and 20% for grid points close to the wall ([Di Labbio et al. 2019](#)).

3.3.4 Viscous energy dissipation

With the velocity gradient calculated, it is possible to calculate the energy loss in the AAA. This is done by computing the viscous energy dissipation rate VED_r and the total energy loss during the cardiac cycle. VED_r is a measure of how adversely the flow is losing its kinetic energy due to viscous friction and deformation. As previously mentioned, VED_r is clinically significant as it represents the adverse workload to the function of the cardiovascular system. It is classically defined as the scalar product of viscous stress ((τ)) and strain rate (S). In the

case of a 2D incompressible flow field similar to those obtained with 2D PIV, VDE_r is calculated via the following equation, [\(Pedrizzetti et al. 2005\)](#). In the case of a 2D incompressible flow field similar to those obtained with 2D PIV, VDE_r is calculated via the following equation, from [\(Pedrizzetti et al. 2005\)](#).

$$VDE_r = \frac{\mu}{2} \int_A \left(\sum_{i,j} \left(\frac{\partial v_i}{\partial x_j} + \frac{\partial v_j}{\partial x_i} \right)^2 \right) dA \quad i, j = 1, 2$$

Where μ is the dynamic viscosity of blood, V is the velocity vector, and i and j account for the coordinates of the 2D Cartesian coordinate system. Note that the total dissipation rate is obtained by integrating the VDE_r over the total domain for all time instants.

3.3.5 Proper orthogonal decomposition

As previously mentioned, Proper Orthogonal Decomposition is used to decompose a dataset into a linear combination of a set of modes, and their corresponding expansion coefficients. A space-only POD method was used in this work. The resulting modes are spatially dependent $\phi_j(x)$ and have time dependent weight ($b_j(t)$).

The first step of the POD scheme is to reorganize the data into a tall matrix X , called the snapshot matrix, containing every snapshot of the velocity field recordings. A column of X is a vector $x(t_k)$ itself containing every velocity component, u and v forming the velocity field at every spatial grid point.

$$X = [x(t_1) \ x(t_2) \ \dots \ x(t_k) \ x(t_n)]; x(t_k) = \begin{bmatrix} u_{1k} \\ u_{2k} \\ \vdots \\ u_{mk} \\ v_{1k} \\ v_{2k} \\ \vdots \\ v_{mk} \end{bmatrix}$$

The number of snapshots is in $[1,n]$ and the number of spatial grid points is in $[1,m]$.

It is a common practice in modal studies to focus on structure associated with fluctuation, for this purpose, the temporal mean of the vector field is often subtracted from the vector field.

This was not done in this work as the mean flow can be used as a reference when comparing lower-ranking modes, it is also essential to reconstruct the flow field using a truncated number of modes.

When the flow data are properly arranged, three different approaches exist. The classical POD method, the method of snapshots, and the singular value decomposition (SVD).

The classical POD method involves solving the eigenvalue problem of size $2m \times 2m$ for the covariance matrix of $R = XX^T$. The computed eigenvectors are known as the POD modes and their eigenvalue corresponds to the kinetic energy captured by respective POD modes. In the case of PIV measurement, vector fields include a significantly high number of grid points, compared with the number of snapshots $m \gg n$. In this study, if we simply consider the duration of the PIV measurements as one heartbeat, with $T_l = 1$ s, we will get $n = 240$ snapshots, for grid points. Therefore, it is not practical to solve the $2m \times 2m$ eigenvalue problem.

The method of snapshots addresses this issue by replacing the covariance matrix with the temporal correlation matrix $C = X^T X$ with a smaller size $n \times n$ ([Sirovich et al. 1987](#)). This method relies on the similarity of the nonzero eigenvalues yielded from both eigenvalue problems.

$$C = \sum_{i=1}^n (x(t_i)^T x(t_i)) = X^T X$$

Since the velocity vectors are chosen for the decomposition, the resulting eigenvalues (λ_j) determine the kinetic energy content of the POD modes. Those eigenvalues are stored in decreasing order relative to their energy content.

$$C\psi_j = \psi_j\lambda_j, \quad \psi_j \in \mathbb{R}^n, \quad \lambda_1 \geq \dots \geq \lambda_n \geq 0$$

$$C\Psi = \Psi\Lambda$$

Ψ denotes the eigenvectors of the temporal correlation matrix and Λ is the diagonal matrix of eigenvalues. The eigenvectors of the temporal correlation matrix C make up an expansion basis to recover the eigenvectors of the original covariance matrix R , or POD mode (ϕ_j).

$$\phi_j = \frac{x\psi_j}{\sqrt{\lambda_j}} \quad \Phi = \frac{x\Psi}{\sqrt{\Lambda}}$$

The flow at each time instant can be represented by a linear combination of modes

$$X = \sum_{j=1}^n b_j(t)\phi_j(x)$$

$$B = \Phi^T X$$

As mentioned, another POD method is SVD which does not use a correlation matrix and is more robust to round off errors. However, it is not the method of choice for large datasets ([Taira et al. 2017](#)).

In this work the snapshot method is then used, it is illustrated in [Figure 17](#)

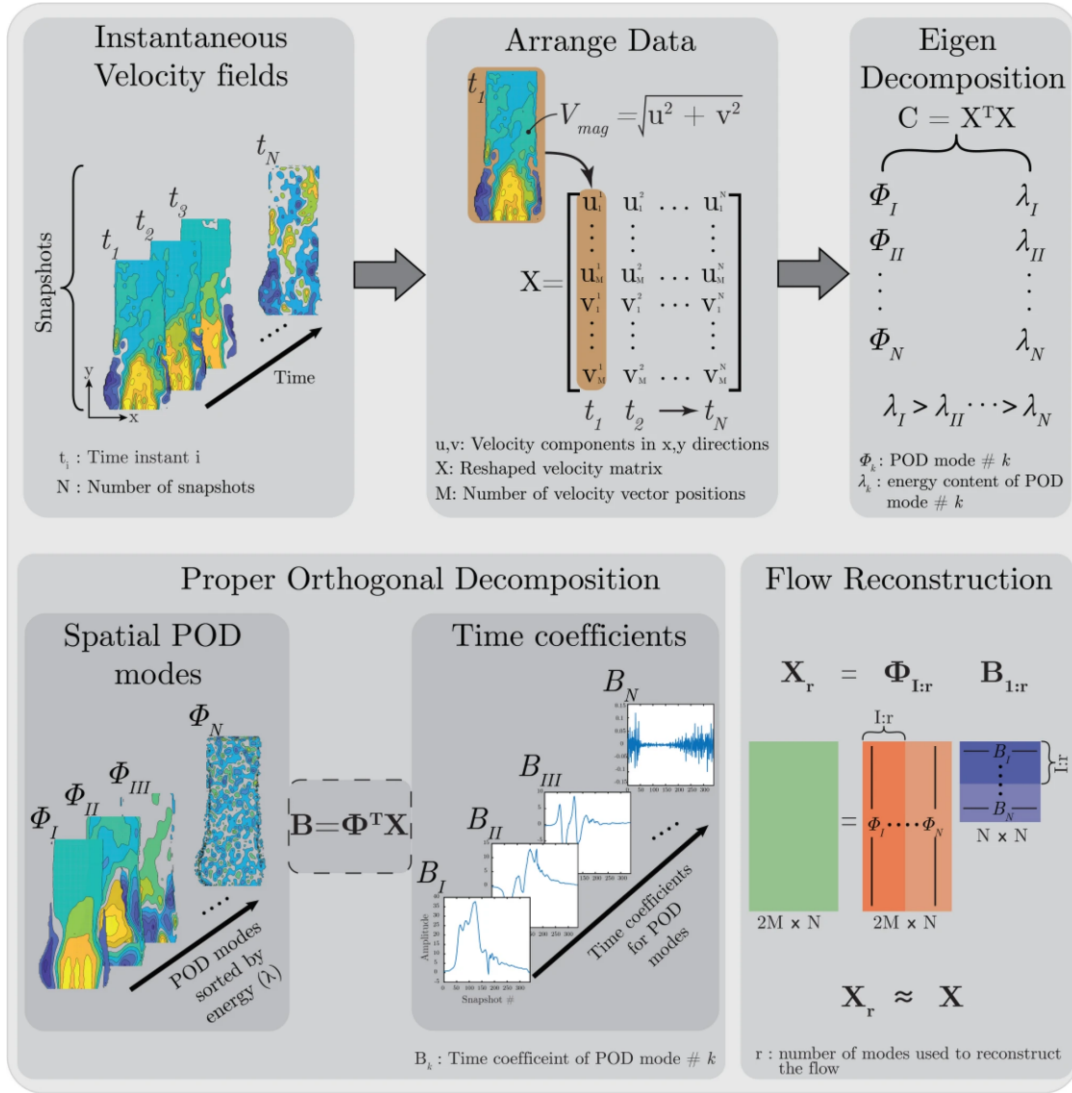


Figure 17: Proper orthogonal decomposition snapshot method from (Darwish et al. 2021).

Finally, the Shannon or global entropy, H , of the decomposition is computed. This parameter can represent the energy distribution among different modes. H varies between 0 and 1, it has a minimal value if all the energy is captured by the first mode and is equal to 1 if all the eigenvalues are equal, meaning an equal repartition of energy in the structures.

$$H = -\frac{1}{\ln(n)} \sum_{i=1}^n p_i \ln(p_i) \quad p_i = \frac{\lambda_i}{\text{tr}(\Lambda)}$$

p_i is the ratio between the eigenvalue and the global energy.

4 Results

The results of this work are presented in the following section. As explained in section 3.1.2, the results of the flow and pressure study were used to validate the experimental setup. The velocity fields were recorded using a multi-plan 2D PIV. Planes are selected perpendicular to either the sagittal or coronal plan. In total two planes are investigated for the healthy aorta, 8 are investigated for the saccular AAA model, and 10 for the fusiform AAA model.

4.1 Instantaneous velocity field

4.1.1 Healthy aorta

The planes chosen in the healthy aorta are one plane parallel to the coronal plane, plane A, and the other parallel to the median plane. The plane B position was chosen to capture the exit of the flow in one of the iliac arteries and the flow in the aorta. The two planes investigated are presented in [Figure 18](#).

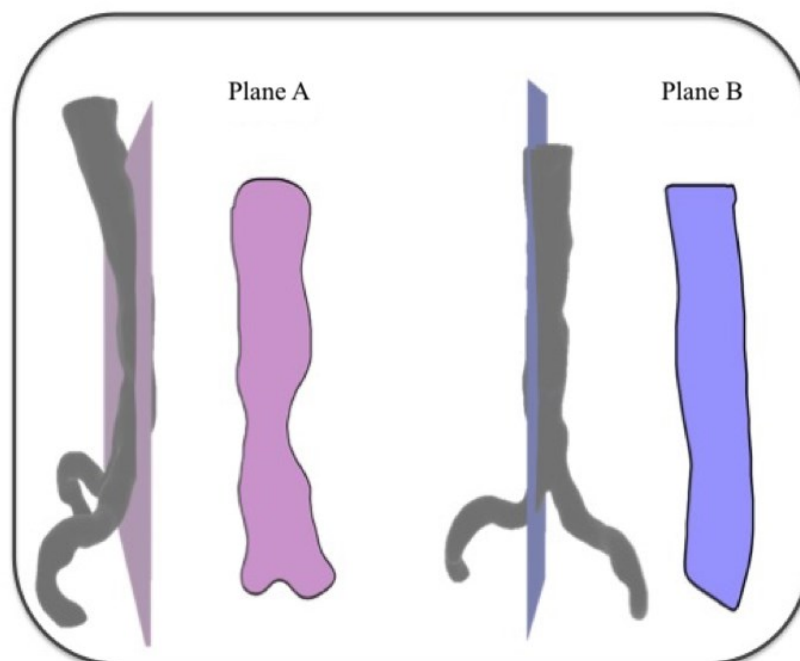


Figure 18: Planes investigated for the healthy aorta.

4.1.1.1 Velocity fields at rest, healthy aorta.

The velocity fields obtained in the healthy aorta are used as a reference for comparison. Measurements in healthy abdominal flow observed in our model were similar to those described in the literature. Starting with the period $T_I = 1$ s (60 bpm), the flow shows patterns resembling the laminar flow during the acceleration phases of the systole with few transient separations observed. During the systolic deceleration, transitional effects are observed as random fluctuation in the flow. The complex topology of this patient-specific aorta (varying lumen diameter) seems to facilitate the transition and the formation of vortices. A separation towards the posterior wall, caused by the lumbar curvature, is observed and it creates a preferential area for a backward flow to manifest toward the end of the systole and beginning of the diastole. As seen on the flow rate waveform a rebound of the flow is visible during diastole, however, most of the diastole is characterized by a low-velocity flow where some vortices are maintained. Snapshots of the velocity field are shown in [Figure 19](#) and [Figure 20](#).

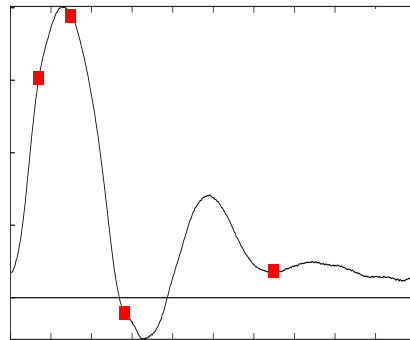
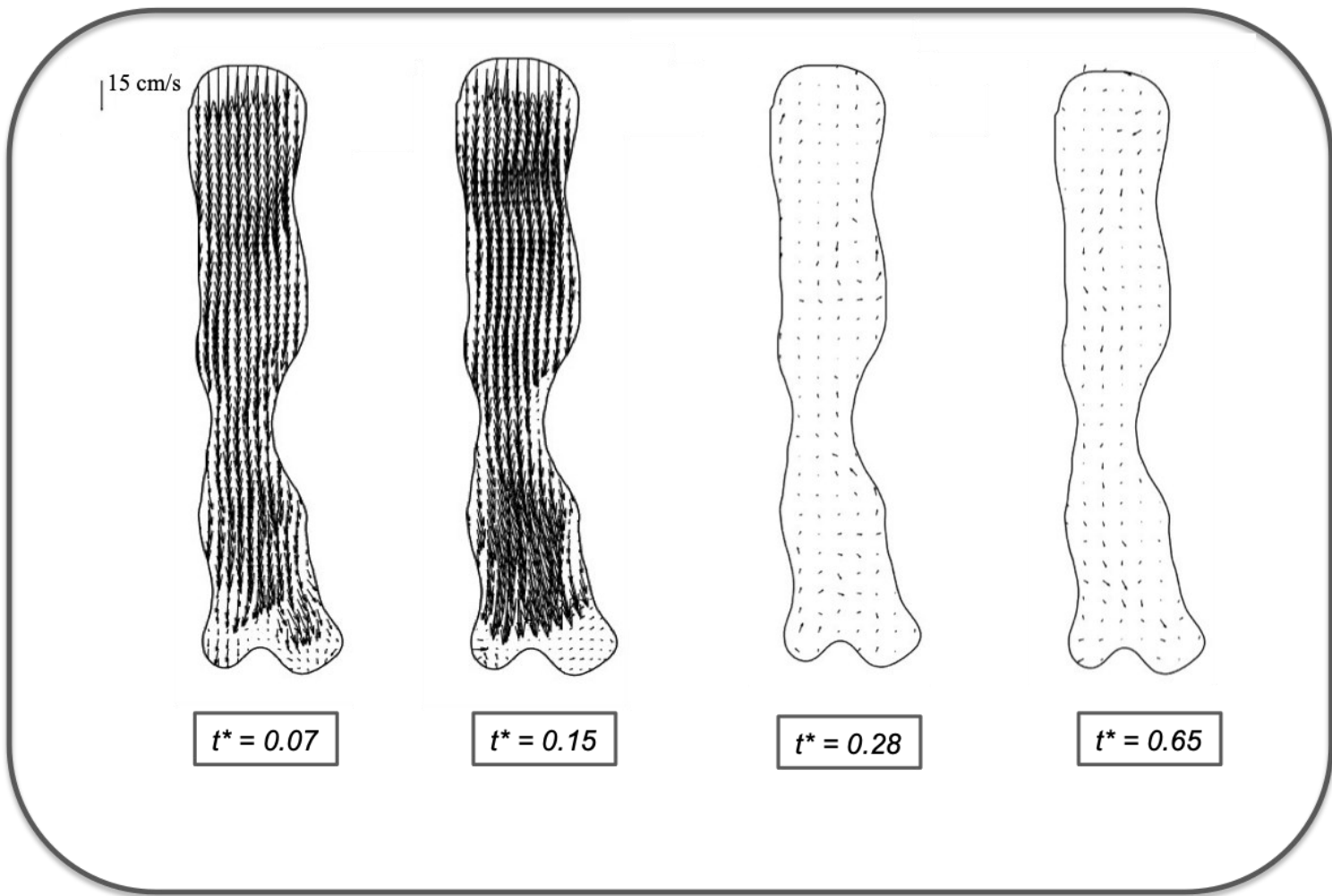


Figure 19: Velocity field snapshots, Healthy aorta plane A; The dimensionless times ($t^* = t/T_1$) are indicated in red on the flow waveform graph

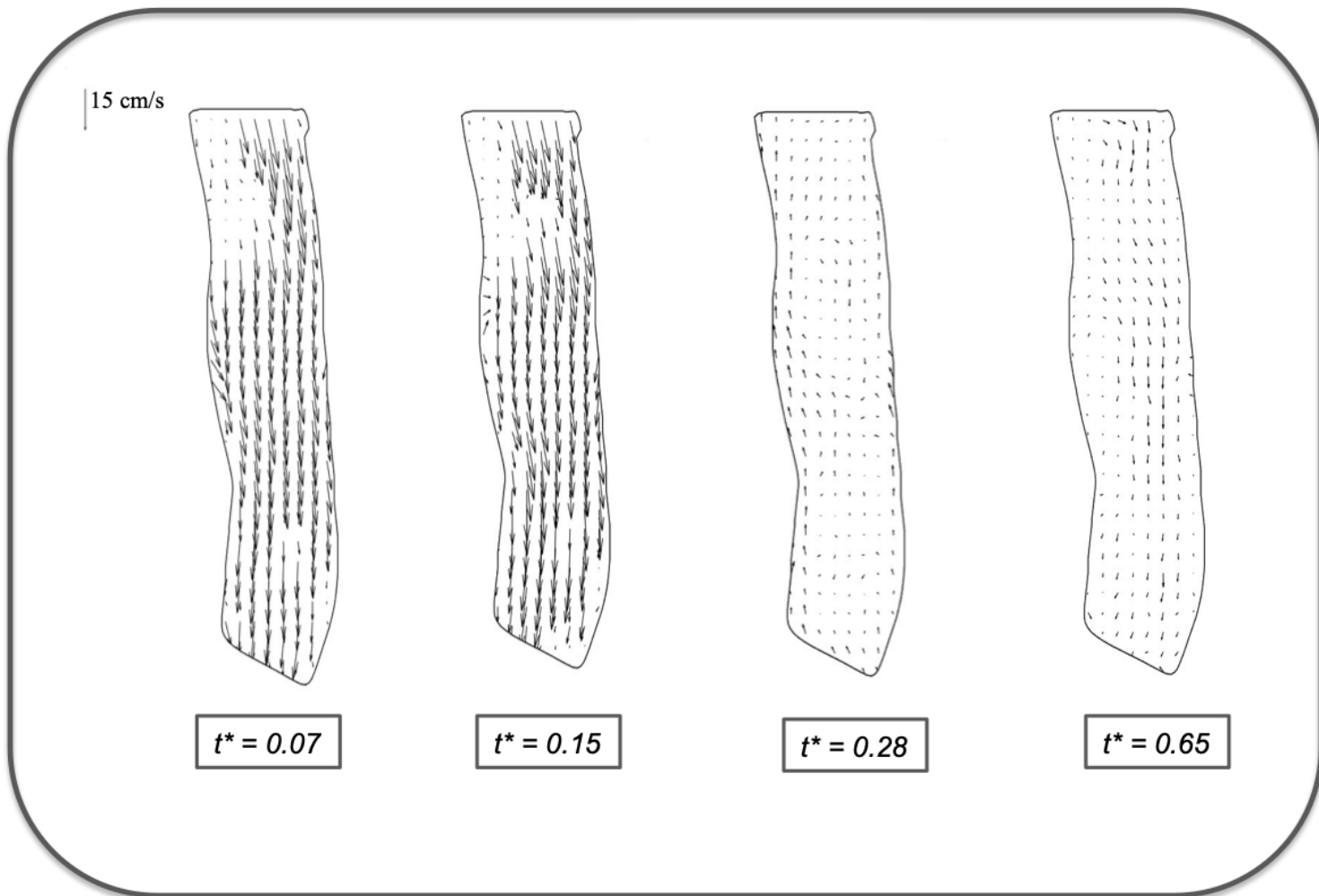


Figure 20: Velocity field snapshots, Healthy aorta plane B. With a velocity scale of 15 cm/s

4.1.1.2 Impact of increased heart rate, case of the healthy aorta

When the heart rate increases, from 60 bpm to 80 bpm, the forward flow velocity increases, however, the same general structures are observed at the same time instant. Notably the same backflow is observed and the same slow motion vortices in the center of the lumen are present. When the heart rate goes up to 100 bpm, the forward flow increases even more, at this point the vortices are compressed against the posterior wall becoming narrower. The higher heart rate used represents a tachycardia situation. In the normal aorta, increased heartbeat results in a few modifications in the flow structures. The velocity field at the time instant $t^* = 0.275$ in plane B is presented in [Figure 21](#).

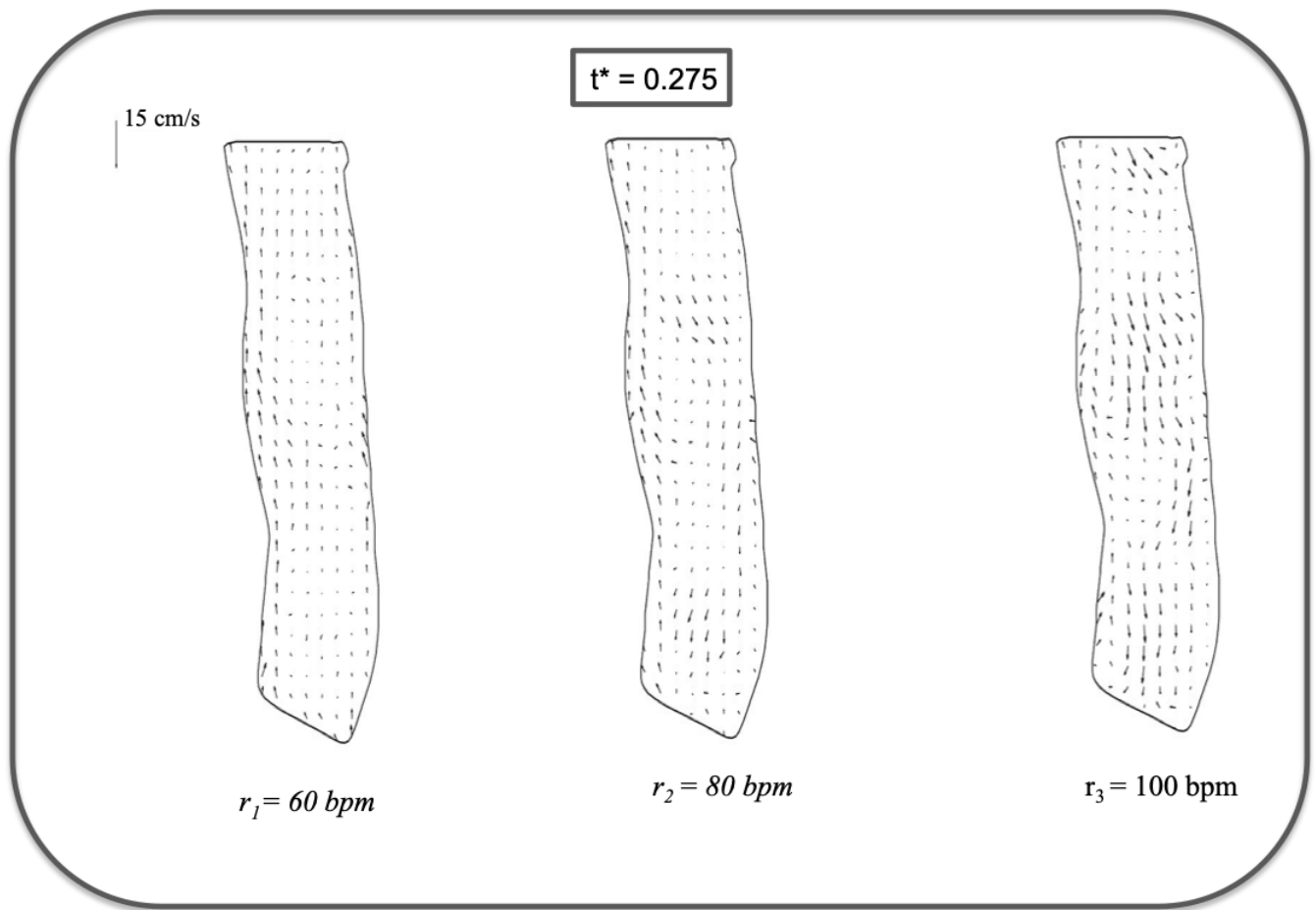


Figure 21: Velocity field at $t^* = 0.275$ comparison between the three different heart rates.

With a velocity scale of 15 cm/s

4.1.2 Saccular aneurysm model

In the saccular AAA model, 8 planes are studied. As stated above, this model represents a small aneurysm (compared to the fusiform aneurysm, see next section). The main flow structures are of comparable size to the aneurysm; therefore, strong interactions with the walls are expected. Those structures are visible in every plan, even if they only partially appear in the smallest planes. This aneurysm bulge reduces to a healthy size before the aortic arch. It is also important to note that, in this model, there is a reduction of the aorta diameter before the

aneurysm, with a diameter of roughly 16 mm at the entry of the aneurysm. [Figure 22](#) shows the different planes investigated in this model.

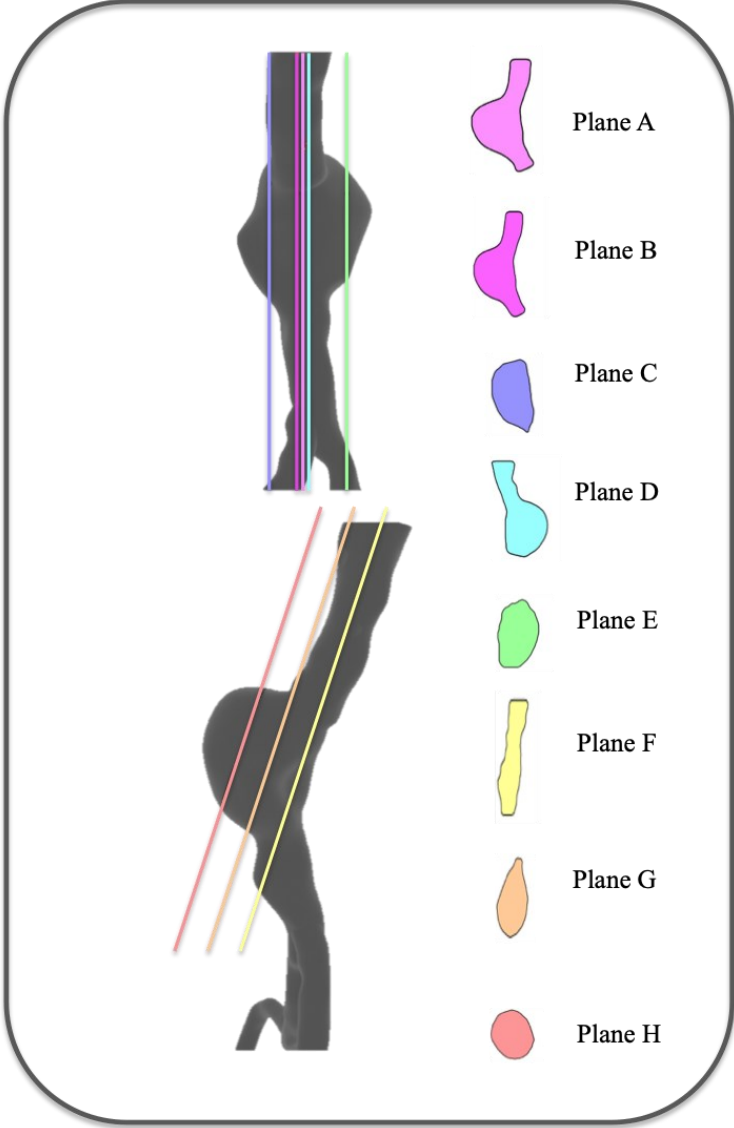


Figure 22: Planes investigated for the saccular aneurysm model.

4.1.2.1 Velocity fields at rest, Saccular aneurysm model

When observing the flow created in the saccular AAA model in resting conditions, we observed that, at the start of systole, two regions were identified: a nearly stagnant flow in the aneurysm bulge and a jet flow at the aneurysm neck. A vortex is generated shortly after the

systolic peak, in a more symmetrical aneurysm it would be expected that a vortex ring would form. It appeared that due to the saccular shape of this particular aneurysm, the interaction with the posterior wall prevented the formation of such a vortex ring. Here, we can describe this structure as ‘a squeezed vortex ring’. As the vortex propagates downwards the shape of the vessel after the aneurysm sac allows the development of the second half of the vortex ring at the beginning of the diastole. It rapidly crashes on the wall at the aortic bifurcation. After some deformations only the main side of the vortex ring subsists and creates a large recirculation area in the aneurysm bulge.

Contrarily to the healthy case, there is no backflow close to the posterior wall where the main jet structure exists, however, some backward flow exists. It primarily comes from the upward rotation of the flow in the aneurysm bulge. Some random fluctuation and small vortices appear, notably in the aortic neck, where the shear between forward and backward flow seems to be their main cause. Some velocity field snapshots are presented in [Figure 23](#) and [Figure 24](#) for the plane A and G.

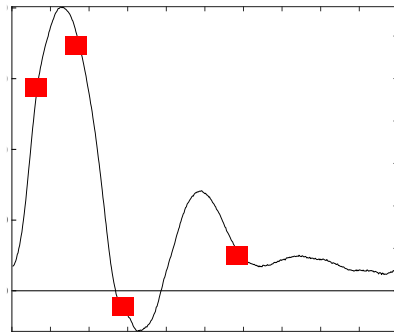
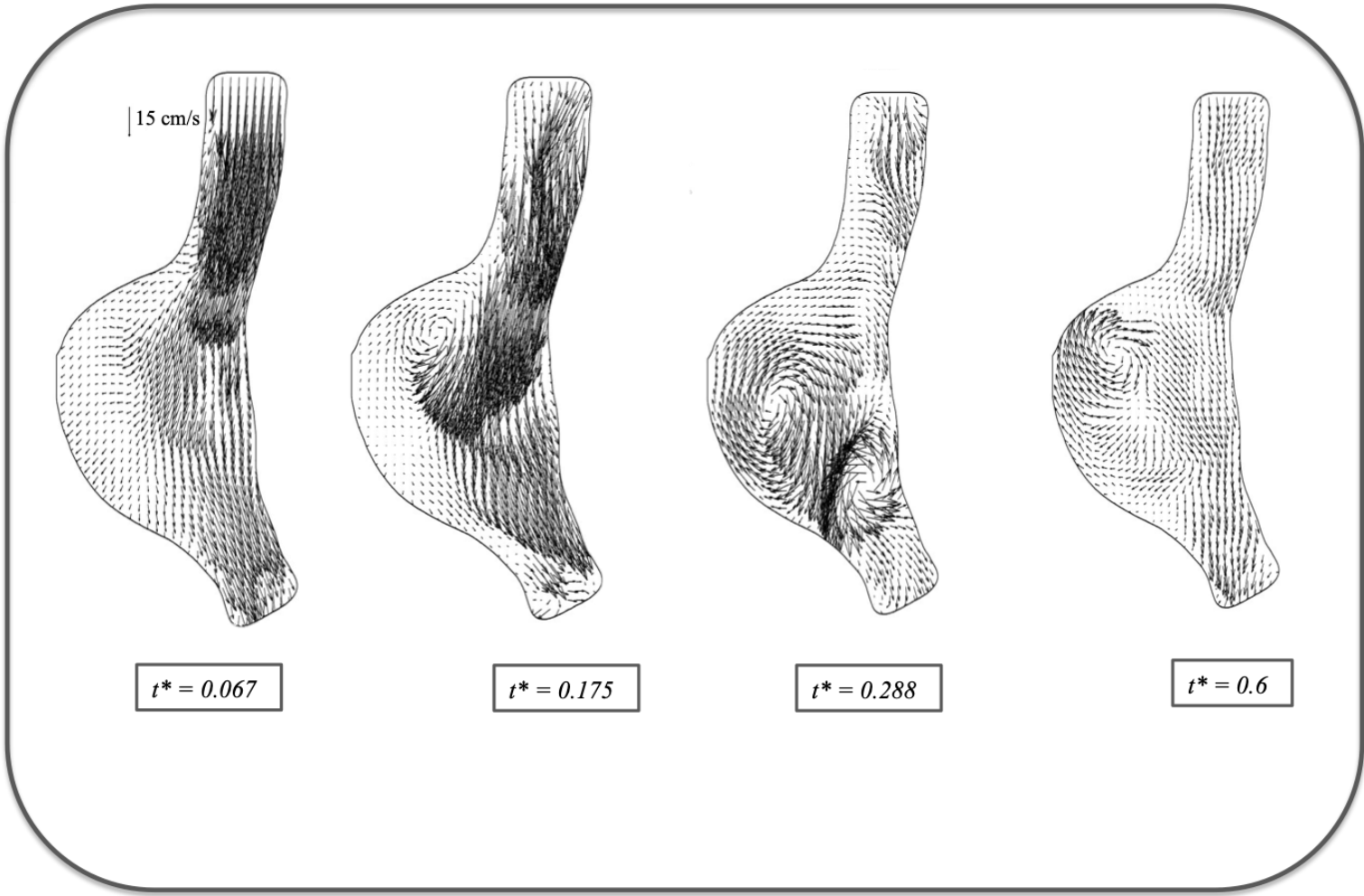


Figure 23: Velocity snapshot, saccular aneurysm plane A, the dimension-less times ($t^* = t/T_I$) are indicated in red on the flow waveform graph

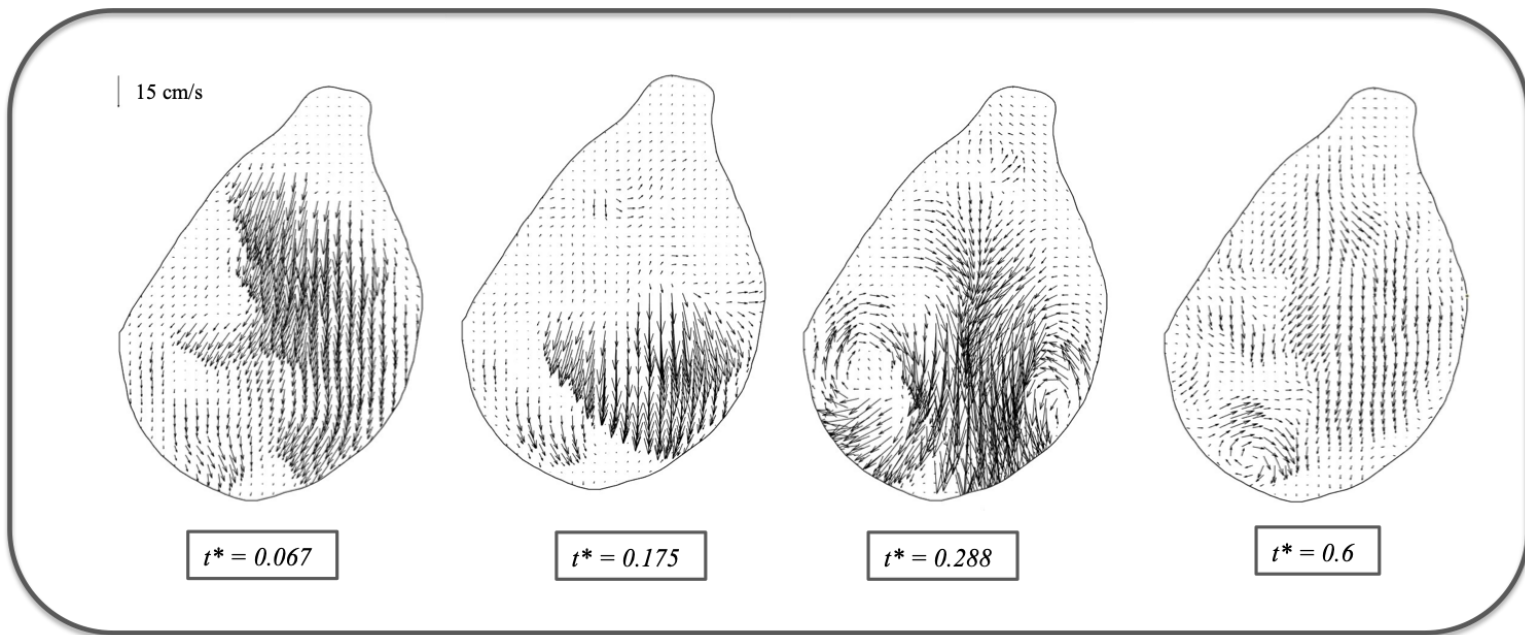


Figure 24 Velocity snapshot, saccular aneurysm plane G

4.1.2.2 Impact of increased heart rate on the flow in the saccular aneurysm

When increasing the heart rate to 80 bpm, the flow structures are mostly similar, although more instabilities are visible. The backward flow observed in resting conditions is no longer present. When the heart rate is further increased to 100 bpm, we observed a higher level of instability of the flow. It can also be noted that the vortex ring does not form right after the peak of systolic. The vortex ring does not appear in this case, but some vortices form in the aneurysm bulge. Some short bursts of backward flow from the unstable bulge flow are observed.

Therefore, we can see that increasing the heart rate has different effects on the flow when compared to a normal aorta. [Figure 25](#) shows a comparison of velocity fields at different heart rates.

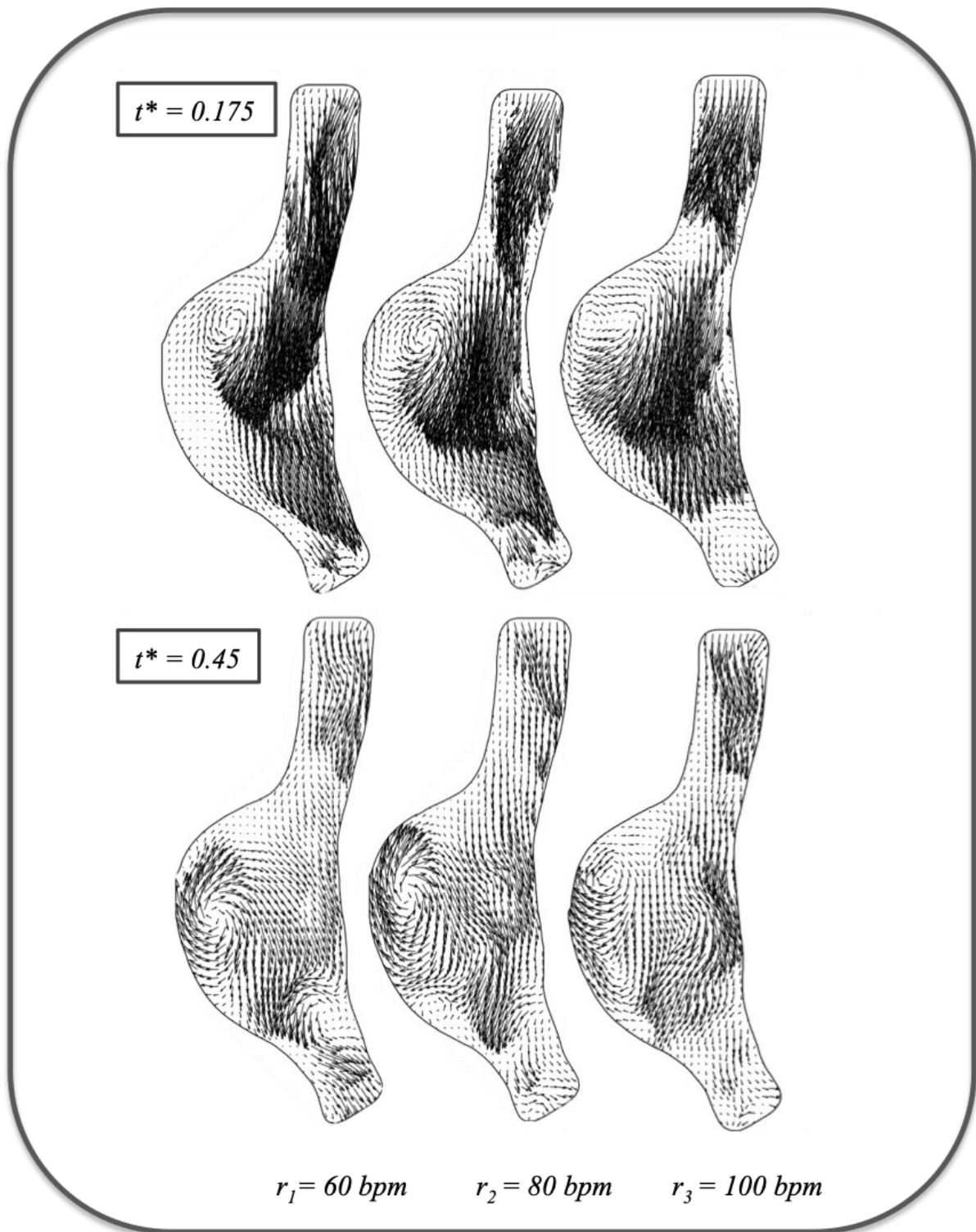


Figure 25: Velocity fields at $t^* = 0.175$ and $t^* = 0.45$, on plane A comparison for different heart rates.

4.1.3 Fusiform aneurysm model

The fusiform AAA model studied in this thesis can be considered a large aneurysm (with a characteristic size of around 70 mm). Some of the flow structures are smaller than the aneurysm bulge and do not appear in every plane. The arterial bifurcation is directly linked to the aneurysm, with a rapidly decreasing diameter from the 70 mm aneurysm to the iliac arteries. [Figure 26](#) shows the different planes of investigation for this model.

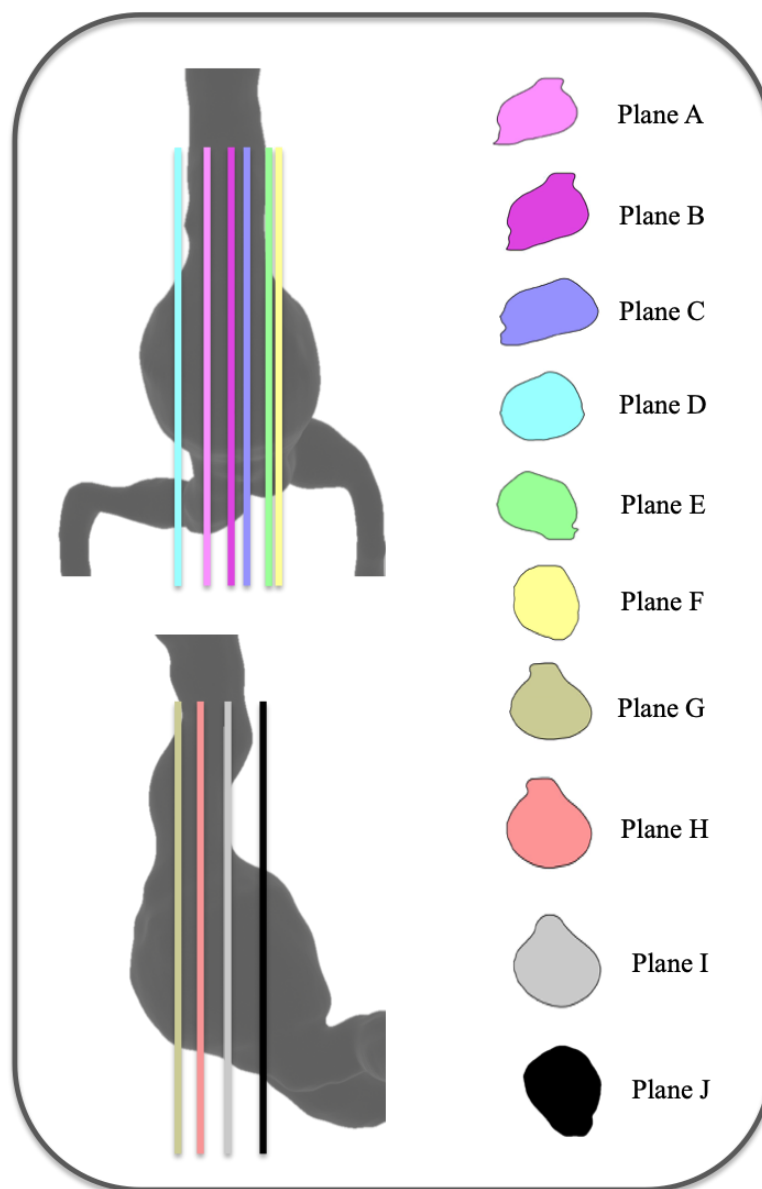


Figure 26: Planes of investigation for the fusiform AAA model

4.1.3.1 Velocity fields at rest

In the case of the fusiform aneurysm studied, for $r = r_l$, it is clear that the large size of the aneurysm has an impact on the flow, with fairly different patterns at different places of the aneurysm. The jet entering the aneurysm creates an unstable vortex ring, which sheds multiple smaller vortices. A large rotational motion is also observed in the aneurysm. It creates some backward flows. As stated, the jets entering the aneurysm do not create a clear vortex ring. Instead, they rapidly decay and generate smaller vortices. This unusual behavior could be caused by the nature of the jet entering the aneurysm bulge, as we can see from the patient-specific section of the aorta that bends shortly before the aneurysm neck. Another hypothesis is that the difference in size between the iliac arteries and the bulge of the aneurysm creates a pressure wave reflection that could impact the development of the vortex ring. [Figure 27](#) and [Figure 28](#) show some velocity snapshots at $T = T_l$ in Planes A and G of the fusiform AAA model.

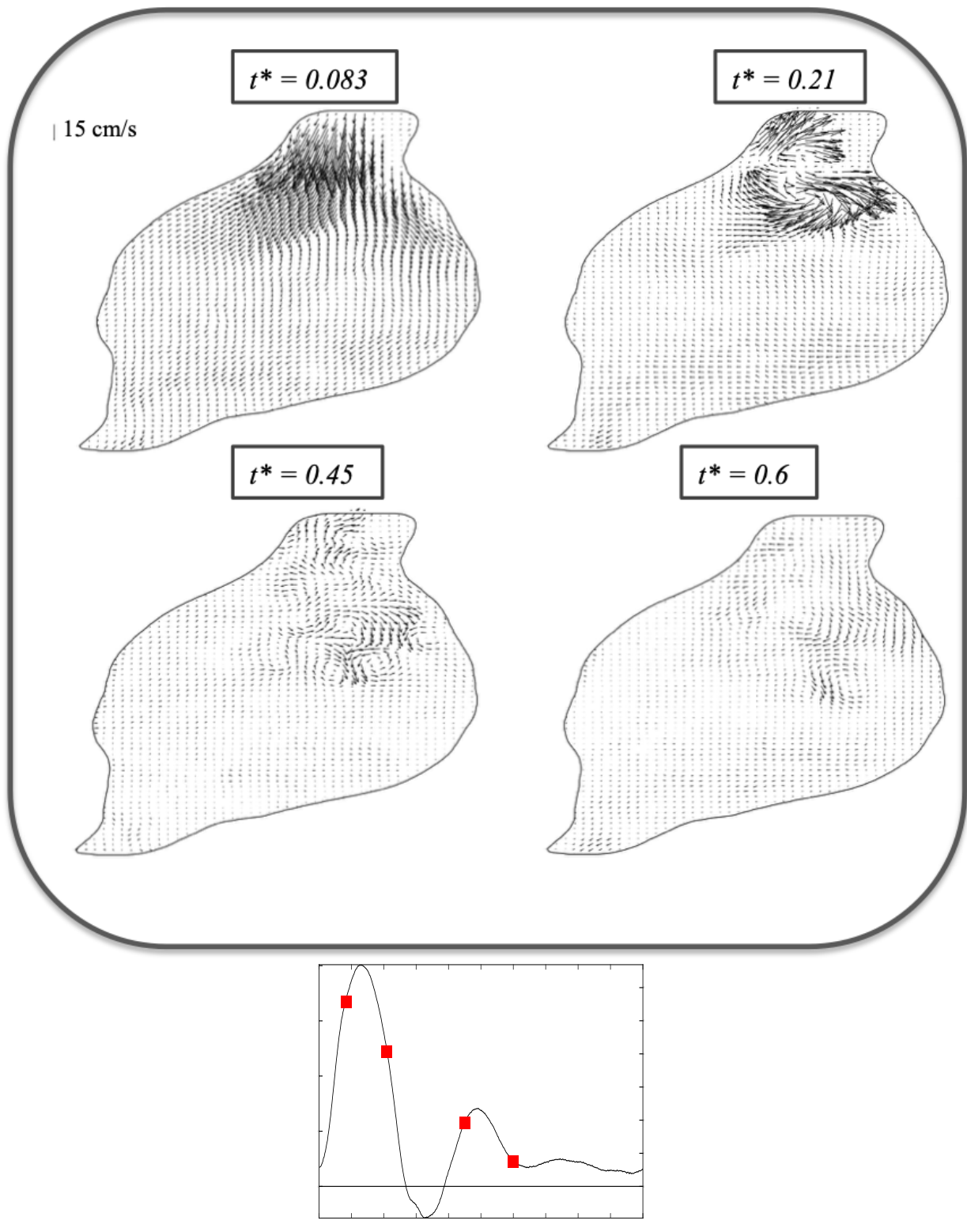


Figure 27: Velocity field snapshots, fusiform aneurysm plane A, the dimensionless times ($t^* = t/T_1$) are indicated in red on the flow waveform graph underneath

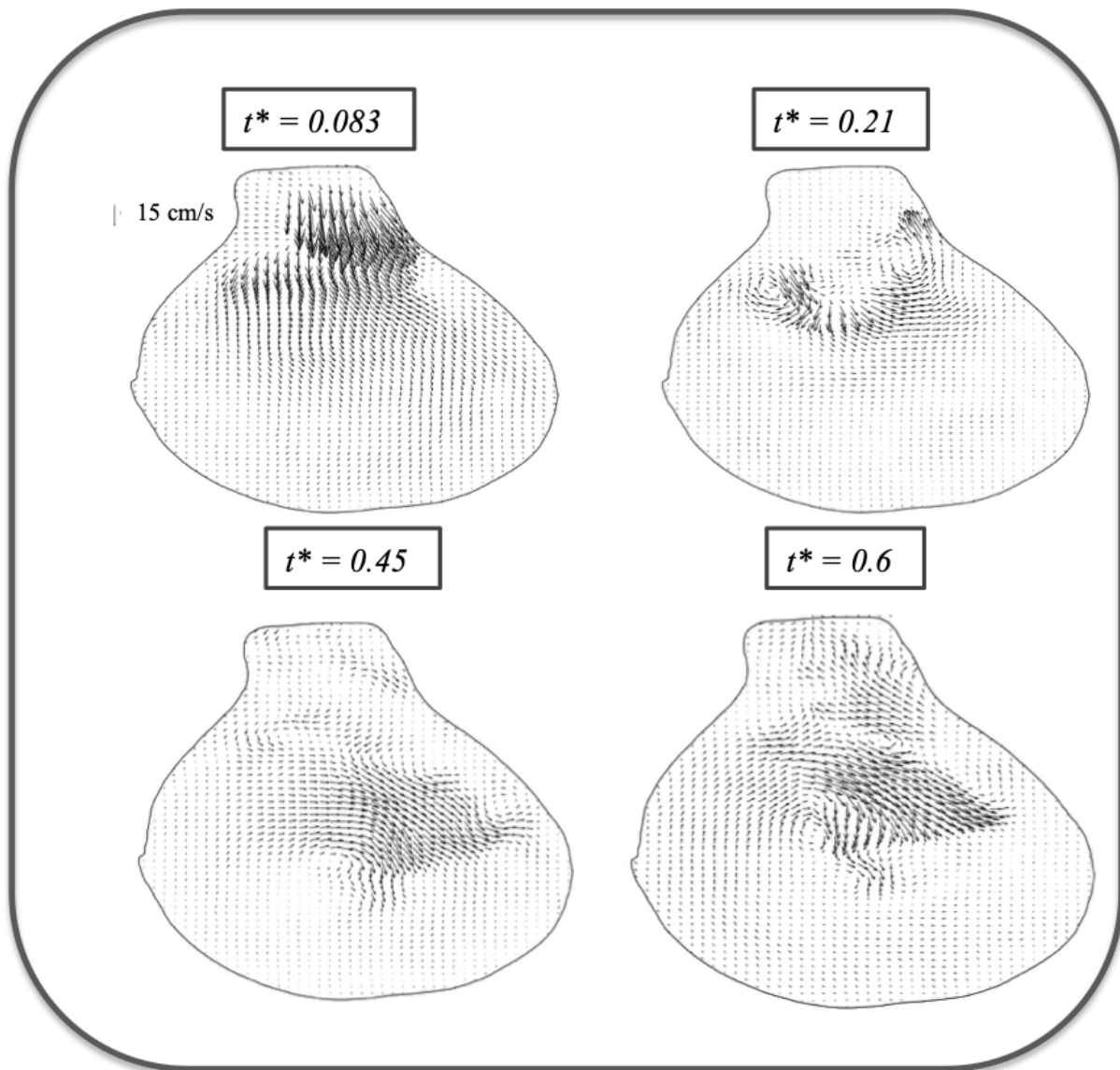
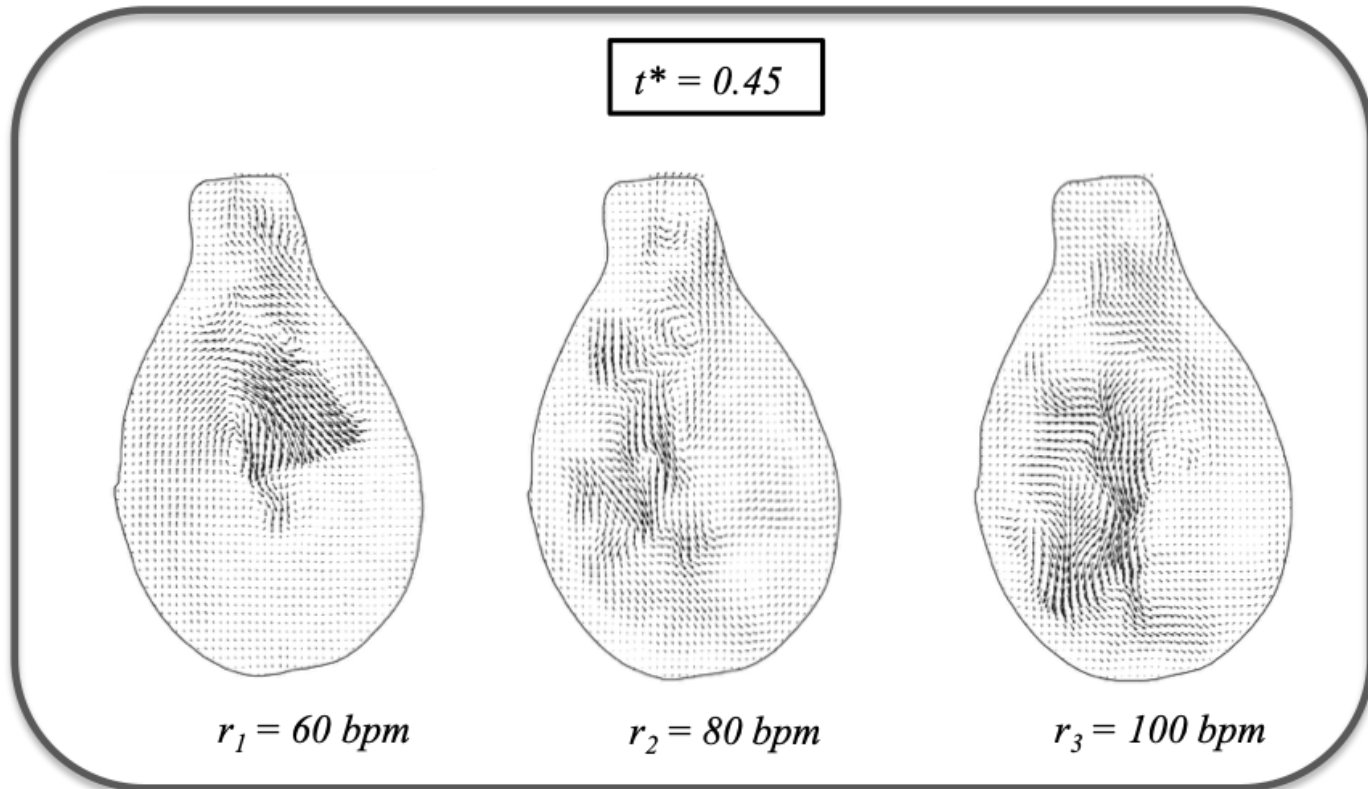


Figure 28: Velocity field snapshots, fusiform aneurysm plane G

4.1.3.2 Impact of increased in heart rate in the fusiform aneurysm

When increasing the heart rate at both $r_2 = 80$ bpm and $r_3 = 100$ bpm, we observed an acceleration of the large rotation motion in the aneurysm as well as an increase in random fluctuations. It also appears that the vortex structures created by the entering jet change the path when the heart rate changes. Some random changes in the path from beat to beat are to be expected. However, the changes of paths with the heart rate seem consistent between the different investigated planes. The latter reinforces the idea that this difference comes from the

changes in heart rates and is not a random change between two heartbeats. [Figure 29](#) presents the flow difference on the plane G for every heart rate at $t^* = 0.45$



[Figure 29](#): Velocity fields at $t^* = 0.45$, on plane G comparison for different heart rates.

4.2 Viscous energy loss

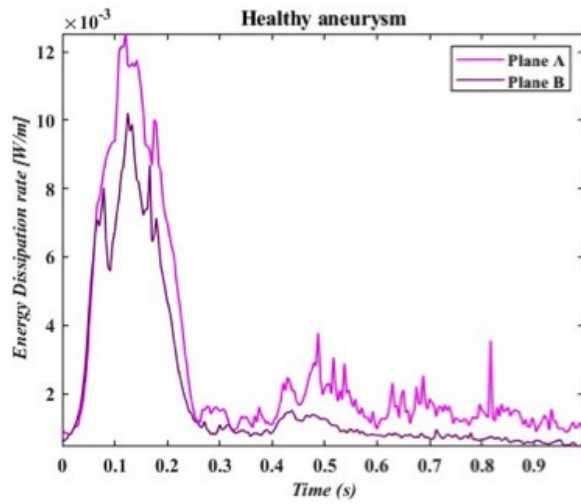
As discussed, investigating the growth of AAAs and the risk of rupture is a challenging task. Useful morphologic data like the maximal diameter is a marker used in the clinic to estimate the risk of rupture but is not precise enough. Other hemodynamic parameters like low WSS (Wall Shear Stress) and high OSI (Oscillatory Shear Index) have been recommended to assess the risk of rupture. Nevertheless, their correlation with the aneurysm growth is still debated. As stated in section 2.3, we investigated here the impact of an aneurysm on the viscous energy loss in the abdominal aorta, by way of the comparison of the Viscous energy dissipation rate (VEDr) or the rate at which the energy is dissipated. VEDr quantifies how fast

the kinetic energy is transformed into heat. [Figure 30](#), [Figure 31](#), and [Figure 32](#) present the VEDr by unit of depth for all the cases investigated in this study. The VEDr by unit depth is the result of the integration of the surface of the VEDr.

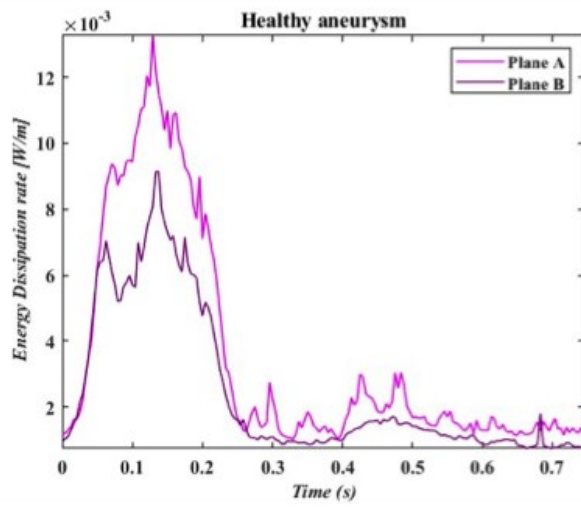
As expected, the VEDr is higher for all models during systole where the jet structure and vortices are created. During diastole, the VEDr is close to zero. If there is no notable increase in the VEDr systolic peak when the heart rate increases the shortening of the period creates an overall increase of the energy loss.

In both aneurysm models, flow structures like vortices create a higher VEDr compared to the healthy aorta. Overall, both aneurysm cases seem comparable in terms of VEDr.

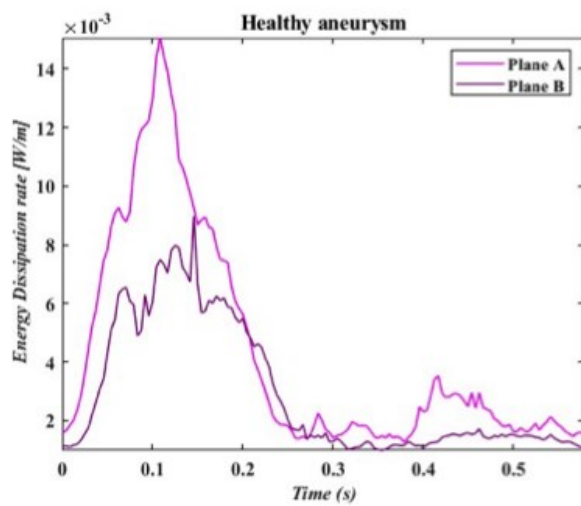
Lastly, the total energy loss on every plane during the heartbeat is computed by integrating over time the VEDr by unit of depth. [Figure 33](#) presents the total energy loss for all cases. On average, we can observe that the presence of an aneurysm increases the energy loss. The saccular model presents a higher energy loss than the fusiform model. This is likely due to the higher velocities present in this model with the reduction of the aneurysm neck diameter. It is also possible that, as the flow structures in the fusiform aneurysm occupy less space proportionally to the aneurysm size, the integration over the total area leads to an underestimation of the energy loss in the fusiform aneurysm.



$r_1 = 60 \text{ bpm}$

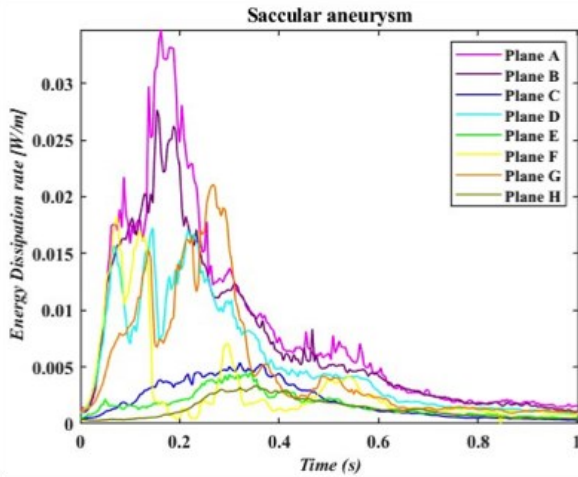


$r_2 = 80 \text{ bpm}$

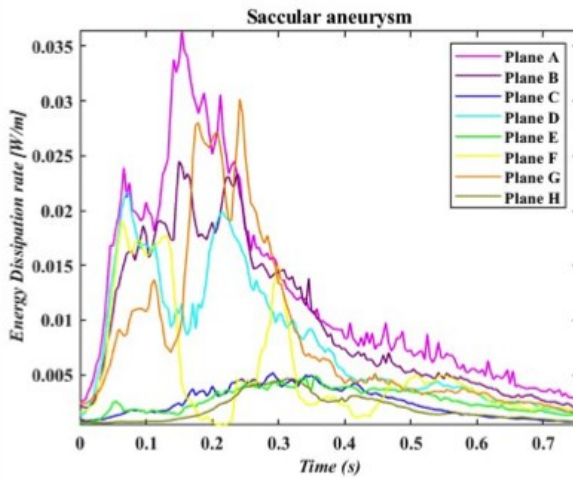


$r_3 = 100 \text{ bpm}$

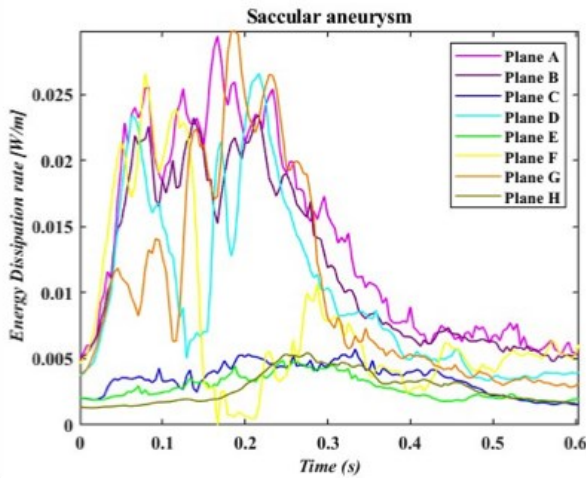
Figure 30: Energy dissipation rate by unit depth in the healthy aorta.



$$r_1 = 60 \text{ bpm}$$



$$r_2 = 80 \text{ bpm}$$



$$r_3 = 100 \text{ bpm}$$

Figure 31: Energy dissipation rate by unit of depth in the saccular AAA model.

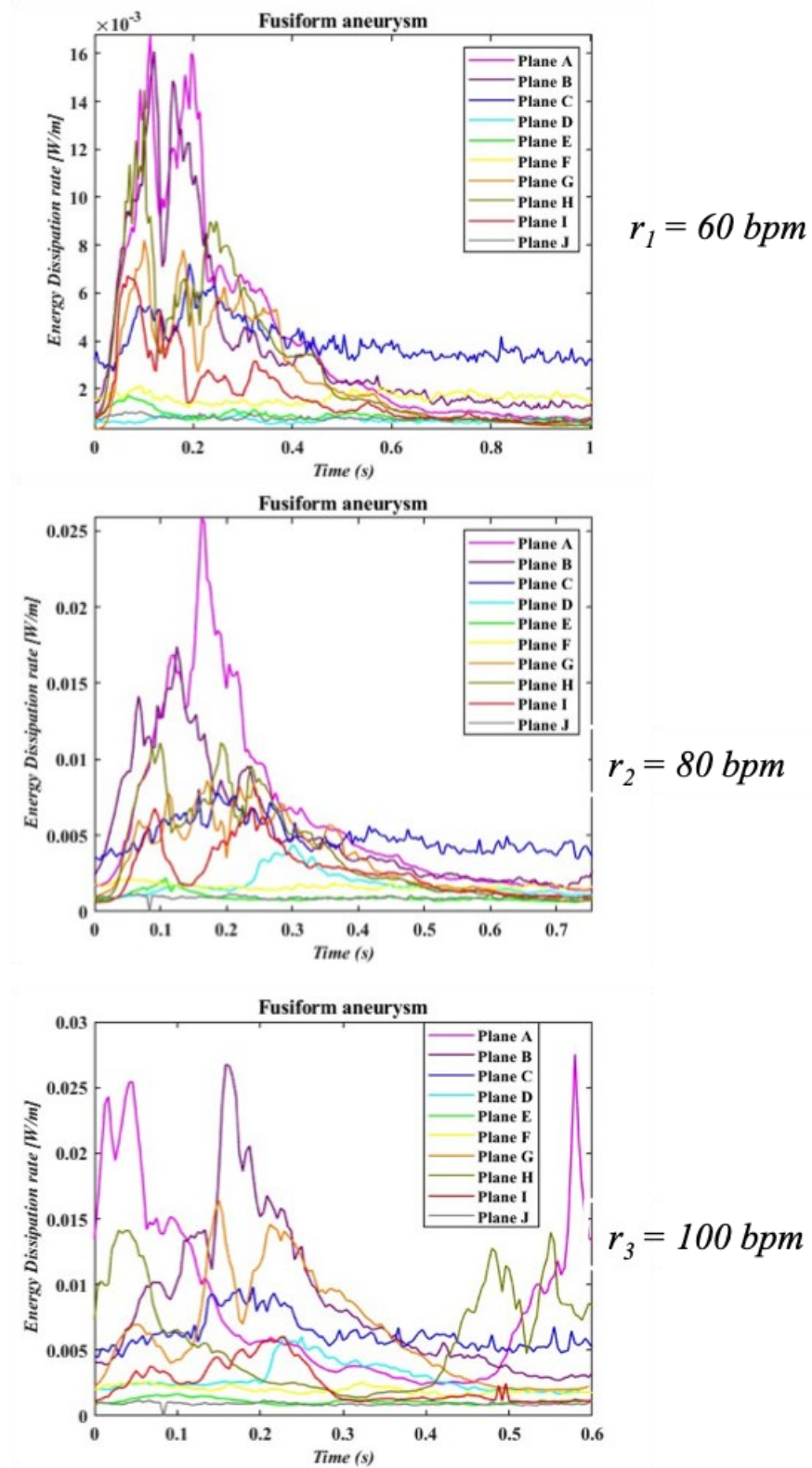


Figure 32: Energy dissipation rate by unit depth total fusiform AAA model

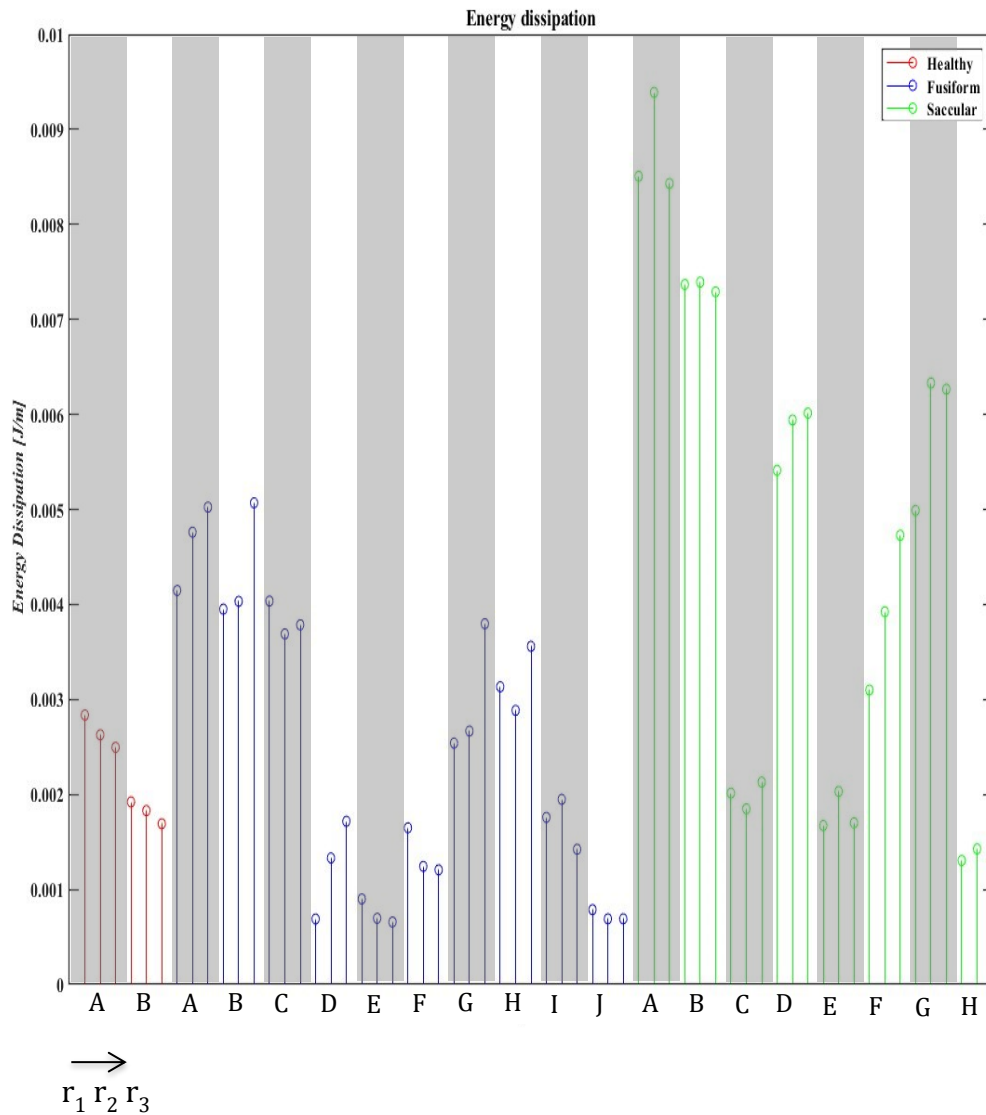
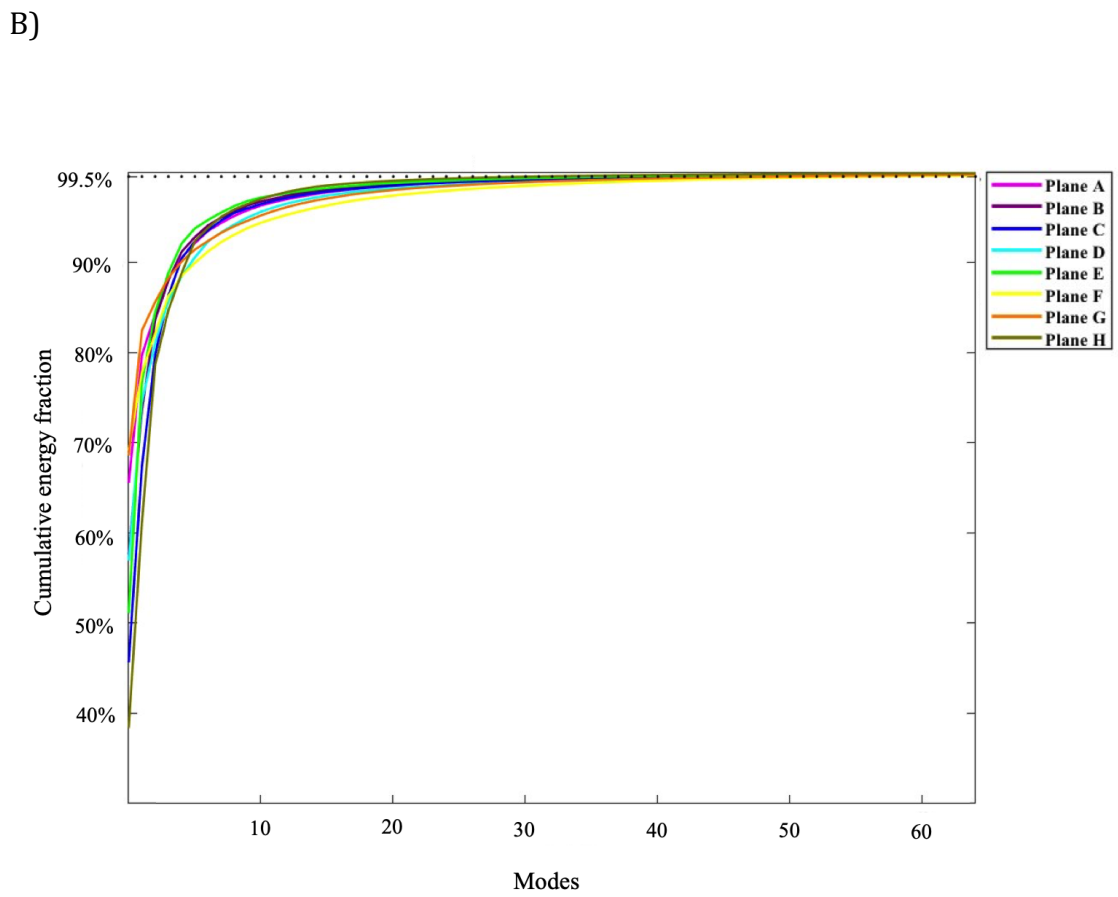
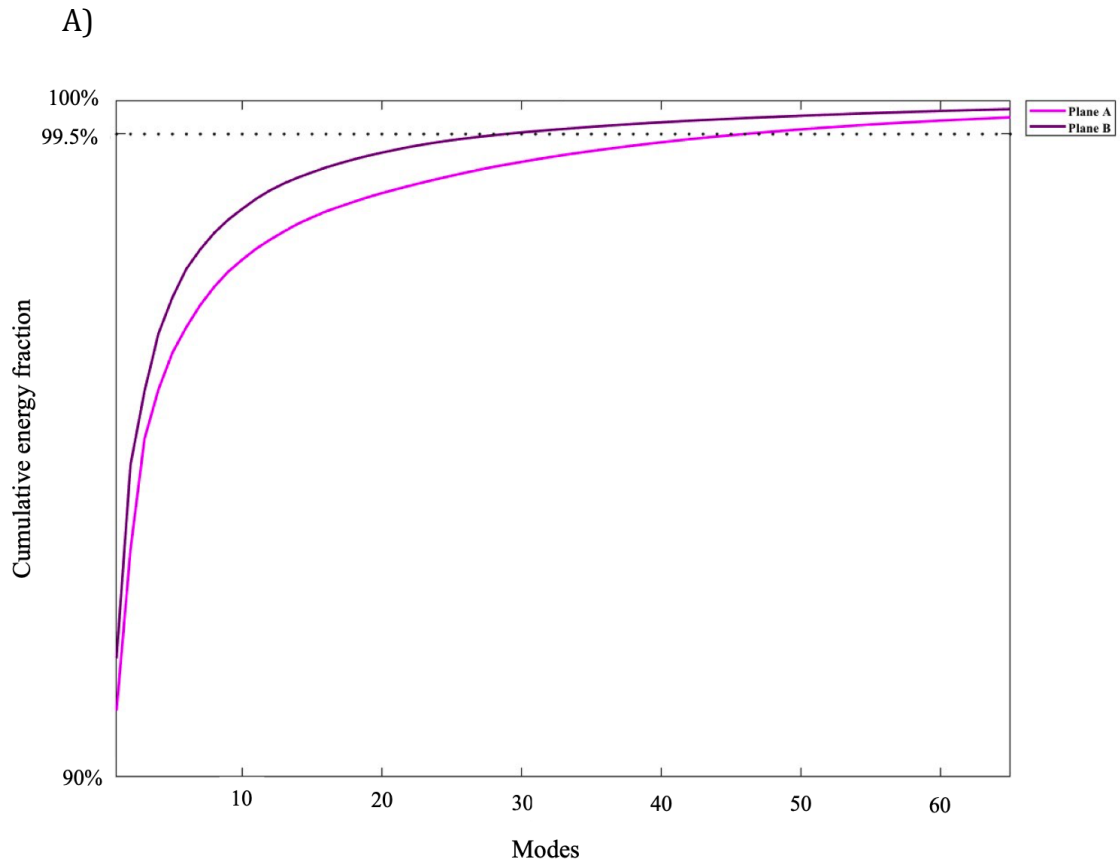


Figure 33: Total energy loss during a heartbeat, y-axis represents the total energy loss, x-axis represents all cases studied by plane clustered in groups of increasing heart rates.

4.3 Proper Orthogonal Decomposition

The description of flow structures as done in section 4.1 may enable the identification of structures in the flow. However, if the study of flow patterns is to be used as a diagnostic tool, a precise way of identifying coherent structures in the flow would be needed. POD is performed on all the cases in this study. The snapshot matrix size is therefore dependent on the heart rate used, 240 snapshots for r_1 , 180 snapshots for r_2 , and 140 snapshots for r_3 .

As stated, the modes obtained are stored in decreasing order with the amount of kinetic energy. The cumulative energy stored in the first 65 modes of every plane for each model in resting conditions is presented in [Figure 34](#). This can give a first understanding of the complexity of the flow, in terms of the number of modes required to compute a given value of the kinetic energy. We can see that the distribution of the energy in the saccular model is more similar from plane to plane than in the fusiform case, which reinforces the observation made that the flow structures created are partially visible in all planes, due to the size similarity between those structures and the aneurysm bulge. This is not the case in the bigger aneurysm corresponding to the fusiform model. The energy contents of the first mode in the healthy case, are respectively 92.4% for plane A and 93.8% for plane B. The simple flow of the healthy case results in the confinements of energy in the first mode, while the cases with aneurysms have a slightly wider distribution.



C)

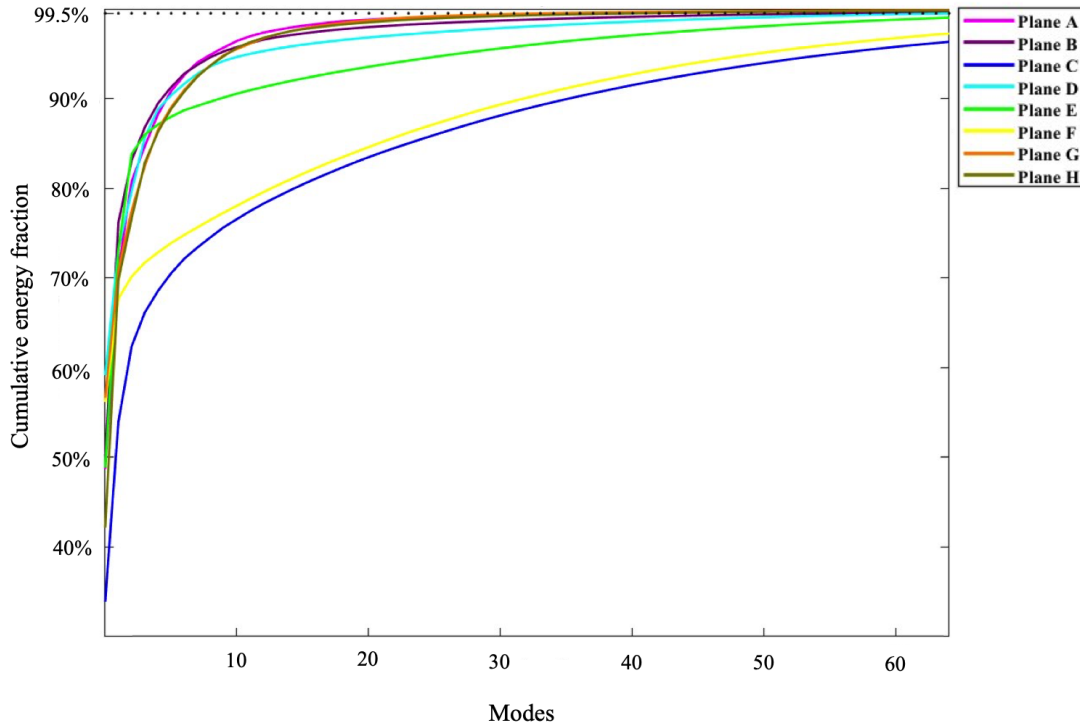


Figure 34: Energy contained in the 65 first modes, for $r = r_l$, A) healthy model, B) saccular model, C) fusiform model.

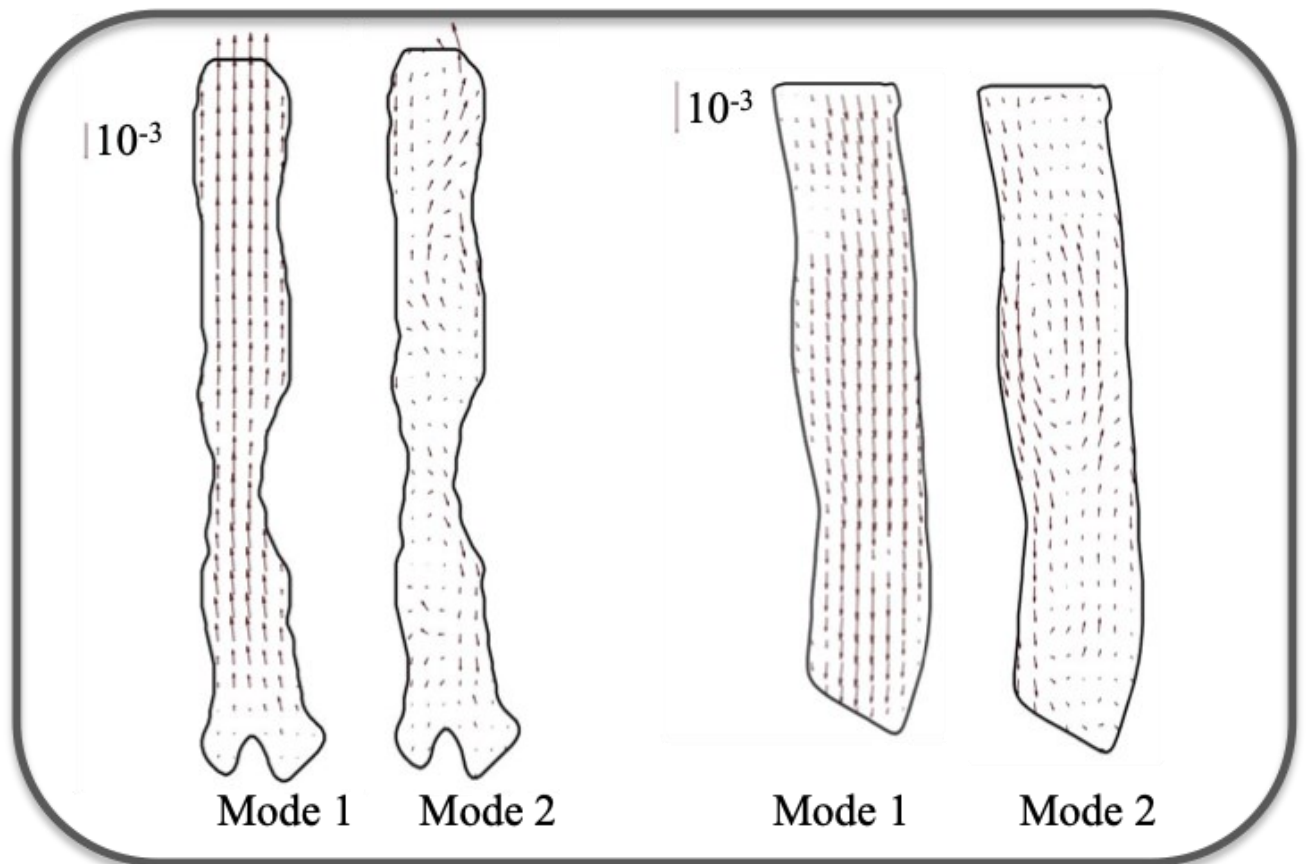
4.3.1 Mode description

As presented in section 3.3.5, the POD algorithm is performed without removing the time-averaged flow. Therefore, the first POD mode is similar to the time-averaged flow field. It is important to note that the first POD modes can also resemble the inverse of the time-average velocity field; in those cases the time coefficient of the POD mode is negative. This means that in the linear combination of modes that compose the flow the first POD mode will always behave as the time-average velocity field.

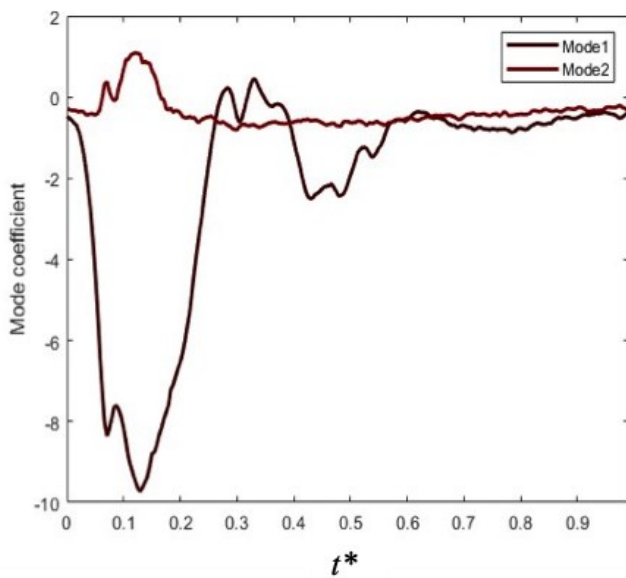
4.3.2 Healthy model

As stated, the healthy model has the simplest flow. In both planes, the first mode includes more than 90% of the overall kinetic energy; it acts as the mean flow corresponding to the forward motion of the blood needed by the vascular system to propagate in the body. Temporally speaking it follows the imposed flow. The second mode accounts for small perturbations in the flow and the backward flow. The two first modes for $r = r_l$ and their time coefficients are presented in [Figure 35](#).

A)



B)



C)

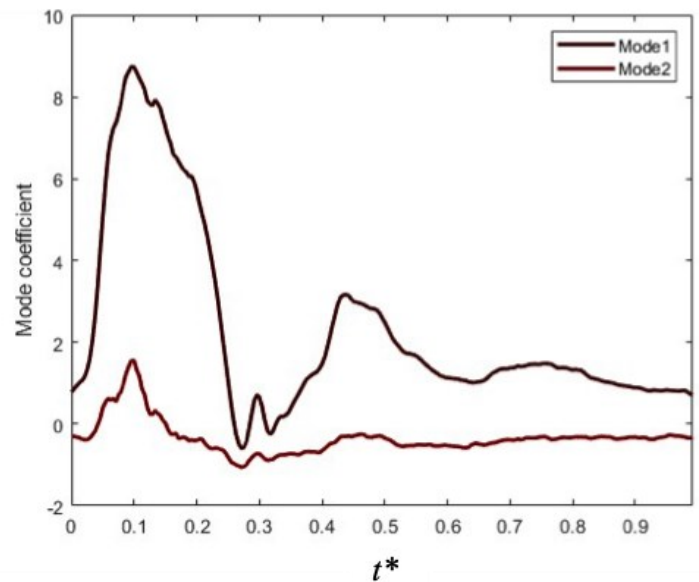
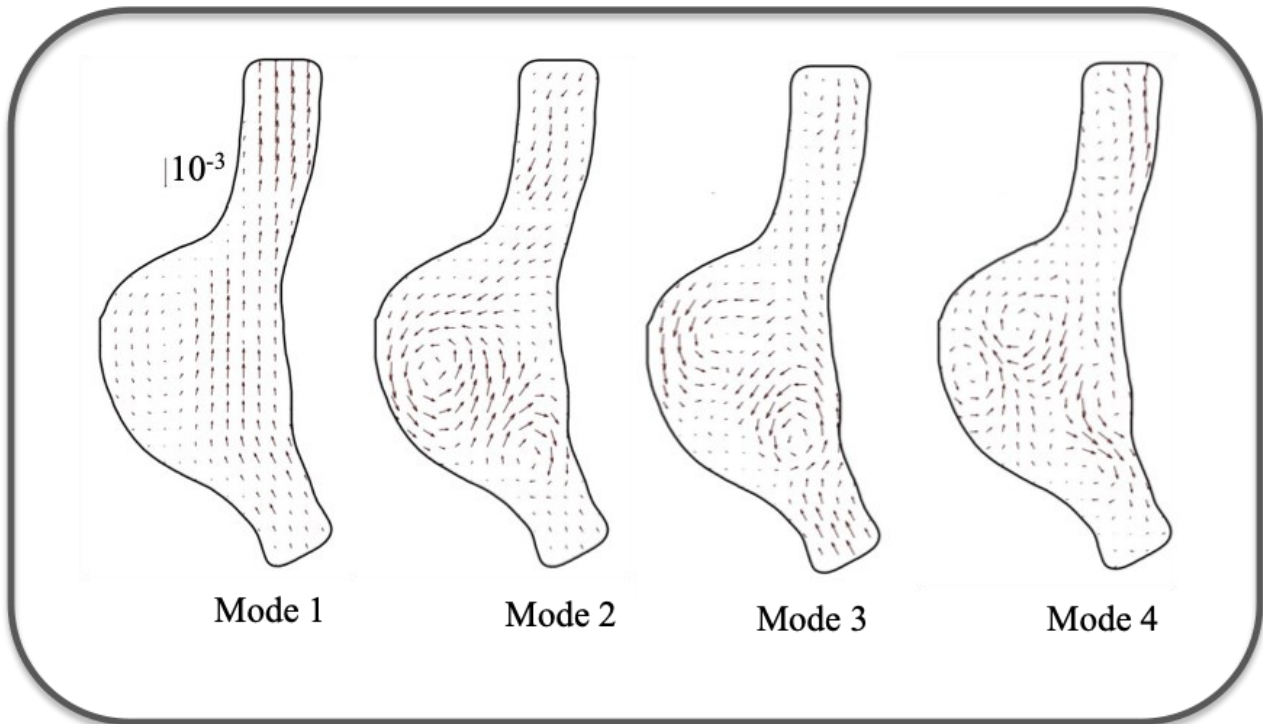


Figure 35: First two POD modes for planes A and B in the healthy aortic model, A) POD modes, B) time coefficients of the modes in plane A, C) time coefficients of the modes in plane B.

4.3.3 Saccular aneurysm model

In the saccular AAA model, the first mode also represents the forward blood flow. We can identify a slow-moving vortex filling the aneurysm bulge. The second mode captures the vortex ring at the end of the aneurysm; it shows the location of the vortex ring where its kinetic energy is maximal. Modes 3 and 4 compute a series of smaller vortices that contribute to the complexity of the flow. They were not easily identifiable by studying the velocity field of the flow. [Figure 36](#) presents the four first modes on plane A at $r = r_l$. The same general observations can be made on the plane G in [Figure 37](#).

A)



B)

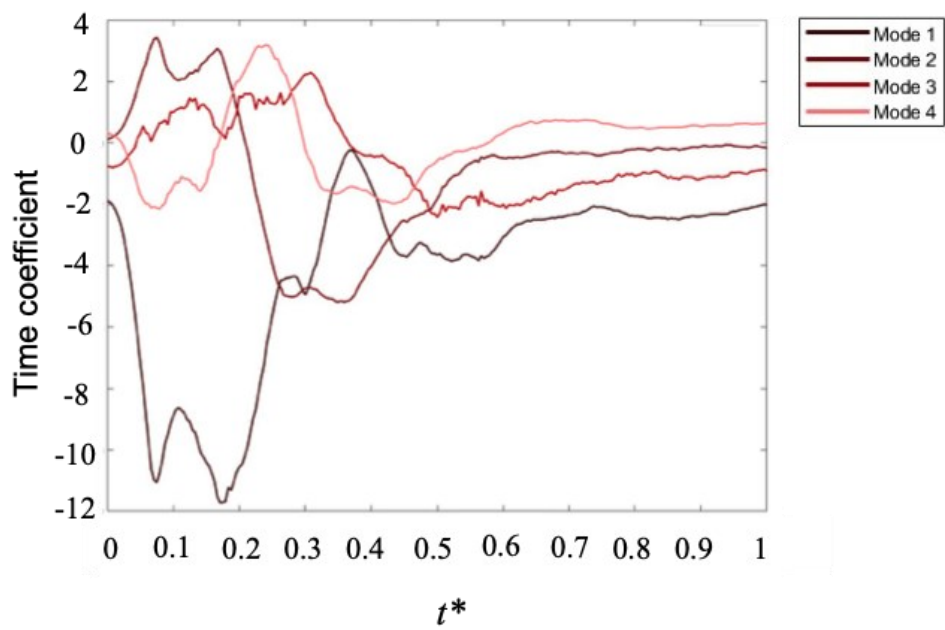
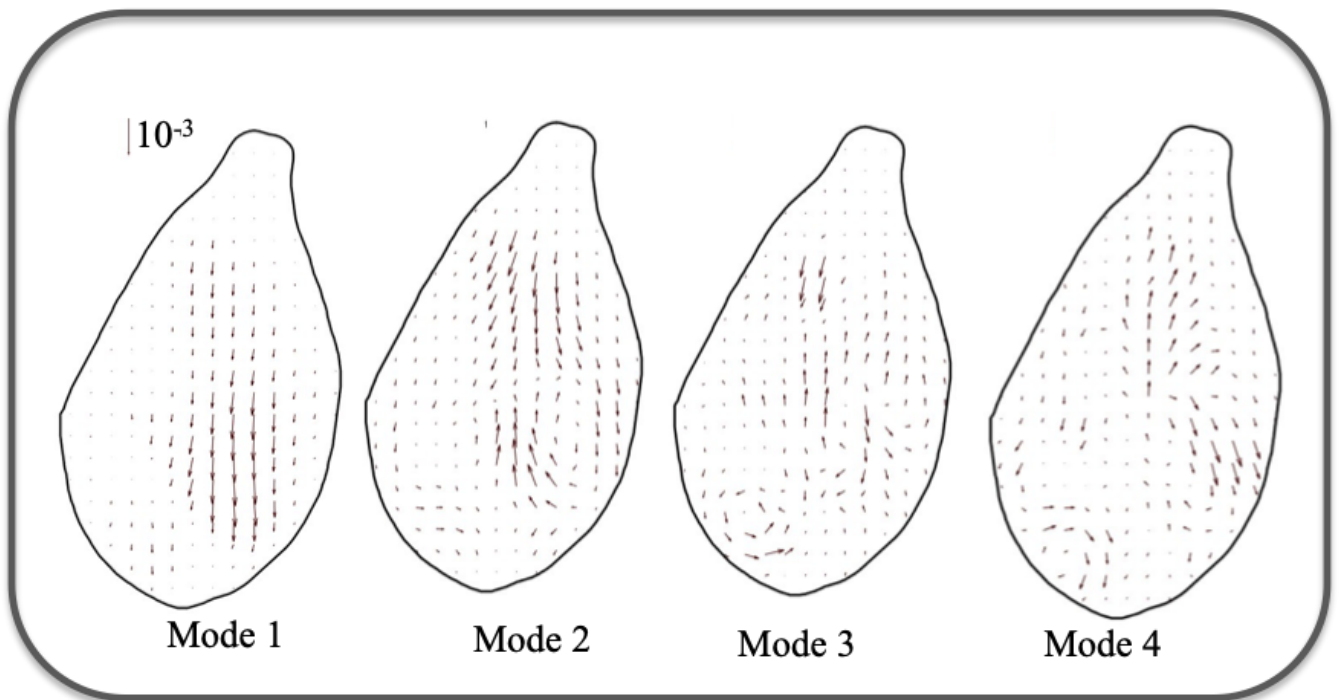


Figure 36: First four POD modes for plane A in the saccular AAA model, A) POD modes, B) time coefficients of the modes.

A)



B)

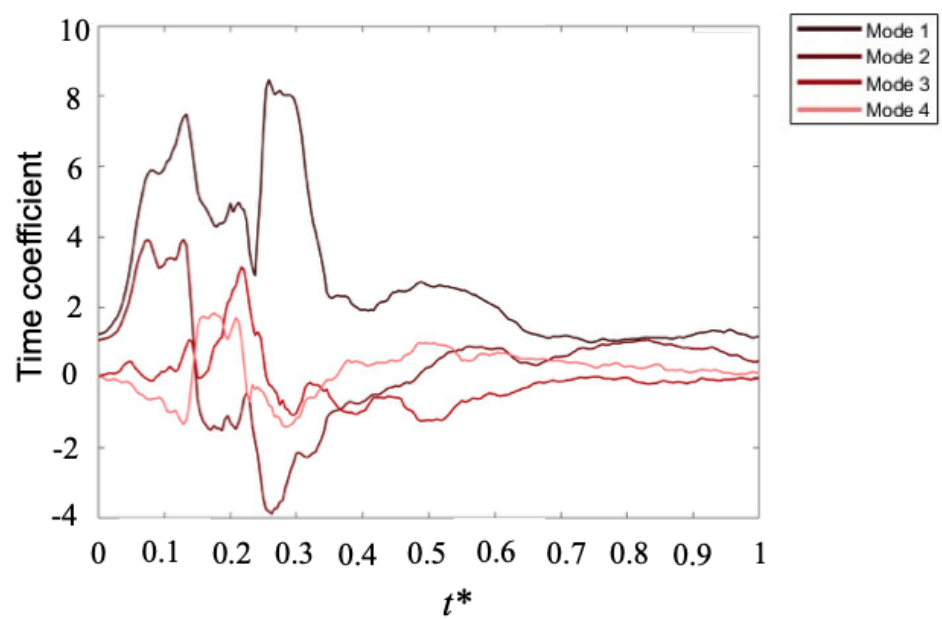


Figure 37: First four POD modes for plane G in the saccular AAA model, A) POD modes, B) time coefficients of the modes.

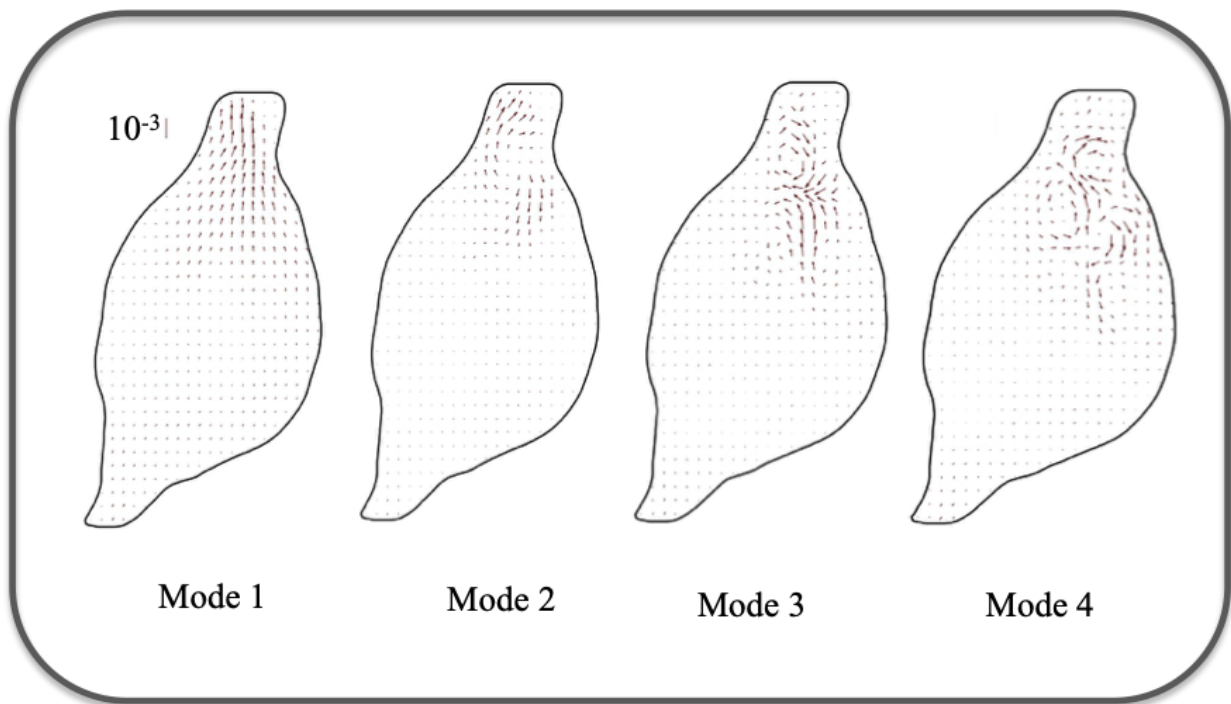
4.3.4 Fusiform Model

Similar observations can be made for the fusiform model. The first mode representing the time-average flow is still a forward flow. We see that most of the kinetic energy creates structures at the neck of the aneurysm on plane A [Figure 38](#).

In the plane G, we can see again that the planes 4 and 3 include small vortices. However, we can identify from the second mode, the large rotating structure present in the aneurysm in the second mode. [Figure 39](#) presents the four first modes at plane G.

Lastly, an interesting pattern is revealed by the time coefficient of the first mode. It shows clearly a systolic peak, however, some mechanical oscillation is present in the flow.

A)



B)

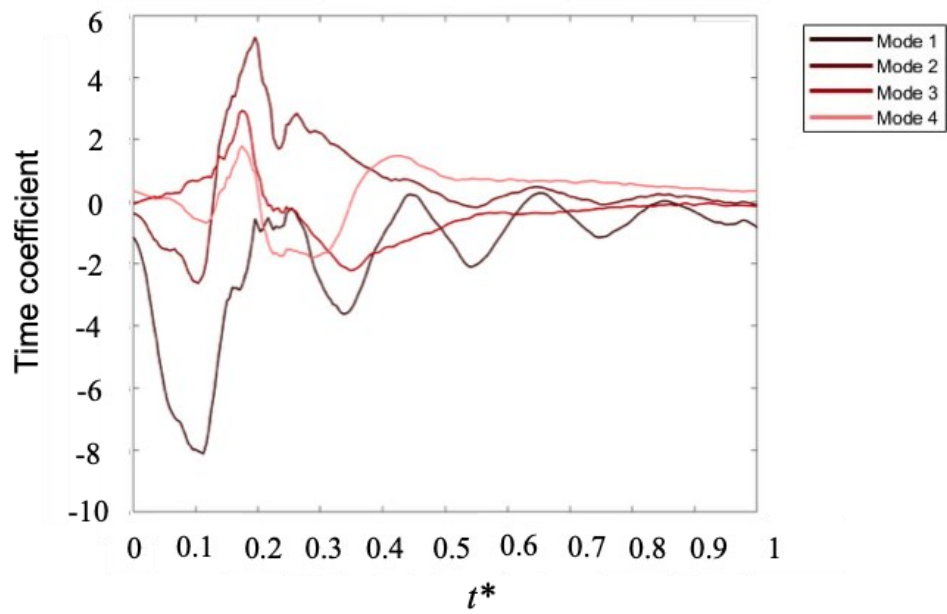
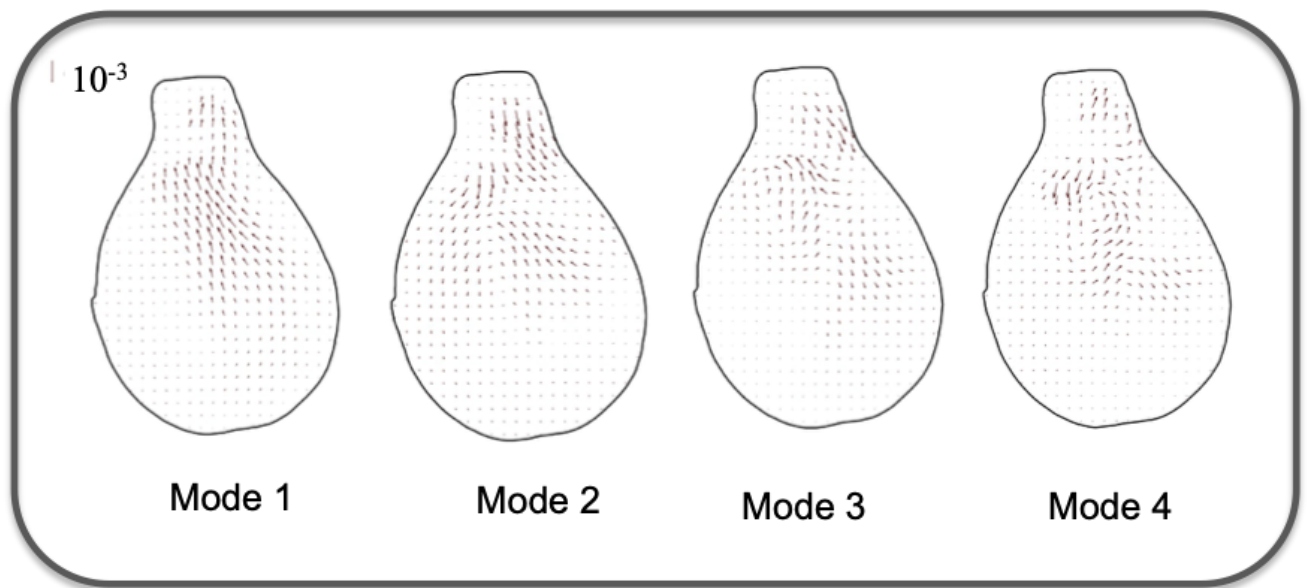


Figure 38: First four POD modes for plane A in the fusiform AAA model, A) POD modes, B) time coefficients of the modes.

A)



B)

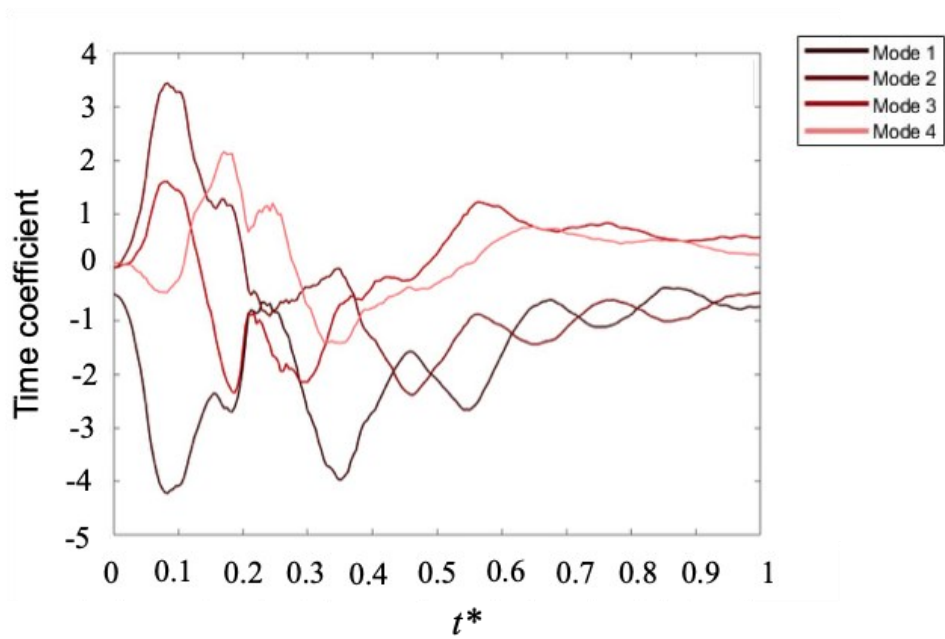


Figure 39: First four POD modes for plane G in the fusiform AAA model, A) POD modes, B) time coefficients of the modes.

4.3.5 Data reduction with POD

Instead of using a large number of grid points to represent the flow field, POD can be used to reconstruct the variables of interest from an optimal set of modes. The number of modes used will compute a total of cumulative energy; it must be chosen to reduce the relative error.

The reconstruction is done by projecting the POD modes onto the snapshot basis using the matrix of POD mode weights as a transformation matrix with the temporal dynamics in the rows and the essential coefficient for the reconstruction as columns. ([Di Labbio and Kadem 2019](#)). The required number of modes required to capture a specified energy level is shown in the following table.

Healthy				
$r_1 = 60$ bpm				
	88%	90,5%	99,0%	99,9%
Plane A	1	1	37	74
Plane B	1	1	48	103
$r_2 = 80$ bpm				
Plane A	1	1	37	74
Plane B	1	1	30	74
$r_3 = 100$ bpm				
Plane A	2	2	37	74
Plan B	1	1	23	56

Saccular				
$r_1 = 60$ bpm				
	88%	90,5%	99,0%	99,9%
Plane A	5	6	37	77
Plane G	6	7	37	70
$r_2 = 80$ bpm				
Plane A	5	6	37	77
Plane G	6	7	37	70
$r_3 = 100$ bpm				
Plane A	5	6	37	77
Plane G	6	7	37	70

Fusiform				
$r_1 = 60$ bpm				
	88%	90,5%	99,0%	99,9%
Plane A	5	6	35	70
Plan G	7	8	31	61
$r_2 = 80$ bpm				
Plane A	5	6	35	70
Plane G	7	8	31	61
$r_3 = 100$ bpm				
Plane A	5	6	35	70
Plane G	7	8	31	61

Table 2: Number of modes needed to capture a given kinetic energy fraction.

A model using enough modes to reach 98% of the overall kinetic energy is created, it strongly resembles the initial flow. The flow is smoother and it is expected that the vorticity will be lower than in the original flow as a part of the kinetic energy has not been reconstructed. This part will likely be linked to the small-scale vortices [Figure 40](#) shows a snapshot of the flow obtained with the reduced order model, in plane A of the fusiform model.

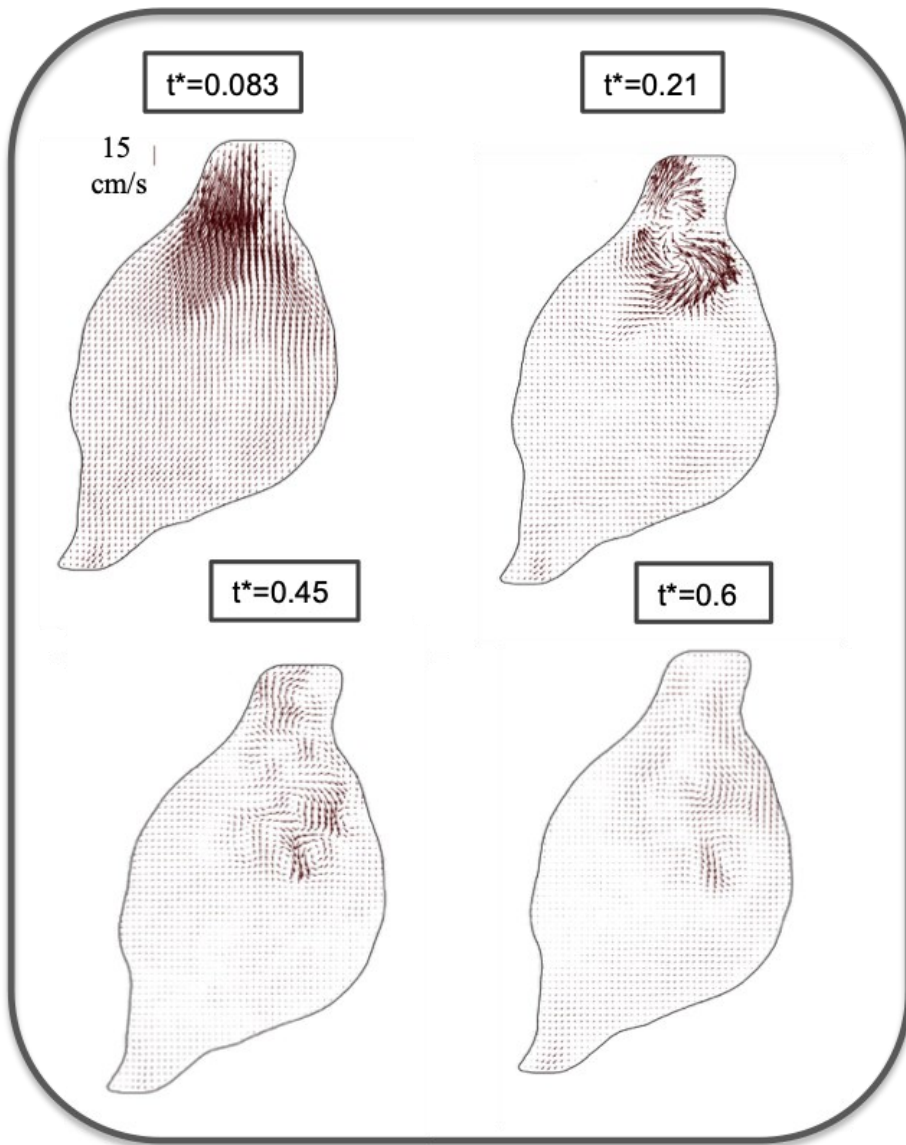


Figure 40: Velocity field snapshots, reduced order model capturing 98% of the overall kinetic energy, fusiform model plane A $r = r_l$

4.3.6 Viscous energy of the reconstructed model

In order to validate the reduced order model obtained with POD, we calculated the error between the viscous energy loss during one beat calculated based on the PIV results and based on the reduced order model. This is shown in [Figure 41](#). The computation of high-level parameters like the viscous energy loss requires that the model captures up to 99% of the kinetic energy, to obtain errors that are less than 10%.

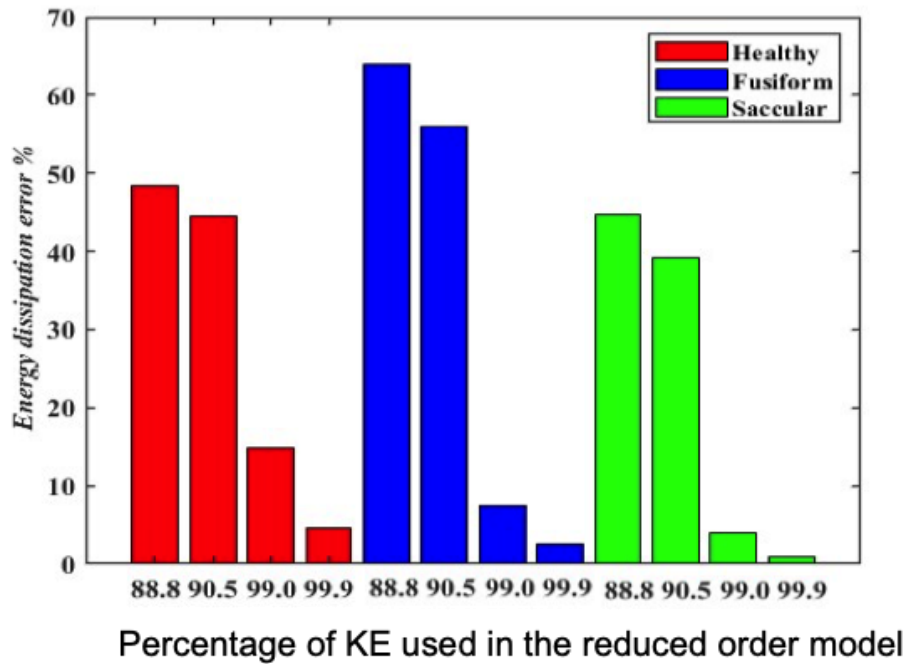


Figure 41: Difference in kinetic energy loss between the PIV data and the reduced order model

4.3.7 Shannon entropy

As stated in section 3.3.5, the Shannon or global entropy of the POD represents the distribution of energy between the different modes. It quantifies the complexity of the flow and clearly separates the three models. We averaged the Shannon entropy for all cases (planes and heart rates) for each model. This results in an average of 0.11 for the healthy case, which we had identified as leading to the simplest flow configuration, 0.29 for the saccular aneurysm, and 0.37 for the fusiform aneurysm. The Shannon entropy seems to be a robust parameter in terms of plane position, with a close value for every plane in the saccular and healthy cases.

We tested the robustness of this parameter to the reduction of the spatial resolution of the initial velocity field. By downsampling our results, we reach a resolution of $2.3 \times 2.3 \text{ mm}^2$ (close to what is usually available with clinical MRI). Results were similar between the results at PIV and MRI-like resolutions. This is encouraging since it shows that Shannon

Entropy could be used as a metric to characterize the flow dynamics in clinical settings.

Figure 42 represents the Shannon entropy for every model and every heart rate.

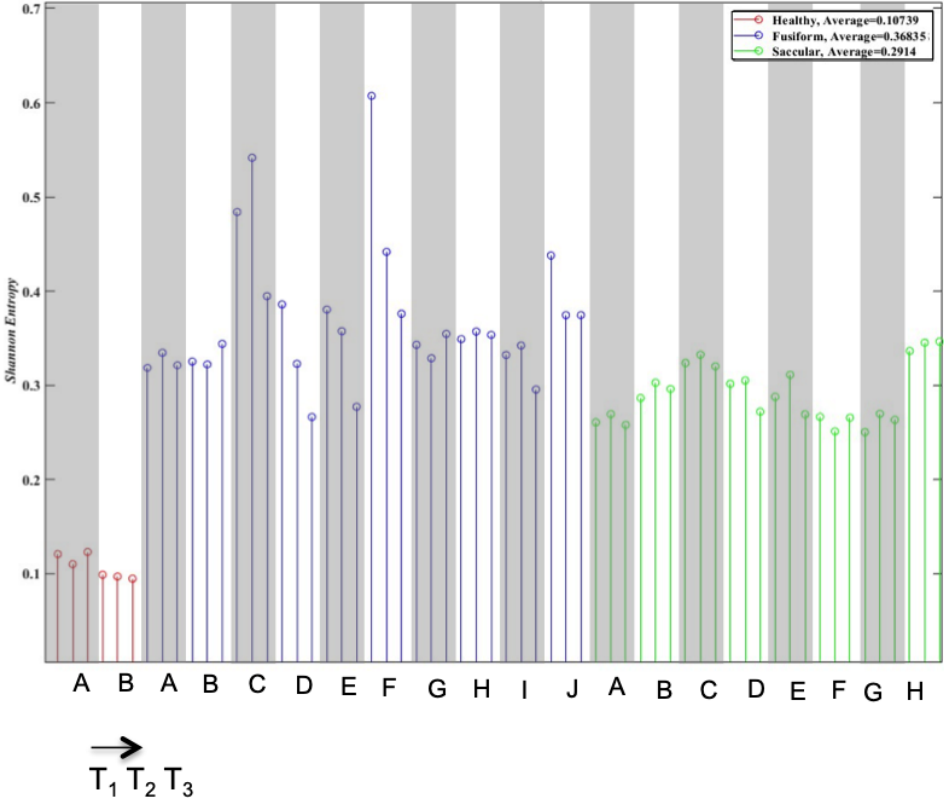


Figure 42: Shannon entropy y-axis, x-axis represents all cases studied clustered by plane in groups of heart rate levels.

5 Discussion and conclusion

5.1 Patient-specific models

This work assessed flow in aneurysm models based on patients' real anatomic structures. The first objective was to build these models. We show that the fabrication method used, which had, prior to this work, only been used to create ventricles and aortic models with simplified geometries, is suitable for more complex models. We were able to create 3 structures with different specific anatomies that were subsequently analyzed and compared regarding their impacts on blood flow. This method is more likely to show flow variations that mimic physio-pathological anomalies and are closer to reality. Moreover, as explained, this method preserves the mold when removing the model, limiting the usage of material and the waste created. Once the mold is done for a specific patient, multiple phantoms can be created.

5.2 Hemodynamic study of AAA in patient-specific models

Regarding the hemodynamic study of AAA and its use to monitor aneurysm growth and rupture risk, our results seem to show that the development of large vortical structures near the neck of the aneurysm and the formation of recirculation regions can result in adverse hemodynamic effects. Indeed, in both AAA models, rotational motions were observed in the aneurysm bulge. These changes in the flow may exacerbate the dilatation and increase the rupture risk. The structures that may impact health are the jets and vortices that create high shear stress that can destroy or damage endothelial cells. The creation of stagnation areas and the overall reduction of velocity in the aneurysm increase the stagnation time of blood flow. It may also cause vascular injury. Indeed, stagnation is known to favor thrombus formation.

Therefore, modification of blood flow in AAA will have an impact on thrombus formation and direct endothelial cell injury. Different studies focused on hemodynamic mechanical stress and endothelial cell damage. It was shown that hemodynamic forces cause alterations in endothelial cell function. Indeed, mechanical stress may modify gene expression. Although the signaling network between shear stress and gene expression has not yet been fully described, the role of the cytoskeleton and other mediators were suggested, as mentioned in [\(Patrick et al. 1995\)](#). This study analyzed the phenotype of endothelial cells modified by hemodynamics. If we compare the two aneurysm models used in this study to each other and to a study based on simplified aneurysms [\(Norouzi 2020\)](#), we can confidently say that the flow in patient-specific models presents additional features compared to the averaged model cases. However, this would not be true for every patient-specific model, as some will be close to the average model. Our saccular aneurysm had a fairly common size with a maximum diameter close to 37 mm. This model differs from the averaged model and it is primarily because of a slightly reduced diameter at the aneurysm neck (17 mm maximum diameter). The most significant difference, however, is that this saccular aneurysm is extremely asymmetric; as the aneurysm is saccular, the bulge is only present on the anterior face. If we compare this AAA to the averaged fusiform model of dimension 40 mm in the work by [\(Norouzi 2020\)](#), differences are observed. In our asymmetrical model, a large recirculation area is seen with relatively fast velocities, and we described the formation of a vortex ring. (This is to be compared with a flow closer to the healthy case in the averaged model of 40 mm maximum diameter obtained by [\(Norouzi 2020\)](#)).

Moreover, this type of aneurysm seems to have more interactions with the walls compared to the averaged model. This can be explained, firstly, by the curvature of the patient-specific model, in contrast to the relatively straight averaged model. Here, the inlet and outlet of the patient-specific model are not aligned. The complexity of the flow is therefore increased due

to the impact of the entering jet into the wall of the aneurysm. It appears that the saccular aneurysm, because of its asymmetric geometry, contributes to the development of more vortex structures. Finally, the patient-specific aneurysm also has tortuous iliac arteries that are thinner and longer compared to those of the simplified model. We suspect that in this case, it is responsible for a part of the resistance in the downstream system, although no effect of the iliac arteries' geometry was clearly identified here.

Regarding the patient-specific fusiform aneurysm, its dimensions are far from the average, as this aneurysm has a maximum diameter close to 70 mm. This diameter is near a critical stage with a rupture risk estimated at 30% to 40% per year. Compared to an averaged model, a model of a fusiform AAA with a maximum diameter of 50 mm was studied by [\(Norouzi 2020\)](#). The patient-specific model does not develop the same propagating vortex ring as the averaged model. Instead, the vortices created at the neck of the aneurysm are unstable, decaying rapidly, and forming smaller vortices. This could be caused by the angulation at the neck of the aneurysm, which is absent from the averaged model. Studies of proximal neck angulation have shown its impact on turbulence, asymmetric flow, and recirculation in the AAA bulge; an example of such a study is [\(Kaewchoothong et al. 2022\)](#). It is also possible that the significant difference between the iliac arteries and the AAA bulge creates an important pressure reflection wave. We cannot exclude the possibility that it could create an adverse pressure gradient, limiting the propagation of the vortex ring.

Concerning the viscous energy dissipation rate, it can be observed that in the plane capturing the flow patterns responsible for the energy dissipation per unit depth, the maximum obtained in the saccular model (under our resting conditions $r_l = 60$ bpm) is 0.03 W/m, which is close to the results obtained in the averaged fusiform model with a diameter of 40 mm. However, in the case of the fusiform aneurysm model, the energy dissipation is lower. Although the

experience with the averaged model indicated that an increase in diameter should lead to an increase in $VEDr$, it should be noted that the relationship between the size of the aneurysm and energy dissipation should take into account another geometric parameter. As mentioned, it is also possible that the localized nature of the structure responsible for energy dissipation needs to be considered when integrated on the surface of the aneurysm.

Regarding the use of Proper Orthogonal Decomposition (POD) in these models, it is evident that the extraction of energetically significant modes improved our understanding of flow behavior. For instance, we identified that a substantial portion of the energy in the vortical structures of the saccular model was expressed in the interaction between this structure and the wall near the exit of the aneurysm. The time coefficient of POD modes can also provide additional insights. As observed in the first mode of plane A in the fusiform model, the time coefficient exhibits an oscillatory behavior, closely resembling the inlet flow waveform for both the healthy and saccular models. To explain this phenomenon, the relationship between aneurysm size and iliac resistance could be explored.

Furthermore, we demonstrated the feasibility of creating reduced models of this flow using a truncated number of modes. The POD study enabled the identification of a significant difference in Shannon entropy values between the healthy case and the pathological cases, as well as notable differences between the two AAA models. This suggests that the Shannon entropy, utilized as a marker of flow complexity, could serve as a robust parameter for analyzing various aneurysm cases.

This study aimed to capture the flow movement through the aneurysm bulge by scanning multiple planes on each model. This approach enables the capture of the 3D motion of the flow, but it lacks depth resolution, making it challenging to confidently measure values for the total volume of the AAA or the entire wall surface. Gaining access to a 3D visualization of

the flow would be a significant advancement in the study of AAA hemodynamics. The use of stereo Particle Image Velocimetry (PIV) could help provide some insight into the third velocity component. However, conducting a multi-plane stereo PIV experiment is relatively complex, and errors could arise if the third velocity component is of significant importance. Tomographic PIV seems to be a suitable solution for capturing 3D flow in AAA phantoms. Nonetheless, from our experience, a major issue encountered when working with PIV is the illumination of the entire AAA volume and all the aneurysm walls, causing reflections that obscure the particles from the camera's view. Thus, optimizing the Refractive Index (RI) match between the working blood-analog and the silicone of the model walls is crucial for tomographic PIV. Additionally, using particles emitting more light toward the camera, such as fluorescent particles, could prove essential.

Comparing these *in vitro* results with numerical simulations could also be of interest, as a validated *in silico* model would provide insight into the total 3D flow. In this context, monitoring the pressure in the iliac arteries during the experiment to create tailored outlet boundary conditions would be of interest. It is important to note that the inlet boundary condition used in our *in vitro* study is the flow measurement.

Studying another dynamic parameter could yield valuable insights. Specifically, investigating wall shear stress and oscillatory shear index would be meaningful, as they are suspected to impact aneurysm growth. Another parameter worth studying is turbulence kinetic energy, given our demonstration that the aneurysm generates turbulence, and that flow complexity varies among different models. To study turbulence kinetic energy, an ensemble average of velocity over more than 10 heartbeats would be necessary.

In conclusion, our results collectively demonstrate that using phantoms is technically feasible for studying the impact of specific aneurysm geometry on blood flow. The obtained results

revealed discrepancies with averaged models. We can speculate that averaged models do not universally apply to all patients. While they are valuable for understanding basic flow modifications, patient-specific in vitro-based models are better suited to comprehend the flow variability across the diverse aneurysm geometries found in patients. If specific markers can be identified and linked to rupture risk through a systematic flow study of patients, it could be interesting to explore correlations between flow modifications and disease history in patients with long-term follow-up.

Bibliography

ADRIAN, Ronald J., WESTERWEEL, Jerry. *Particle Image Velocimetry*. Cambridge university press, 2011.

ALEXANDER, J. Jeffrey. The pathobiology of aortic aneurysms. *Journal of surgical research*, 2004, vol. 117, no 1, p. 163-175.

ARZANI, Amirhossein, SHADDEN, Shawn C. Transport and mixing in patient-specific abdominal aortic aneurysms with lagrangian coherent structures. In: *Summer Bioengineering Conference*. American Society of Mechanical Engineers, 2012. p. 9-10.

ASBURY, Charles L., RUBERTI, Jeffrey W., BLUTH, Edward I., *et al.* Experimental investigation of steady flow in rigid models of abdominal aortic aneurysms. *Annals of biomedical engineering*, 1995, vol. 23, p. 29-39.

BARKER, Alex J., PIM VAN, Ooij, KRISHNA, Bandi, *et al.* Viscous energy loss in the presence of abnormal aortic flow, *Magnetic Resonance in Medicine*, 2014, vol. 72, no. 3, p. 620-628.

BENARD, Nicolas, JARNY, Sebastien, COISNE, Damien. Definition of an experimental blood like fluid for laser measurements in cardiovascular studies. *Applied Rheology*, 2007, vol. 17, no 4, p. 44251-1-44251-8.

BETTS, Gordon J., DESAIX, Peter, JOHNSON, Eddie, *et al.* Anatomy and Physiology. Openstax College, 2013, vol 2, ch. 26, p. 1187-12009

BLUESTEIN, Danny, NIU, Lijun, SCHOEPHOERSTER, Richard T., *et al.* Steady flow in an aneurysm model: correlation between fluid dynamics and blood platelet deposition, 1996, vol. 118, no 3, p.280-287

BLUTH, Edward I., MURPHEY, Steven M., HOLLIER, Larry H., *et al.* Color flow Doppler in the evaluation of aortic aneurysms. *International Angiology: A journal of the International Union of Angiology*, 1990, vol. 9, no 1, p. 8-10.

BOPP, Maximilian, BAUER, Andreas., WEGT, Sebastian, *et al.* A computational and experimental study of physiological pulsatile flow in an aortic aneurysm. In: *Proceedings of the 11th International Symposium on Turbulence and Shear Flow Phenomena, Southampton, UK (United Kingdom)*. 2019.

BREWSTER, David C., CRONENWETT, Jack L., HALLETT JR, John W., *et al.* Guidelines for the treatment of abdominal aortic aneurysms: report of a subcommittee of the Joint Council of the American Association for Vascular Surgery and Society for Vascular Surgery. *Journal of Vascular Surgery*, 2003, vol. 37, no 5, p. 1106-1117.

BRIET, Marie, BOUTOUYRIE, Pierre, LAURENT, Stéphane, *et al.* Arterial stiffness and pulse pressure in CKD and ESRD. *Kidney International*, 2012, vol. 82, no 4, p. 388-400.

BRINDISE, Melissa C., BUSSE, Margaret M., VLACHOS, Pavlos P. Density- and viscosity-matched Newtonian and non-Newtonian blood-analog solutions with PDMS refractive index. *Experiments in Fluids*, 2018, vol. 59, p. 1-8.

BROWNRIGG, Jack R. W., DE BRUIN, Jorg L., ROSSI, Luca, *et al.* Endovascular aneurysm sealing for infrarenal abdominal aortic aneurysms: 30-day outcomes of 105 patients in a single centre. *European Journal of Vascular and Endovascular Surgery*, 2015, vol. 50, no 2, p. 157-164.

CANADIAN NUCLEAR SAFETY COMMISSION, 30 March 2023, available from: <http://nuclearsafety.gc.ca/eng/resources/radiation/introduction-to-radiation/radiation-doses.cfm>

CAZEMIER, Willem. *Proper Orthogonal Decomposition and Low Dimensional Models for Turbulent Flows*. Rijksuniversiteit Groningen, 1997, ch. 2.

CHEN, Chia-Yuan, ANTÓN, Raúl, HUNG, Ming-yang, *et al.* Effects of intraluminal thrombus on patient-specific abdominal aortic aneurysm hemodynamics via stereoscopic particle image velocity and computational fluid dynamics modeling. *Journal of Biomechanical Engineering*, 2014, vol. 136, no 3, p. 031001.

DARWISH, Ahmed, DI LABBIO, Giuseppe, SALEH, Wael, *et al.* Proper orthogonal decomposition analysis of the flow downstream of a dysfunctional bileaflet mechanical aortic valve. *Cardiovascular Engineering and Technology*, 2021, vol. 12, p. 286-299.

DEPLANO, Valérie, GUIVIER-CURIEN, Carine, BERTRAND, Eric. 3D analysis of vortical structures in an abdominal aortic aneurysm by stereoscopic PIV. *Experiments in Fluids*, 2016, vol. 57, p. 1-11.

DEPLANO, Valérie, KNAPP, Yannick, BAILLY, Lucie, *et al.* Flow of a blood analogue fluid in a compliant abdominal aortic aneurysm model: Experimental modelling. *Journal of Biomechanics*, 2014, vol. 47, no 6, p. 1262-1269.

DEPLANO, Valerie, KNAPP, Yannick, BERTRAND, Eric, *et al.* Flow behaviour in an asymmetric compliant experimental model for abdominal aortic aneurysm. *Journal of Biomechanics*, 2007, vol. 40, no 11, p. 2406-2413.

DI LABBIO, Giuseppe et KADEM, Lyes. Jet collisions and vortex reversal in the human left ventricle. *Journal of Biomechanics*, 2018, vol. 78, p. 155-160.

DI LABBIO, Giuseppe. *On Left Ventricular Fluid Dynamics Associated With Progressive Chronic Aortic Regurgitation*. 2019. Thèse de doctorat. Concordia University.

DUCLAUX, Virginie, GALLAIRE, Francois, CLANET, Christophe. A fluid mechanical view on abdominal aortic aneurysms. *Journal of Fluid Mechanics*, 2010, vol. 664, p. 5-32.

DYVERFELDT, Petter, HOPE, Michael D., TSENG, Elaine, SALONER, David. Magnetic resonance measurement of turbulent kinetic energy for the estimation of irreversible pressure loss in aortic stenosis, *JACC: Cardiovascular Imaging*, 2013, vol. 6, no. 1, p.64-71.

ENGELHARD, Stefan, VOORNEVELD, Jason, VOS, Hendrik J., *et al.* High-frame-rate contrast-enhanced ultrasound particle image velocimetry in the abdominal aorta: First human results. *Radiology*. 2018. vol. 289, no.1, p. 119-125.

ETEBARI, Ali and VLACHOS, Pavlos P. Improvements on the accuracy of derivative estimation from DPIV velocity measurements. *Experiments in Fluids*, 2005, vol. 39, p. 1040-1050.

FRASER, Katharine H., MEAGHER, Siobhan, BLAKE, James R., *et al.* Characterization of an abdominal aortic velocity waveform in patients with abdominal aortic aneurysm. *Ultrasound in Medicine & Biology*, 2008, vol. 34, no 1, p. 73-80.

GOPALAKRISHNAN, Shyam Sunder. *Dynamics and Stability of flow through Abdominal Aortic Aneurysms*. 2014. Thèse de doctorat. Université Claude Bernard-Lyon I.

HAGER, Alfred, KAEMMERER, Harald, RAPP-BERNHARDT, Ulrike, *et al.* Diameters of the thoracic aorta throughout life as measured with helical computed tomography. *The Journal of Thoracic and Cardiovascular Surgery*, 2002, vol. 123, no 6, p. 1060-1066.

HARVEY, William, *et al.* Exercitatio anatomica de motu cordis et sanguinis in animalibus. *Frankfurt am Main*, 1928, vol. 1628, p. 17.

HEALTH CANADA, Ultrasound, 10 October 2019 available from:
<https://www.canada.ca/en/health-canada/services/health-risks-safety/radiation/medical/ultrasound.html>

HOLZAPFEL, Gerhard A., GASSER, Thomas C., OGDEN, Ray W.. A new constitutive framework for arterial wall mechanics and a comparative study of material models. *Journal of Elasticity and the Physical Science of Solids*, 2000, vol. 61, p. 1-48.

IAIZZO, Paul A. (ed.). *Handbook of Cardiac Anatomy, Physiology, and Devices*. Springer Science & Business Media, 2010.

INDRAKUSUMA, Reza, JALALZADEH, Hamid, VAN DER LAAN, Maarten, *et al.* 4D Flow MRI in Patients with Asymptomatic Abdominal Aortic Aneurysms: Reproducibility and Clinical Analysis. *European Journal of Vascular and Endovascular Surgery*, 2019, vol. 58, no 6, p. e652-e654.

ISSELBACHER, Eric M. Thoracic and abdominal aortic aneurysms. *Circulation*, 2005, vol. 111, no 6, p. 816-828.

KAEWCHOOHONG, Natthaporn, ALGABRI, Yousif A., ASSAWALERTSAKUL, Thanin, *et al.* Computational study of abdominal aortic aneurysms with severely angulated neck based on transient hemodynamics using an idealized model. *Applied Sciences*, 2022, vol. 12, no 4, p. 2113.

KASSEM, Tamer W. Follow up CT angiography post EVAR: Endoleaks detection, classification and management planning. *The Egyptian Journal of Radiology and Nuclear Medicine*, 2017, vol. 48, no 3, p. 621-626.

KEMMERLING, Erica MC., PEATTIE, Robert A. Abdominal aortic aneurysm pathomechanics: current understanding and future directions. *Molecular, Cellular, and Tissue Engineering of the Vascular System*, 2018, p. 157-179.

KENT, K. Craig, ZWOLAK, Robert M., EGOROVA, Natalia N., *et al.* Analysis of risk factors for abdominal aortic aneurysm in a cohort of more than 3 million individuals. *Journal of Vascular Surgery*, 2010, vol. 52, no 3, p. 539-548.

KHANAFER, Khalil M., BULL, Joseph L., BERGUER, Ramon. Fluid–structure interaction of turbulent pulsatile flow within a flexible wall axisymmetric aortic aneurysm model. *European Journal of Mechanics-B/Fluids*, 2009, vol. 28, no 1, p. 88-102.

KHE, Alexander K., CHUPAKHIN, Alexander P., CHEREVKO, Alexander A., *et al.* Viscous dissipation energy as a risk factor in multiple cerebral aneurysms. *Russian Journal of Numerical Analysis and Mathematical Modelling*, 2015, vol. 30, no 5, p. 277-287.

KU, David N. Blood flow in arteries. *Annual Review of Fluid Mechanics*, 1997, vol. 29, no 1, p. 399-434.

KUNG, Ethan O., LES, Andrea S., MEDINA, Francisco, *et al.* *In vitro* validation of finite-element model of AAA hemodynamics incorporating realistic outlet boundary conditions. *Journal of Biomechanical Engineering*, 2011, vol. 133, no 4.

LAENNEC, René Théophile Hyacinthe et LAENNEC, Mériadec. *Traité de l'auscultation médiate, et des maladies des poumons et du coeur*. JS Chaudé, 1837.

LES, Andrea S., SHADDEN, Shawn C., FIGUEROA, C. Alberto, *et al.* Quantification of hemodynamics in abdominal aortic aneurysms during rest and exercise using magnetic resonance imaging and computational fluid dynamics. *Annals of Biomedical Engineering*, 2010 a, vol. 38, p. 1288-1313.

LES, Andrea S., YEUNG, Janice J., SCHULTZ, Geoffrey M., *et al.* Supraceliac and infrarenal aortic flow in patients with abdominal aortic aneurysms: mean flows, waveforms, and allometric scaling relationships. *Cardiovascular Engineering and Technology*, 2010 b, vol. 1, p. 39-51.

LYNCH, Richard M. Accuracy of abdominal examination in the diagnosis of non-ruptured abdominal aortic aneurysm. *Accident and Emergency Nursing*, 2004, vol. 12, no 2, p. 99-107.

MARKL, Michael, FRYDRYCHOWICZ, Alex, KOZERKE, Sebastian, *et al.* 4D flow MRI. *Journal of Magnetic Resonance Imaging*, 2012, vol. 36, no 5, p. 1015-1036.

MARRERO, Victor L., TICHY, John A., SAHNI, Onkar, *et al.* Numerical study of purely viscous non-Newtonian flow in an abdominal aortic aneurysm. *Journal of Biomechanical Engineering*, 2014, vol. 136, no 10, p. 101001.

MAY, James, WHITE, Geoffrey H., WAUGH, Richard, *et al.* Comparison of first-and second-generation prostheses for endoluminal repair of abdominal aortic aneurysms: a 6-year study with life table analysis. *Journal of Vascular Surgery*, 2000, vol. 32, no 1, p. 124-129.

MCGREGOR, Robert, SZCZERBA, Dominik, VON SIEBENTHAL, Martin, *et al.* Exploring the use of proper orthogonal decomposition for enhancing blood flow images via computational fluid dynamics.: *Medical Image Computing and Computer-Assisted Intervention–MICCAI 2008: 11th International Conference, New York, NY, USA, September 6-10, 2008, Proceedings, Part II 11*. Springer Berlin Heidelberg, 2008. p. 782-789.

MOORE JR, James E., KU, David N., ZARINS, Christopher K., *et al.* Pulsatile flow visualization in the abdominal aorta under differing physiologic conditions: implications for increased susceptibility to atherosclerosis. *The American Society of Mechanical Engineering*, 1992, vol. 114, no. 3, p.391-397.

NOROUZI, Shahrzad. *Flow Characteristics in Abdominal Aortic Aneurysms: An In Vitro Study*. 2020. Master Thesis. Concordia University.

O’ROURKE, Malachy J., MCCULLOUGH, James P., KELLY, Sinead. An investigation of the relationship between hemodynamics and thrombus deposition within patient-specific models of abdominal aortic aneurysm. *Proceedings of the Institution of Mechanical Engineers, Part H: Journal of Engineering in Medicine*, 2012, vol. 226, no 7, p. 548-564.

PARASHAR, Abhinav, SINGH, Rahul, PANIGRAHI, Pradipta K., *et al.* Chaotic flow in an aortic aneurysm. *Journal of Applied Physics*, 2013, vol. 113, no 21.

PATEL, Shivam, USMANI, Abdullah Y., MURALIDHAR, Krishnamurthy. Effect of aorto-iliac bifurcation and iliac stenosis on flow dynamics in an abdominal aortic aneurysm. *Fluid Dynamics Research*, 2017, vol. 49, no 3, p. 035513.

PATRICK, JR, Charles, W. MCINTIRE, Larry V. Shear stress and cyclic strain modulation of gene expression in vascular endothelial cells. *Blood Purification*, 1995, vol. 13, no 3-4, p. 112-124.

PEATTIE, Robert A., RIEHLE, Tiffany J., BLUTH, Edward I. Pulsatile flow in fusiform models of abdominal aortic aneurysms: flow fields, velocity patterns and flow-induced wall stresses. *Journal of Biomechanical Engineering*, 2004, vol. 126, no 4, p. 438-446.

PEDRIZZETTI, Gianni et DOMENICHINI, Federico. Nature optimizes the swirling flow in the human left ventricle. *Physical Review Letters*, 2005, vol. 95, no 10, p. 108101.

POELMA, Christian, WATTON, Paul N., VENTIKOS, Yiannis. Transitional flow in aneurysms and the computation of haemodynamic parameters. *Journal of The Royal Society Interface*, 2015, vol. 12, no 105, p. 20141394.

RAFFEL, Markus, WILLERT, Christian E., SCARANO, Fulvio, *et al.* *Particle Image Velocimetry: a Practical Guide*. Springer, 2018.

SAAID, Hicham, VOORNEVELD, Jason, SCHINKEL, Christiaan, *et al.* Tomographic PIV in a model of the left ventricle: 3D flow past biological and mechanical heart valves. *Journal of Biomechanics*, 2019, vol. 90, p. 40-49.

SAKALIHASAN, Natzi, MICHEL, Jean-Baptiste, KATSARGYRIS, Athanasios, *et al.* Abdominal aortic aneurysms. *Nature Reviews Disease Primers*, 2018, vol. 4, no 1, p. 34.

SCARANO, Fulvio RIETHMULLER, Michel L. Advances in iterative multigrid PIV image processing. *Experiments in Fluids*, 2000, vol. 29, no Suppl 1, p. S051-S060.

SCHARNOWSKI, Sven, GRAYSON, Kristian, DE SILVA, Charitha M., *et al.* Generalization of the PIV loss-of-correlation formula introduced by Keane and Adrian. *Experiments in Fluids*, 2017, vol. 58, no 10, p. 150.

SCHERMERHORN, Marc. A 66-year-old man with an abdominal aortic aneurysm: review of screening and treatment. *Journal of the American Medical Association*, 2009, vol. 302, no 18, p. 2015-2022.

SCOTT, Alan P. The Multicentre Aneurysm Screening Study (MASS) into the effect of abdominal aortic aneurysm screening on mortality in men: a randomised controlled trial. *The Lancet*, 2002, vol. 360, no 9345, p. 1531-1539.

SCOTTI, Christine M., SHKOLNIK, Alexander D., MULUK, Satish C., *et al.* Fluid-structure interaction in abdominal aortic aneurysms: effects of asymmetry and wall thickness. *Biomedical Engineering Online*, 2005, vol. 4, p. 1-22.

SHADDEN, Shawn C., TAYLOR, Charles A. Characterization of coherent structures in the cardiovascular system. *Annals of Biomedical Engineering*, 2008, vol. 36, p. 1152-1162.

SIROVICH, Lawrence. Turbulence and the dynamics of coherent structures. I. Coherent structures. *Quarterly of Applied Mathematics*, 1987, vol. 45, no 3, p. 561-571.

TAIRA, Kunihiko, BRUNTON, Steven L., DAWSON, Scott TM, *et al.* Modal analysis of fluid flows: An overview. *American Institute of Aeronautics and Astronautics' Journal*, 2017, vol. 55, no 12, p. 4013-4041.

TAYLOR, Charles A., CHENG, Christopher P., ESPINOSA, Leandro A., *et al.* In vivo quantification of blood flow and wall shear stress in the human abdominal aorta during lower limb exercise. *Annals of Biomedical Engineering*, 2002, vol. 30, p. 402-408.

VERGARA, Christian, LE VAN, Davide, QUADRIO, Maurizio, *et al.* Large eddy simulations of blood dynamics in abdominal aortic aneurysms. *Medical Engineering & Physics*, 2017, vol. 47, p. 38-46.

VITELLO, Dominic J., RIPPER, Richard M., FETTIPLACE, Michael R., *et al.* Blood density is nearly equal to water density: a validation study of the gravimetric method of measuring intraoperative blood loss. *Journal of Veterinary Medicine*, 2015, vol. 2015, p.4

VLACHOPOULOS, Charalambos, O'ROURKE, Michael, NICHOLS, Wilmer W. *McDonald's Blood Flow in Arteries: Theoretical, Experimental and Clinical Principles*. CRC press, 2011.

WESTERWEEL, Jerry, SCARANO, Fulvio. Universal outlier detection for PIV data. *Experiments in Fluids*, 2005, vol. 39, p. 1096-1100.

WILLE, Sven Øivind. Pulsatile pressure and flow in an arterial aneurysm simulated in a mathematical model. *Journal of Biomedical Engineering*, 1981, vol. 3, no 2, p. 153-158.

WITHERS, Kathleen, CAROLAN-REES, Grace, DALE, Megan. Pipeline™ embolization device for the treatment of complex intracranial aneurysms: a NICE Medical Technology Guidance. *Applied Health Economics and Health Policy*, 2013, vol. 11, p. 5-13.

YIP, T. H. et YU, S. C. M. Oscillatory flows in straight tubes with an axisymmetric bulge. *Experimental thermal and fluid science*, 2002, vol. 26, no 8, p. 947-961.

YOUSIF, Majid Y., HOLDSWORTH, David W., POEPPING, Tamie L. A blood-mimicking fluid for particle image velocimetry with silicone vascular models. *Experiments in Fluids*, 2011, vol. 50, p. 769-774.

YU, Ming-Ching. Steady and pulsatile flow studies in abdominal aortic aneurysm models using particle image velocimetry. *International Journal of Heat and Fluid Flow*, 2000, vol. 21, no 1, p. 74-83.

ZHAN, Jie-min, LU, Tian-dong, YANG, Zhi-yun, *et al.* Influence of the flow field and vortex structure of patient-specific abdominal aortic aneurysm with intraluminal thrombus on the arterial wall. *Engineering Applications of Computational Fluid Mechanics*, 2022, vol. 16, no 1, p. 2100-2122.